

DISS. ETH No. 29783

**FUEL FROM SUNLIGHT AND AIR -
DEMONSTRATION, AUTOMATION AND
PARAMETER ANALYSIS**

A thesis submitted to attain the degree of
DOCTOR OF SCIENCES of ETH ZURICH
(Dr. sc. ETH Zurich)

presented by

REMO SCHÄPPI
MSc ETH ME
born on 06.09.1989
citizen of Horgen (ZH)

accepted on the recommendation of

Prof. Dr. Aldo Steinfeld, examiner
Prof. Dr. Justin Lapp, co-examiner

2023

Abstract

Developing novel renewable technologies for producing carbon-neutral transportation fuels has become a global energy challenge. Especially for long-haul aviation synthetic drop-in fuels are a viable option to replace refined fossil fuels. A promising pathway is the production of drop-in fuels made from CO_2 and H_2O using concentrated solar energy as the source of high-temperature process heat. However, so far the technological readiness level has largely been limited to bench-top studies of individual components.

This thesis reports on the technological demonstration under real field conditions of the entire process chain to drop-in fuels from concentrated sunlight and ambient air.

Crucial to this accomplished milestone is the design and integration of three thermochemical conversion units: A direct air capture unit for the co-extraction of CO_2 and H_2O directly from air, a solar redox unit performing the solar redox co-splitting of CO_2 and H_2O to produce a desired syngas mixture, and the gas-to-liquid synthesis unit converting the syngas to liquid methanol or hydrocarbon fuels. This thesis presents the components of the implemented process chain, with a focus on the solar redox unit as the core process. It presents the fully automated full day cyclic production of syngas suitable for either methanol or Fischer-Tropsch synthesis, demonstrating the stability and robustness of the system. The demonstration of the

implemented process chain is concluded with a multiple day production campaign for producing syngas that is later on transformed to methanol.

A parametric study of the main operational parameters (namely: reactor pressure, reduction-end and oxidation-start temperatures, CO_2 and H_2O mass flow rates) determines the influence on the key performance indicators such as the specific fuel yield, molar conversion, and solar-to-fuel energy efficiency. This thesis shows how the syngas product quality can be tailored for Fischer-Tropsch synthesis by selecting adequate oxidation conditions, eliminating the need for additional downstream refining of the syngas. Changing process parameters such as reduction/oxidation temperatures, gas flow rates, or oxidation start/end conditions allows optimising the cycles towards maximising either efficiency, quality, yield or conversion.

The entire solar fuel system is fully-automated based on real-time product gas analysis and feedback control loops, and can be further extended with an auto-optimisation scheme that executes online mass and energy balances to guide performance improvement. An example of a solar run of fully-automated consecutive redox cycles is presented to show the implementation of this control scheme for the optimisation of the solar fuel system.

A dynamic grey box model of the redox reactor is developed for the purpose of further examining the dependence of reactor outputs to reactor inputs and investigating different operation procedures to run the reactors. The developed reactor model can also be used as building block for a future model of the entire solar fuel system. A simplified model to simulate a two reactor system and a three reactor system that make continuous use of the solar power incident on the system is applied. It allows the comparison of the two systems and helps to determine the feasibility of incorporating a third reactor of similar design into the system. The analysis shows that, for a solar power of 4.8 kW, the three reactor system is not a viable option, as additionally to the more complex implementation, it also shows 36.6% lower hourly production rate and solar-to-syngas energy efficiency. However, since, for a solar power of 6.2 kW, the two reactor system is forced to experience times where both reactors are off-sun in order to keep producing syngas,

introducing a third reactor when operating at higher power levels might be a viable option to keep making uninterrupted use of the incoming solar radiation.

Zusammenfassung

Die Entwicklung erneuerbarer Technologien zur Herstellung von CO₂-neutralen Treibstoffen für den Transportsektor ist zu einer globalen energiewirtschaftlichen Herausforderung geworden. Insbesondere für Langstreckenflüge sind synthetische Treibstoffe eine realisierbare Option, um raffinierte fossile Treibstoffe zu ersetzen. Ein vielversprechender Weg ist die Produktion von flüssigen Treibstoffen aus CO₂ und H₂O unter Verwendung konzentrierter Sonnenenergie als Quelle für die Hochtemperatur-Prozesswärme. Bisher beschränkte sich der technologische Reifegrad jedoch weitgehend auf Laborstudien einzelner Komponenten.

Die vorliegende Arbeit berichtet über die Demonstration der gesamten Prozesskette von konzentriertem Sonnenlicht und Umgebungsluft zu flüssigen Treibstoffen, unter realen äusseren Bedingungen.

Wichtig für das Erreichen dieses Meilensteins ist die Entwicklung und die Integration von drei thermochemischen Umwandlungseinheiten: Eine Einheit zur direkten Abscheidung von CO₂ und H₂O aus der Luft, eine solare Redox-Einheit für die solare Redox-Spaltung von CO₂ und H₂O in ein gewünschtes Synthesegasgemisch und die Syntheseinheit, die das Synthesegas in flüssiges Methanol oder Kohlenwasserstoffe umwandelt. Die vorliegende Arbeit stellt die Komponenten der implementierten Prozesskette vor, mit einem Fokus auf der solaren Redox-Einheit als Kernprozess. Sie zeigt die ganztägige

vollautomatische zyklische Produktion von Synthesegas, das entweder für die Methanol- oder Fischer-Tropsch-Synthese geeignet ist, und demonstriert die Stabilität und Robustheit des Systems. Die Demonstration der implementierten Prozesskette wird mit einer mehrtägigen Produktionskampagne zur Herstellung von Synthesegas abgeschlossen, welches später in Methanol umgewandelt wird.

Eine parametrische Untersuchung der wichtigsten Betriebsparameter (Reaktordruck, Temperaturen am Ende der Reduktion und Oxidation, Massenströme von CO_2 und H_2O) bestimmt den Einfluss auf die wichtigsten Leistungsindikatoren wie die spezifische Treibstoffproduktion, die molare Umwandlung und die Energieeffizienz von der Sonnenenergie zum Treibstoff. Diese Arbeit zeigt, wie die Qualität des Synthesegas für die Fischer-Tropsch-Synthese durch die Auswahl geeigneter Oxidationsbedingungen angepasst werden kann, wodurch die Notwendigkeit einer nachgelagerten Raffinierung des Synthesegases entfällt. Durch die Änderung von Prozessparametern wie Reduktions- und Oxidationstemperaturen, Gasmassenströmen oder Oxidationsstart- und Endbedingungen können die Zyklen optimiert werden, um Effizienz, Qualität, Ausbeute oder Umwandlung zu maximieren.

Das gesamte Solartreibstoffsystem ist auf der Grundlage von Echtzeit Produktgasanalysen und Feedback-Regelkreisen vollständig automatisiert und kann mit einem automatischen Optimierungsschema erweitert werden, welches laufend Massen- und Energiebilanzen berechnet, um die Leistungsverbesserung zu steuern. Ein Beispiel eines Messtages mit vollautomatischen aufeinanderfolgenden Redoxzyklen wird gezeigt, um die Implementierung dieses Steuerungsschemas zur Optimierung des solaren Treibstoffes zu demonstrieren.

Ein dynamisches Gray-Box-Modell des Redox-Reaktors wird vorgestellt, um die Abhängigkeit der Reaktoroutputs von den Reaktorinputs weiter zu untersuchen und verschiedene Verfahren für den Betrieb der beiden Reaktoren zu testen. Das entwickelte Reaktormodell kann auch als Baustein für ein zukünftiges Modell des gesamten Solartreibstoffsystems verwendet werden. Die Anwendung eines vereinfachten Modells zur Simulation eines Zwei-

Reaktor-Systems und eines Drei-Reaktor-Systems, die die Sonnenenergie kontinuierlich nutzen, ermöglicht den Vergleich der beiden Systeme, um zu bestimmen, wie sinnvoll eine zukünftige Integration eines dritten Reaktors mit demselben Design wäre. Die Analyse zeigt, dass das Drei-Reaktor-System für eine Leistung von 4.8 kW keine sinnvolle Option ist, da es neben der komplexeren Implementierung auch eine um 36.6% geringere stündliche Produktionsrate und Energieumwandlungseffizienz aufweist. Da das System mit zwei Reaktoren jedoch bei einer Leistung von 6.2 kW gezwungen ist, Zeiten zu durchlaufen, in denen beide Reaktoren nicht der Sonne ausgesetzt sind, um weiterhin Synthesegas zu produzieren, könnte die Einführung eines dritten Reaktors beim Betrieb mit höherer Leistung eine sinnvolle Option sein für die ununterbrochene Nutzung der einfallenden Sonnenstrahlung.

Acknowledgements

I would like to thank Prof. Aldo Steinfeld for this wonderful opportunity to conduct my doctoral thesis under his supervision at the Professorship of Renewable Energy Carriers (PREC). His guidance and continued support was invaluable throughout my time in his group and very much appreciated.

I am thankful to Prof. Justin Lapp from the University of Maine for acting as co-examiner.

I also thank Brendan Bulfin for acting as second supervisor in the last year and all the fruitful discussions and inputs especially on the topic of modelling chemical reactions.

I want to thank Philipp Furler for being my direct supervisor and team leader in the beginning of my doctoral studies and Alexander Muroyama for the fruitful discussions and contributions to the project as a member of the team working on the initial setup construction. I also want to thank Fabian Dähler for first introducing me to this wonderful project, and giving me the opportunity to start working on the solar optics of the solar dish system.

I thank Philipp Haueter for the countless constructive discussions and solutions to design challenges and his contribution in designing and building the dish-setup on the roof. I also thank Julian Urech for the technical sup-

port, all the manufactured parts as well as for sitting in on experimental runs.

I thank Leonore Noll for the administrative support.

I would like to thank all the students I had the pleasure to work with and who's semester projects (SP) or master thesis (MT) I could supervise. Their help was invaluable, especially during the intensive days working on the setup and conducting experiments. This thank goes to Yago Vila (SP), David Rutz (MT), Patrick Basler (MT), Matthieu Dessieux (SP), Maurice Grunder (MT), Boris Kunz (MT) and Vivien Hüsler (MT). Especially I would like to thank the students supporting this project also as assistants, David Rutz, Patrick Basler, Vivien Hüsler and Daniel Notter.

I want to thank all the past and current members of the PREC group I had the pleasure of working with for all the support and the fruitful discussions during meetings, lunch and coffee breaks, and for all the friendship and fun times also not work related.

And finally I would like to thank my family: Rachel, Lyle and Elva for their love, support, patience and always being there...

I am grateful for the funding by the Swiss Federal Office of Energy to make this project possible. This work was funded in part by the Swiss Federal Office of Energy (Grant No. SI/501213-01 and Grant No. SI/502552-01), the Swiss National Science Foundation (Grant No. 200021-162435), and the European Research Council under the European Union's ERC Advanced Grant (SUNFUELS - Grant No. 320541).

Contents

| | |
|---|------------|
| Abstract | iii |
| Zusammenfassung | vii |
| Acknowledgements | x |
| Contents | xi |
| Nomenclature | xv |
| 1 Introduction | 1 |
| 1.1 Sustainable Fuel Production | 1 |
| 1.2 The Ceria Cycle | 3 |
| 1.3 Previous Reactor Designs | 5 |
| 1.4 Thesis Goal and Outline | 6 |
| 2 Demonstration of the Entire Process Chain from Sunlight and Air to Solar Fuels | 9 |
| 2.1 System Design and Experimental Setup | 10 |
| 2.1.1 DAC Unit | 10 |
| 2.1.2 Solar Redox Unit | 12 |
| 2.1.3 GTL Unit | 22 |
| 2.2 Cycles for CO ₂ -splitting | 25 |

| | | |
|----------|--|-----------|
| 2.2.1 | Representative CO ₂ -splitting Cycle | 25 |
| 2.2.2 | Full-day Stable CO ₂ -splitting Cycles | 26 |
| 2.3 | Cycles Targeting Syngas for Methanol and FT Synthesis . . . | 29 |
| 2.3.1 | Representative Co-splitting Cycle | 30 |
| 2.3.2 | Cycle Targeting Syngas for Methanol Synthesis | 31 |
| 2.3.3 | Cycle Targeting Syngas for Fischer-Tropsch Synthesis | 34 |
| 2.4 | Producing Syngas for Methanol Synthesis | 37 |
| 2.4.1 | Full-day Syngas Production for Methanol Synthesis | 37 |
| 2.4.2 | Long-term Production Campaign for Methanol Synthesis | 39 |
| 2.5 | Energy Efficiency Analysis | 41 |
| 2.6 | Summary and Conclusions | 46 |
| 3 | Parametric Study of the Solar Reactor Operation | 49 |
| 3.1 | Reduction Parameters | 51 |
| 3.2 | Oxidation Parameters Co-splitting | 53 |
| 3.3 | Separate Splitting of CO ₂ and H ₂ O | 57 |
| 3.3.1 | Oxidation of CO ₂ -splitting | 58 |
| 3.3.2 | Oxidation of H ₂ O Dominant Co-splitting | 58 |
| 3.4 | Summary and Conclusions | 61 |
| 4 | Control and Automation of the Solar Fuel System | 63 |
| 4.1 | Automation Control Logic | 64 |
| 4.2 | LabView Implementation | 67 |
| 4.3 | Auto-optimisation of Full Day Run | 69 |
| 4.3.1 | Auto-optimisation Description | 69 |
| 4.3.2 | Experimental Results and Discussion | 71 |
| 4.4 | Summary and Conclusions | 73 |
| 5 | Dynamic Gray Box Model | 75 |
| 5.1 | Model Description | 77 |
| 5.1.1 | Model Equations | 78 |
| 5.2 | Simplified Model | 84 |
| 5.3 | Model Application — Multi Reactor System | 93 |

| | | |
|----------|--|------------|
| 5.4 | Summary and Conclusions | 100 |
| 6 | Summary and Outlook | 101 |
| 6.1 | Summary | 101 |
| 6.2 | Outlook and Research Recommendations | 103 |
| 6.2.1 | Improvements on the Setup and Reactor Design | 103 |
| 6.2.2 | Operation of the Fuel System | 108 |
| 6.2.3 | System Integration | 110 |
| 6.2.4 | Advances in System and Reactor Modelling | 112 |
| 6.2.5 | Scale-up to Industrial Size Plant | 113 |
| 6.2.6 | Techno Economic Analysis | 114 |
| 6.2.7 | Bringing Solar Fuels to the Market | 116 |
| | List of figures | 119 |
| | List of tables | 127 |
| | Bibliography | 129 |
| | Curriculum vitae | 143 |
| | List of publications | 145 |

Nomenclature

Abbreviations

| | |
|--------|---|
| CFD | Computational fluid dynamics |
| CORSIA | Carbon Offsetting and Reduction Scheme for International Aviation |
| CPI | Combined performance indicator |
| CSP | Concentrated solar power |
| DAC | Direct air capture |
| DNI | Direct normal irradiation |
| FT | Fischer-Tropsch |
| GTL | Gas to liquid |
| GUI | Graphical user interface |
| NRMSE | Normalized root mean square error |
| O&M | Operation and maintenance |
| PI | Performance indicator |
| PPA | Power purchase agreement |
| ppi | Pores per inch |
| PU | Polyurethane |
| PV | Photo voltaic |
| R&D | Research and Development |
| RPC | Reticulated porous ceramic |
| RWGS | Reverse water gas shift |
| SAF | Sustainable aviation fuel |

SCADA Supervisory control and data acquisition

SEM Scanning electron microscope

Greek Symbols

| | | |
|----------------|-----------------------------------|--|
| α | Absorptivity | - |
| ΔE | Apparent activation energy | $J \cdot mol^{-1}$ |
| ΔH | Molar enthalpy change | $kJ \cdot mol^{-1}$ |
| Δt | Time duration | s |
| δ | Non-stoichiometry of ceria | - |
| $\Delta\delta$ | Oxygen exchange capacity of ceria | - |
| ϵ | Emissivity | - |
| η | Energy efficiency | - |
| σ | Stefan-Boltzmann constant | $5.67 \cdot 10^{-8} W \cdot m^{-2} \cdot K^{-4}$ |

Latin Symbols

| | | |
|--------------|--------------------------------------|---|
| \dot{m} | Mass flow rate | $L \cdot min^{-1} \quad g \cdot min^{-1}$ |
| \dot{n} | Molar flow rate | $mol \cdot s^{-1}$ |
| \dot{V} | Yield per time | $L \cdot h^{-1}$ |
| \dot{X} | Instantaneous molar conversion | - |
| A | Area | m^2 |
| c | Specific heat capacity | $J \cdot kg^{-1} \cdot K^{-1}$ |
| CPI | Combined performance indicator | - |
| h | Specific enthalpy | $J \cdot mol^{-1}$ |
| K_0 | Rate constant | s^{-1} |
| m | Mass | kg |
| n | Fitting parameter | - |
| p | Pressure | $mbar$ |
| P_{solar} | Solar power incident on the reactors | kW |
| PI | Performance indicator | - |
| R | Ideal Gas Constant | $8.314 J \cdot mol^{-1} \cdot K^{-1}$ |
| $R_{H_2:CO}$ | $H_2 : CO$ molar ratio in syngas | - |
| s | Specific entropy | $J \cdot mol^{-1}$ |
| T | Temperature | K |
| t | Time | s |

| | | |
|--------------------|---|--------------------|
| UA | UA product | $W \cdot K^{-1}$ |
| V | Cumulative volume / yield | L |
| V | Volume | m^3 |
| w | Weight factor | - |
| X | Cumulative molar conversion | - |
| Q_{fuel} | Heating value of the fuel over a cycle | W |
| Q_{inert} | Thermal energy penalty of inert gas consumption | W |
| Q_{pump} | Thermal energy penalty of vacuum pumping | W |
| Q_{solar} | Solar energy input of the reduction step | W |
| r_{fuel} | Molar rate of the fuel produced | $mol \cdot s^{-1}$ |

Subscripts

| | |
|-----------------|-----------------|
| app | Apparent |
| cond | Conductive |
| conv | Convective |
| cool-down | Cool-down |
| cycle | Cycle |
| dish | Dish |
| fuel | Fuel |
| g | Gaseous |
| geo | geometrical |
| mean | Mean value |
| oxidation | Oxidation |
| oxidation-end | Oxidation end |
| oxidation-start | Oxidation start |
| p | Porous |
| rad | Radiative |
| reactor | Reactor |
| reduction | Reduction |
| reduction-end | Reduction end |
| reduction-start | Reduction start |
| ref | Reference |
| s | Solid |

solar-to-syngas Solar-to-syngas
syngas Syngas

INTRODUCTION

1.1 Sustainable Fuel Production

In the current debate on measures to mitigate greenhouse gas emissions, reducing emissions from the transport sector becomes increasingly important. Aviation and shipping alone currently contribute approximately 8% of total anthropogenic CO₂ emissions, with growth in tourism and global trade projected to increase this contribution further [1, 2]. Carbon-neutral transportation is feasible with electric motors powered by rechargeable batteries in cars, but becomes very challenging if not impossible for long-haul commercial travel and particularly air travel [3]. For long-haul aviation sustainable aviation fuels (SAF) are being considered [4]. Importantly, SAF are drop-in fuels (synthetic alternatives for petroleum-derived liquid hydrocarbon fuels such as kerosene, gasoline or diesel) and can utilize existing storage, distribution, and utilization infrastructure and thus require no new technologies beyond the production chain. SAF are already on the market, but are a niche product without a significant share of the global aviation market. Currently

the vast majority of SAF is bio-kerosene, a relatively mature technology, yet ultimately limited in the long-term scalability because of its environmental effects and limited cultivable land. The production of bio-kerosene is also directly competing with agricultural food or fodder production.

A promising solution are drop-in fuels made from H_2O and CO_2 by solar-driven processes [5, 6, 7]. Among the many possible approaches, the thermochemical path using concentrated solar radiation as the source of high-temperature process heat offers potentially high production rates and efficiencies [8]. The solar driven thermochemical cycle for co-splitting of CO_2 and H_2O into syngas — a specific mixture of CO and H_2 — which can be further processed to drop-in fuels (e.g. synthetic kerosene) via Fischer-Tropsch (FT) synthesis or other gas-to-liquid processes, are considered a promising path for the production of SAF [9, 10].

If the required CO_2 is obtained directly from atmospheric air this pathway can deliver truly carbon neutral fuels [11]. The resulting synthetic fuel is carbon neutral because only as much CO_2 is released to the air upon its combustion as was taken from the air for its production, hence closing the anthropogenic carbon cycle. If H_2O is also co-extracted from air [12], feedstock sourcing and fuel production can be co-located in desert regions with high solar irradiation and limited access to water resources. This pathway hence also does not compete for land use with agricultural food or fodder production. Obviously, there is also no need for removal of any impurities (e.g. sulfur compounds, salts, heavy metals), as it is the case for hydrocarbons derived from petroleum. Moreover, the combustion of FT-based jet fuel, which is aromatic- and sulfur-free and is certified as aviation turbine fuel after the standard specification ASTM 7566, showed dramatic reductions in soot emissions compared to fossil-based jet fuel [13].

Solar fuel production using H_2O and CO_2 obtained through direct air capture (DAC) has so far largely been limited to bench-top [14, 15] or pilot-

scale [16, 17] demonstrations of individual steps. A combined PV-electrolysis system [18] produced solar fuels from water and captured CO_2 , but the set-up was not optimized and coupling of intermittent solar hydrogen production with continuous non-solar hydrocarbon synthesis necessitated the co-feeding of fossil-derived syngas. Fuel production from CO_2 and H_2O not captured from air in a thermochemical 4kW redox reactor of similar technology to the one used in this thesis and with a FT GTL unit has previously been demonstrated under laboratory conditions in a solar simulator [19]. Most recently, the production of FT fuel from bottled CO_2 and H_2O (no DAC) has been demonstrated in a 50 kW scaled up version of the reactor on a solar tower [20].

While individual steps of such a process scheme have been implemented, this thesis demonstrates the operation of the entire thermochemical solar fuel production chain, from H_2O and CO_2 captured directly from ambient air to the synthesis of drop-in transportation fuels (e.g. methanol, kerosene), with a modular 5-kW_{thermal} pilot-scale solar system operated under real field conditions.

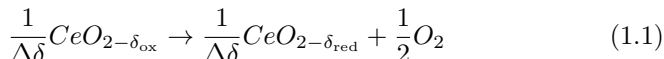
1.2 The Ceria Cycle

To effect the solar driven thermochemical splitting of CO_2 and/or H_2O into CO and/or H_2 various metal oxides have previously been proposed and investigated to perform the two-step redox cycle, with concentrated solar radiation used as the heat source for the reduction step of the cycle [8, 21, 22, 23]. Among the proposed metal oxides are zinc oxides [24, 25, 26, 27, 28], iron oxides [29, 30, 31, 32], ferrites [33, 34, 35] or nonstoichiometric metals such as un-doped [36, 37, 38, 39, 19, 40, 41] and doped [42, 43, 44] ceria or perovskites [45, 46, 43, 47, 48, 49].

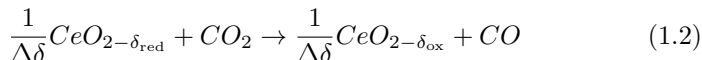
Cerium dioxide CeO_2 , mostly referred to as ceria, has emerged as an attractive redox material because of its rapid kinetics [50, 51, 52], crystallo-

graphic stability over a large range of temperatures and reduction extents [38, 53] and abundance [37, 54]. It also offers a relatively large oxygen exchange capacity (i.e. high nonstoichiometry) for a nonstoichiometric metal oxide [55, 56, 57]. The rare earth metal Cerium Ce is the most abundant rare earth metal, and is about as common as copper in the earth's crust [58]. Nowadays ceria is widely considered the state of the art material for solar thermochemical CO₂ and/or H₂O splitting. Although some alternative redox materials, e.g. perovskites [59, 49, 60] and hercynite [61], exhibit superior redox performance, they have not yet proven to be as stable as ceria.

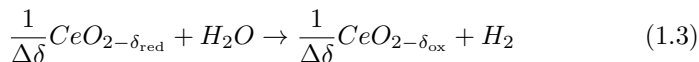
The thermochemical redox cycle based on non-stoichiometric ceria (CeO_{2-δ}) consists of an endothermic reduction to release O₂, followed by an exothermic oxidation with CO₂ and/or H₂O to produce CO and/or H₂ and is represented by the following reactions and the corresponding standard enthalpy changes: Reduction ($\Delta H^\circ \approx 475$ kJ per 1/2 mole O₂):



Oxidation with CO₂ ($\Delta H^\circ \approx -192$ kJ/mol CO₂):



Oxidation with H₂O ($\Delta H^\circ \approx -234$ kJ/mol H₂):



δ denotes the non-stoichiometry — the measure of the redox extent which, in equilibrium, is a function of temperature and oxygen partial pressure. Ceria is not consumed in the process and the net overall reactions are:



and



Note that the fuel (H_2 , CO) and O_2 are generated in separate steps and are thus avoiding the formation of explosive mixtures and the need for high-temperature gas separation. This also allows both reactions to be performed in the same reactor.

In principle, the redox cycle can be operated under a temperature-swing mode and/or a pressure-swing mode to control the oxygen exchange capacity of ceria $\Delta\delta = \delta_{\text{red}} - \delta_{\text{ox}}$, and thereby the fuel yield per cycle. Isothermal operation, i.e. only pressure-swing mode, suffers from low $\Delta\delta$ imposed by the thermodynamics [62, 63, 64, 37, 40]. For example, isothermal cycling at $T_{\text{reduction}} = T_{\text{oxidation}} = 1200^\circ\text{C}$ with a pressure swing between 0.1 mbar and 1 bar, yields only $\Delta\delta = 0.003$. In this thesis a combination of both temperature and pressure swing is applied to maximize $\Delta\delta$ and thereby the fuel yield per cycle. For typical operating conditions of the reduction step at 1500°C and 0.1 mbar and the oxidation step at 900°C and 1 bar, thermodynamics predict an order of magnitude higher value, $\Delta\delta = 0.04$.

1.3 Previous Reactor Designs

Solar reactor concepts previously investigated for effecting the ceria redox cycle have included moving [65, 66, 67, 68, 69] and stationary [37, 70, 17] bulk structures, packed beds [71, 72, 64], moving beds [73, 74, 75], and aerosol flow [41, 76] of particles. Of special interest is the solar reactor concept based on a cavity-receiver containing reticulated porous ceramic (RPC) structures made of ceria [20, 40, 77], which enhance heat and mass transfer. This is also the concept applied in the design of a 50 kW solar reactor [20], tested in a solar tower, achieving the highest measured solar-to-fuel energy efficiency to date (efficiency defined in chapter 2.5 Eq. 2.4).

The development of the solar cavity reactor discussed in this thesis for performing the ceria cycle evolved from its early design with monolithic ceria [37] to a reactor containing ceria felt [78], to a reactor with single scale

porous ceria [39], and finally to its present configuration with dual scale reticulated porous structures [40]. The version discussed in this thesis is a slightly up scaled 5 kW version of the 4 kW reactor presented in Ref. [40] with a 50kW up scaled version installed on a solar tower [20] to set the aforementioned highest measured solar-to-fuel energy efficiency. In contrast to the 4kW laboratory scale reactor of Ref. [40], the reactor studied in this thesis is operating under real field conditions (i.e. directly exposed to concentrated sunlight and performing under varying solar power inputs and changing external conditions). The reactor is also operated as part of a two reactor system.

1.4 Thesis Goal and Outline

The main goal of this thesis was to demonstrate for the first time the entire process chain from sunlight and ambient air to liquid drop in fuels in one setup under real field conditions. This setup was developed and built on the roof of ETH's machine laboratory in Zurich, Switzerland.

The thesis is structured in 4 main chapters that describe the developed and built setup, show experimental results of the demonstration of the entire process chain, present an in depth parameter study of the solar redox unit controlling the syngas composition, describe the implemented automation of the fuel system and present a dynamic reactor model of the solar redox reactor.

Chapter 2 presents the setup of the entire process chain from sunlight and air to solar fuels under real field conditions. The different units and components are introduced and their integration into the system is discussed. The main focus lies on the solar redox unit as the core process. The chapter further shows experimental results demonstrating the stability and robustness of the system, examples for the different cycles targeting syngas for methanol or FT synthesis and the results of a production campaign leading to the first solar methanol produced from sunlight and air via the thermochemical pathway.

Chapter 3 presents a parameter study of the solar reactor operation. The parameter study for the reduction part of the cycle shows the dependencies of performance indicators such as fuel yield and $\eta_{\text{solar-to-syngas}}$ on the varying reduction parameters p_{reactor} , \dot{m}_{Ar} and $T_{\text{reduction-end}}$ for various P_{solar} . The parameter study for the oxidation part of the co-splitting cycle shows the influence of the oxidation parameters $T_{\text{oxidation-start}}$, \dot{m}_{CO_2} and $\dot{m}_{\text{H}_2\text{O}}$ on the performance indicators V_{syngas} , X_{CO_2} and $\eta_{\text{solar-to-syngas}}$ for different syngas quality ratios $R_{\text{H}_2:\text{CO}}$. These results for the co-splitting of CO_2 and H_2O are compared to cycles analysing the splitting of CO_2 and H_2O in separate redox cycles.

Chapter 4 details the program logic of the automation of the solar fuel system and its implementation. The chapter further introduces an auto-optimisation scheme that executes online mass and energy balances to guide performance improvement. To the best of the authors knowledge, this is the first-ever implementation of a fully automated auto-optimization scheme for the control and operation of a solar reactor effecting the thermochemical redox splitting of CO_2 and H_2O .

Chapter 5 describes a dynamic grey box model of the redox reactor based on energy and mass balances. The chapter shows results of a a simplified model and an example of an application by comparing a simulated two and three reactor system reaching constant and continuous cycling conditions.

DEMONSTRATION OF THE ENTIRE PROCESS CHAIN FORM SUNLIGHT AND AIR TO SOLAR FUELS ¹

This chapter focusses on the demonstration of the entire process chain from ambient air and sunlight to liquid solar fuels. The chapter shows the experimental installation and details the different components, followed by demonstrating the stability of the solar redox unit by full day CO₂-splitting cyclic runs and introducing characteristic H₂O and CO₂ co-cycles targeting syngas for both methanol and FT synthesis as the downstream GTL process. The chapter shows full day syngas production for downstream methanol synthesis and summarises a production campaign to collect syngas for the production of methanol. The chapter concludes with an efficiency analysis of the solar fuel system.

¹Parts of this chapter have been published as: Schäppi, R. *et. al.*, Drop-in fuels from sunlight and air. *Nature* 601, 63-68 (2022). <https://doi.org/10.1038/s41586-021-04174-y>

2.1 System Design and Experimental Setup

Figure 2.1 sketches the solar fuel system, installed on the roof of the ETH's Machine Laboratory Building in Zurich. Its three essential units are: 1) the direct air capture (DAC) unit which co-extracts CO_2 and H_2O directly from ambient air; 2) the solar redox unit which converts CO_2 and H_2O into a desired mixture of CO and H_2 (syngas) using concentrated sunlight; and 3) the gas-to-liquid (GTL) unit which converts syngas to liquid hydrocarbons or methanol.

2.1.1 DAC Unit

The DAC unit applies adsorption-desorption cycles based on temperature and pressure swing to an amine-functionalised sorbent to concurrently extract CO_2 and H_2O from ambient air [12].

The installed DAC unit is a Climeworks Demonstrator CW4113 set up inside a 20ft container to protect it from the environment. Ambient air is sucked into the unit and passed through the amine-functionalised sorbent packed bed. Adsorption proceeds at ambient temperature and pressure for 180 minutes per cycle, followed by the desorption at 95°C and 0.1-0.3 bar for 43 minutes per cycle. The unit can process an air flow of $2000\text{ m}^3/\text{hr}$ with 5.5 cycles/day, yielding around 8 kg/day of CO_2 with a measured purity of 98.2% (the remainder being air, CO_2 content measured by IR detectors in a Siemens Ultramat-23 and verified by external analysis done by Intertek) and 20-40 kg/day of water (depending on relative air humidity) with contaminants below the 0.2 ppm detection limit (external H_2O sample analysis done by Intertek). The exhaust air leaves the unit during the adsorption step with about 40-70% of its initial CO_2 content captured. The captured CO_2 stream exiting the DAC unit during the desorption step is collected in a 1.2 m^3 balloon-type buffer reservoir at ambient pressure. Subsequently the CO_2 is passed through additional water traps and an activated alumina adsorption tower before it is compressed to maximum 12 bars and stored in a 750 l steel buffer tank. Water is condensed out of the desorption stream and

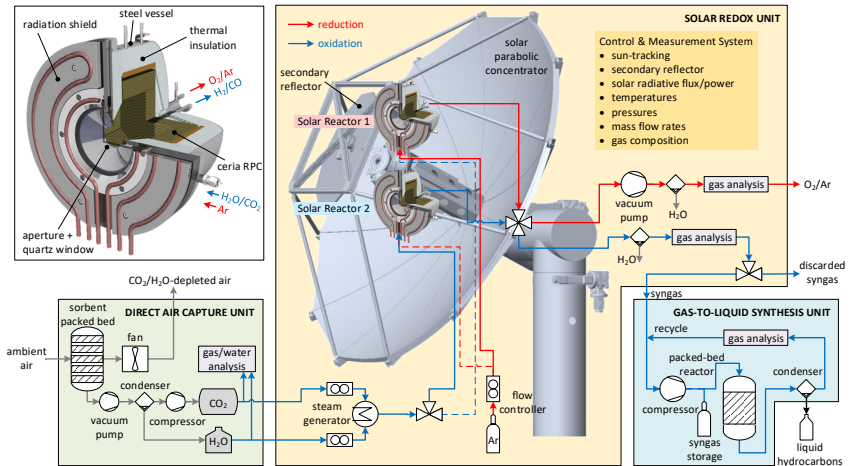


Figure 2.1: Simplified process chain of the solar fuel system integrating three thermochemical conversion units in series: 1) the direct air capture (DAC) unit which co-extracts CO_2 and H_2O directly from ambient air; 2) the solar redox unit which converts CO_2 and H_2O into a desired mixture of CO and H_2 (syngas) using concentrated solar energy; and 3) the gas-to-liquid (GTL) synthesis unit which finally converts syngas to methanol or liquid hydrocarbons. Two identical solar reactors are positioned at the focus of the solar concentrator for performing both redox steps of the thermochemical cycle simultaneously by alternating the concentrated solar input between them. While one solar reactor is performing the endothermic reduction step on sun, the second solar reactor is performing the exothermic oxidation step off sun. Red arrow indicates reduction (Eq. 1.1); blue arrow indicates oxidation (Eq. 1.2 and 1.3). Dimensions are not to scale. Upper-left insert: Cross-section of the solar reactor featuring a cavity-receiver containing a reticulated porous ceramic structure (RPC) made of pure ceria for performing the thermochemical redox cycle.

separately stored in a plastic buffer tank. Both CO_2 and H_2O are delivered from their buffer tanks to the solar redox unit according to demand. If the CO_2 tank reaches 12 bars, usually after 48 hours operation, the DAC unit automatically stops production and goes in to idle state until demand is present. The full CO_2 buffer tank can typically support between 3 to 18 days of operation of the solar redox unit, depending on the specific fuel targeted, e.g. 3 to 5 days for CO_2 -splitting only. The buffer tanks also balance the mismatch between the amount of water obtained in the DAC unit ($\text{H}_2\text{O}:\text{CO}_2$ 6.1-12.2, depending on the relative air humidity) and that used in the solar redox unit ($\text{H}_2\text{O}:\text{CO}_2$ 12.5-24.9, depending on the targeted fuel), with excess unreacted water collected downstream of the solar reactor recycled.

The calculated specific energy requirements of the DAC unit are 13 $\text{kJ/mol}_{\text{CO}_2}$ of mechanical work (vacuum pump operated at 0.05 bar desorption pressure/1 bar exit pressure; 0.7 efficiency of isothermal compression), and 493-640 $\text{kJ/mol}_{\text{CO}_2}$ of heat at 95°C . These energy values were obtained for amine-functionalized nanofibrillated cellulose sorbent with a measured specific CO_2 capacity in the range 0.32-0.65 mmol/g , a specific H_2O capacity in the range of 0.87-4.76 mmol/g , and an air relative humidity in the range 20-80% [12]. For a targeted sorbent's specific CO_2 capacity of 2 mmol/g , the heat requirement would be reduced to 272-530 $\text{kJ/mol}_{\text{CO}_2}$, depending strongly on the amount of co-adsorbed water. Obviously, higher relative humidity results in more water adsorbed and, consequently, higher thermal energy requirements during the desorption step.

2.1.2 Solar Redox Unit

Solar Optics and Solar Power Measurement

The optical design and characterization of the solar concentrator, comprising a primary sun-tracking solar paraboloidal dish coupled to a secondary planar rotating reflector, is found in Ref. [79] and summarised here.

Fig. 2.2 a) shows a schematic of the solar concentrator comprising a

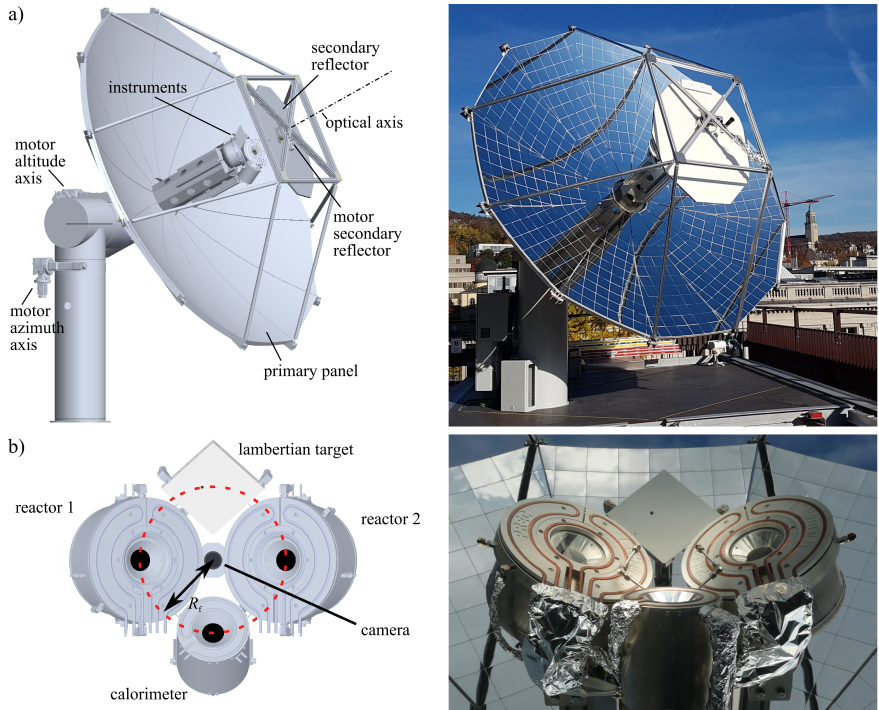


Figure 2.2: Schematics and photographs of the optical solar dish system: a) 3D rendering of the primary two-axis sun-tracking parabolic dish and secondary rotating flat reflector; b) Installed instruments: solar reactors, water-calorimeter, and Lambertian target. The dashed circle indicates the 0.4 m diameter focal point trajectory during rotation of the secondary reflector. Figure reproduced from Ref. [79].

primary parabolic reflector coupled to a secondary rotating planar reflector. The primary reflector is a 4.4 m diameter, 2.2 m focal length parabolic reflector consisting of 12 individual panels with a rim angle of 53° and projected total and illuminated area of 15.3 m^2 and 12.9 m^2 , respectively. For safety purposes, control of the tracking and orientation of the primary reflector is kept separate from the controls of the rest of the solar redox unit. The two-axis (azimuth/altitude) sun-tracking of the primary parabolic dish by means of two three phase AC motors (Lenze IE1 MD071) is based on pre-calculated curves [80] and fine-tuning with a solar sensor (Solar MEMS ISS-D5, precision = 0.005°). The secondary reflector is a 1.71 m^2 -area 24° -tilt planar reflector in the shape of an irregular dodecagon. It is positioned such that all rays incoming from the primary reflector are intercepted and directed to the focal point. The secondary reflector is rotated by means of a slotless, brushless rotary motor (Aerotech BMS60). For both primary and secondary reflectors, the mirror surface consists of $160 \times 160 \times \text{mm}$ highly reflective back-silvered float-glass reflectors (Fast Glass), glued onto the respective support structure. The combined optical system achieves a geometrical concentration ratio $C_{\text{geo}} = A_{\text{dish}}/A_{\text{reactor}} = 4560$ for the 60mm diameter reactor aperture and has 11.1% shading losses and 1.7% blocking losses.

This optical configuration allows to rotate the concentrator focal point among 4 positions by rotating the secondary mirror, as depicted in Fig. 2.2 b). The four instruments mounted in the focal plane are:

- The two solar reactors (details see following section).
- A water-calorimeter for solar radiative power measurements.
- A water cooled Lambertian (diffusely-reflecting) target for solar flux distribution measurements.

This arrangement enables the operation of the two solar reactors side-by-side for performing both redox reactions simultaneously by alternating the solar radiative input between them while making continuous and uninterrupted use of the incoming concentrated sunlight. It also provides the

possibility for solar power measurements while the reactors are in operation (i.e. solar power measurement between the reactors are on sun).

Fig. 2.2b also shows the position of the calibrated CCD camera (Basler scA1400-17gm, manual zoom lens RICOH FL-CC6Z1218-VG, neutral density filters ND 4.8) installed at the center of the four instruments along the optical axis. Given the position along the optical axis the camera always points at the current focal point via a 320 x 320 mm mirror at the centre of the secondary reflector while not being hit by direct solar radiation itself (shaded by the secondary reflector). This allows the camera to be used for flux measurements on the lambertian target, a 200 x 200 mm Al₂O₃ plasma-coated and internally water cooled plate. The camera is also used for optical control and alignment of the other instruments. Alignment of the instruments is also aided by 4 lasers mounted at the rim of the primary mirror with their optical path crossing in the focal point.

The solar radiative power delivered by the solar concentrating system was measured using a water-cooled calorimeter made of a selectively coated Cu-coiled cavity with the same water cooled front containing the 30 mm-radius aperture as the solar reactors. This measurement is needed as the solar power input cannot be measured on the reactors itself. The cooling water flow through the main calorimeter cavity was measured with a magnetic inductive flow meter MAG-VIEW in the water inlet line. Water temperatures at the inlet and outlet of the calorimeter were measured with two Pt100 resistance temperature detectors. Additional K-type thermocouples were installed for temperature surveillance of the outer hull.

The radiative power incident on the system P_{solar} can be determined using the temperature difference $\Delta T = T_{\text{out}} - T_{\text{in}}$ of the water inlet and outlet flow of the calorimeter (equation 2.1). Where \dot{m}_{water} is the measured water mass flow rate and $c_{\text{p,water}}$ the specific heat capacity of the cooling water.

$$P_{\text{solar}} = \dot{m}_{\text{water}} \cdot c_{\text{p,water}} \cdot \Delta T = \dot{m}_{\text{water}} \cdot c_{\text{p,water}} \cdot T_{\text{out}} - T_{\text{in}} \quad (2.1)$$

The direct normal irradiation DNI is measured with a sun tracking Pyrhe-

liometer (EKO Instruments MS-56, mounted on a STR-21G sun tracker). As the DNI is proportional to the measured P_{solar} , the DNI is used to calculate the current P_{solar} incident on the reactor based on the last calorimeter measurements.

For a normalized DNI of 1 kW/m^2 , the concentrating setup delivers a solar radiative power of up to 7680 W to the 30-mm radius aperture of the solar reactor with a mean and peak solar concentration ratio of 2710 suns and 5010 suns, respectively, yielding an overall optical efficiency of 59.6%. Detailed optical analyses based on experimentally measured and numerically simulated data identify feasible measures to increase this optical efficiency to 82% [79].

Solar Reactors

The two identical 5-6 kW solar reactors installed, are a slightly up scaled version of the 4 kW reactor previously tested with a solar simulator and described in Ref. [40]. Key differences are the cavity size and aperture diameter. Since only the endothermic reduction step requires a solar input, two identical solar reactors are employed and perform both redox steps simultaneously by alternating the concentrated solar input between them. While one solar reactor is performing the endothermic reduction step on sun, the second solar reactor is performing the exothermic oxidation step off sun.

Figure 2.3 shows a 3D rendering of the solar reactor. The core of the reactor is a $110 \times 190 \times 190 \text{ mm}$ octagonal cylinder cavity out of reticulated porous ceramic (RPC), consisting of 8 identical trapezoidal prism side bricks and an octagonal back plate. The trapezoidal prism side bricks measure $110 \times 79 \times 35 \text{ mm}$. The regular octagon back plate measures 120 mm medium diameter/span and 35 mm thickness. The RPC foam-type structure made of pure ceria is directly exposed to the solar irradiation, enabling volumetric absorption and uniform heating (details see following section). The RPC core is embedded in a circular 306 mm diameter \times 194 mm stainless steel shell, filled with alumina thermal insulation type Zicar Zirconia BusterM-35 and closed off with a water cooled aluminium front and radiation shields.

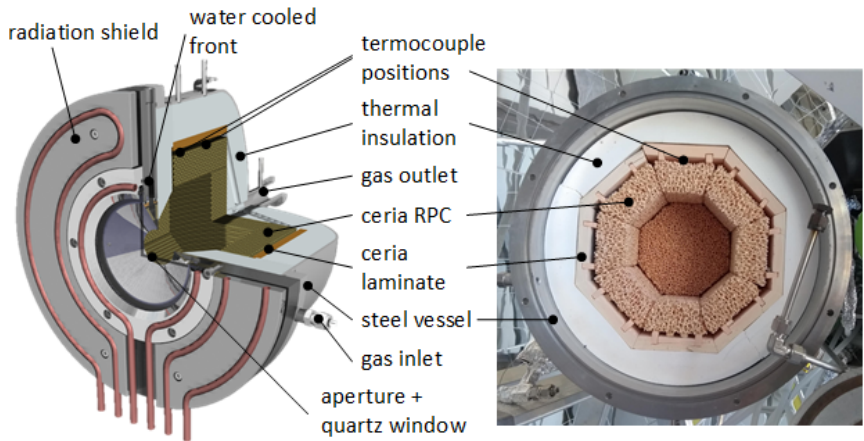


Figure 2.3: 3D rendering of the solar reactor (left) and view of the open reactor cavity with the aluminium front and first insulation layer removed (right). Labeled are the radiation shield, water cooled front, thermocouple positions, thermal insulation, gas outlet, ceria RPC, ceria laminate, steel vessel, gas inlet, aperture + quartz window.

The 60 mm diameter circular aperture is sealed by a 6 mm-thick clear fused quartz disk window for the access of concentrated solar radiation. Sealing the aperture with a window allows the reactor to be operated under vacuum. To avoid any potential side reactions between the ceria RPC and the insulation, there is a layer of 12.7 mm (1/2 inch) ceria laminate type CeFB, with spacers to facilitate a 2-5 mm gap between the RPC and the laminate for better gas flows through the RPC. Gas flows enter the reactor through two inlet ports in the reactor front, entering the cavity through a ring shaped opening directly behind the window to avoid ceria deposition on the window. To avoid forcing hot steam over the water cooled aperture cone, the steam is directly injected into the cavity through a 6mm ceramic tube from an additional inlet port in the reactor front, entering the cavity through the front insulation below the aperture. Gases leave the reactor through a single KF45 gas outlet at the back of the reactor, forcing the gas flows through the RPC. Temperatures inside the reactor were measured at the back of the RPC with B-type thermocouples. The nominal reactor temperature reported in this thesis is defined as the average of the measured temperatures at the back of the top RPC (position indicated in Fig. 2.3). This value serves as a reference temperature to control the reactor cycling. Note that the inner most layer of the RPC is directly exposed to the incoming high-flux irradiation and, therefore, is likely hotter than the reference temperature. Evidently, significant temperature gradients occur within the RPC. Other temperatures such as gas inlet and outlet temperatures, shell temperatures and safety control temperatures were measured using K-type thermocouples. Reactor pressures were measured using Thermovac TTR 101N pressure sensors installed at measuring ports below the reactor.

The following paragraph shows the results of a rough energy balance of the solar reactor based on experimental measurements. Material in this paragraph has been extracted from "*V. Hüsler, Co-Splitting of CO₂ and H₂O in a Solar Dish Reactor System — Parameter Analysis and Automation for Syngas Production*", (Master Thesis, 2021), supervised by R. Schächli. The

solar energy entering the reactor cavity is measured with the calorimeter and adjusted for the transmissivity of the quartz window. Re-radiation losses are estimated based on the inner RPC cavity temperature. As this temperature could not be measured directly (measurement on the back of the RPC), the assumptions for this temperature are based on the heat transfer model by Ref. [81]. Cooling losses through the water cooled front of the reactor are calculated based on measurements of cooling water flow and inlet/outlet temperatures. Conduction losses are estimated using the measured RPC temperatures inside the reactor and various temperature measurements on the steel shell of the reactor. It has to be noted that this energy balance only serves as a rough estimation of the losses and is not a detailed modelled analysis. The energy balance shows that over the entire cycle, 40% of the solar input is lost to the surroundings by re-radiation through the aperture, closely followed by 37% that is removed with the aperture cooling water. This clearly hints at possible improvement options, the water cooling for example could be replaced with oil cooling at higher temperatures. 16% are conductive and convective losses to the surroundings, while 6% are used for heating up gasses. This leaves only about 1% of the solar input to be transformed into reaction heat. It has to be mentioned, that this analysis (especially of the re-radiation losses) is highly dependent on assumptions, e.g. the assumptions for the inner cavity temperature. Analysing only the reduction step, one finds that 19% of the solar input is used for heating up the RPC, with 33% of the input heating up other components. Re-radiation losses account for 18%, losses through the aperture cooling water 19% and conductive/convective losses to the surroundings 6% of the solar input. This leaves 2% for reaction heat of the reduction and 2% for gas heating.

RPC

The 35 mm ceria RPC bricks inside the reactor were fabricated using the replica method and feature a dual-scale interconnected porosity in the mm and μm scales. The mm-size pores provide enhanced volumetric absorption during the reduction step (enhanced heat transfer) and the μm -size pores

within the struts provide enhanced mass transfer, important during the oxidation step.

Basis of the RPC is a 7ppi reticulated polyurethane (PU) foam coated three times with a ceria slurry. The content of the slurry can be found in table 2.1. Note that the zirconia milling balls are removed from the slurry before the coating process and can be recycled. The first, second and third coat were done with a high, medium and low viscosity slurry, respectively and between every coat the RPC bricks were air dried for 24 hours. After the last coat the RPC were dried in an oven at 90°C for 1h before they were sintered in a high temperature furnace. The ramp profile (heating rates) of the sintering process applied was as follows: 1 K/min to 600°C , 2 K/min to 800°C , 1 K/min to 1100°C , 1100°C constant for 4 h, 1 K/min to 1600°C , 1600°C constant for 8 h, -3 K/min to 1000°C , -0.5 K/min to ambient. After the sintering process the RPC were cut into shape to be assembled in the reactor. The final sintered RPC is made out of pure ceria as the support structure and pore former are evaporated during the sintering process.

Figure 2.4 shows scanning electron microscope images (SEM) of RPC struts in 250x and 1000x magnification of a strut cross section and surface of an unused RPC compared with a piece of RPC from the same batch after 43 days and over 200 hours on-sun, performing 239 CO₂ and H₂O splitting redox cycles. Clearly visible is the microporosity. The triangular shape in the center of the strut stems from the support PU foam that got removed during sintering. There is no clear degradation visible when comparing the two samples. However, the RPC brick itself was very brittle upon touch and showed weaker mechanical stability compared to the unused RPC.

Auxiliary Systems

Upstream of the reactors, CO₂ and H₂O are fed from their respective buffer tanks through a mass flow controller directly into the reactors (CO₂-splitting) through 8 mm pipes or are co-fed through a steam generator (co-splitting with H₂O) connected to the reactors through 8 m heated lines type IHH

| Component | Specification | Quantity |
|----------------------------|---|---------------|
| CeO ₂ Powder | <5 μm, Sigma-Aldrich | 1000 g |
| Carbon pore former | SIGRAFIL C M150-3.0/200 UN | 92 g |
| Deionised H ₂ O | - | 160/215/270 g |
| Dispersing agent | Dolapix CE 64 | 8.3 g |
| Zirconia milling balls | 10 mm, Yttria-Stabilized-Zirconia | 500 g |
| PVA-40 | Optapix PA 4G in 40% wt. H ₂ O | 50 g |
| Anti-foaming agent | Contraspum KWE | 20 drops |

Table 2.1: Ingredients for ceria slurry for RPC production with quantities reported for a reference batch containing 1000 g ceria powder. Quantities of deionised H₂O reported for high/medium/low viscosity slurry. Ingredients PVA-40 and Contraspum KWE only added after 24 hours of milling. Zirconia milling balls removed after milling.

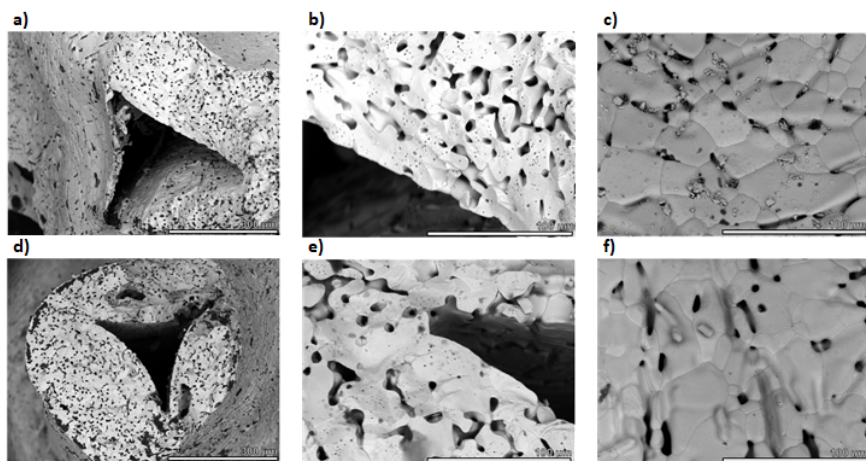


Figure 2.4: SEM images of RPC struts — Strut cross section 250x magnification (a, d) and 1000x magnification (b, e) and strut surface 1000x magnification (c, f) for unused RPC (a, b, c) and used RPC (d, e, f) after 293 on-sun redox cycles.

205 (8 mm inner diameter) set at 150°C . Gas flow rates were regulated and measured using Bronkhorst EL-FLOW Select electronic mass flow controllers and meters. Steam was generated by a Bronkhorst controlled evaporator mixer.

Downstream of the reactors, a valve block (valves 1) connects the reactors with either the vacuum pump during the reduction step (Eq. 1.1) or the gas analysis and downstream GTL unit during the oxidation step (Eq. 1.2 and 1.3). The connection to the vacuum pump installed at the bottom of the solar dish is kept at KF25 diameter to reduce friction in the evacuation process. A multistage dry roots vacuum pump Adixen ACP 28CV (results presented in chapter 2) or a lubricated vane vacuum pump PVR EU 45 (results presented in chapter 3, 4 and 5) in combination with multiple valves (Pfeiffer Vacuum AVC 025 PA) was used to evacuate the reactors during reduction. Product gas composition was analyzed on-line by gas chromatography (Agilent Technologies) and Siemens Ultramat-23 and Calomat-6 gas analysis units (electrochemical sensors for O₂, IR detectors for CO and CO₂, thermal conductivity based detectors for H₂). Unreacted H₂O was condensed out of the product stream before the gas analysis using automatic gravity based condensate drains ADS-T and can be recycled.

2.1.3 GTL Unit

The last step of the thermochemical production chain from sunlight and air to liquid solar fuels is the GTL synthesis in the GTL unit. This last step is a mature technology that is already implemented also in industrial scale commercial plants. For demonstration purposes, the GTL process implemented was methanol synthesis. However, with the same setup and changed catalyst, reactor temperature and reactor pressure it would also be possible to do FT-synthesis as previously demonstrated [19].

Downstream of the solar redox unit (Fig. 2.1), the O₂ stream evolving from the reduction step is analysed and vented. The syngas stream evolving from the oxidation step is analysed and sent to the GTL unit. Before

entering the GTL unit the product gas passes through a discarding valve where the syngas from the reactors can be directed into the GTL unit or discarded/vented. This valve plays a key role in controlling the syngas quality for the synthesis as it allows to discard unwanted parts of the syngas (e.g. syngas with high content of Ar or unreacted CO₂).

The GTL unit itself consists of a dual stage compression unit with buffer gas storage, a packed bed reactor where the synthesis takes place, a condenser and a gas analysis system (see Fig. 2.1). The syngas from the solar redox unit was compressed at up to 250 bar using the two stage compressor station ILS 331 (see labeled components in Fig. 2.5). The gases enter the compression unit into a 50 L bag type buffer storage. Upon entering, a small fraction of the syngas is fed to an additional O₂ sensor. These two independent O₂ measurements in combination with a reduced copper catalyst reactor (first gas conditioning reactor) at 175°C for O₂ removal are a safety measure to avoid any traces of O₂ in the compressed syngas. Should any of the O₂ detectors be triggered, the syngas is automatically vented. After passing through the O₂ reactor and a drying column, the syngas from the bag type buffer storage is first compressed to a 10 bar intermediate buffer and finally to up to 250 bar in a 5 L aluminium gas cylinder for storage. Another safety issue is the potential formation of nickel tetracarbonyl. This is addressed by the usage of non-nickel containing aluminium tubing as well as a second gas conditioning reactor at 250°C to destroy any potentially formed nickel tetracarbonyl after the last compression step. From the 5 L gas cylinder, the syngas is then delivered into the GTL reactor as per demand.

Storing the syngas before the GTL reactor means that the GTL unit can in principle be operated continuously round-the-clock. Intermittent daily startup-shutdown operation of the GTL unit for methanol synthesis at the lab scale is possible by purging the catalyst with H₂-free gas upon shutdown to avoid deactivation [82]. However, while this option reduces the cost of storing syngas, it is generally avoided at a large scale due to the complications associated with operating intermittently an oversized GTL unit.

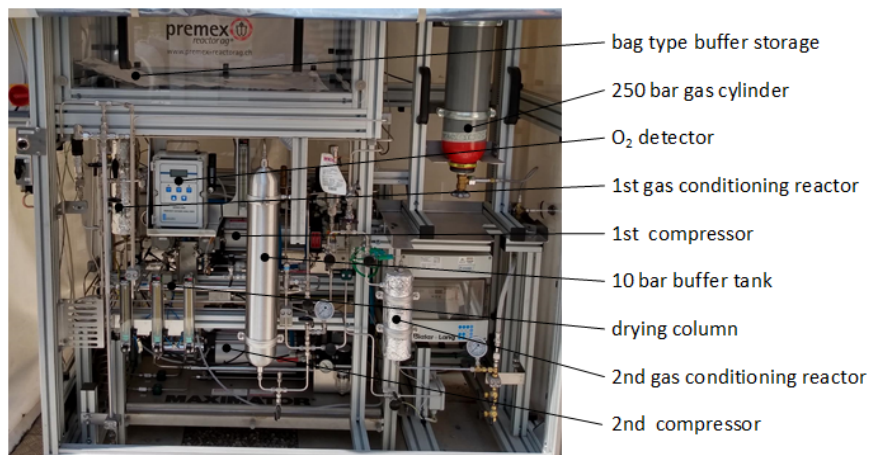


Figure 2.5: Photo of installed compression station with labeled components.

The final syngas processing to methanol in the GTL reactor uses a commercial Cu ZnO-Al₂O₃ catalyst (Product No. 45776, Alfa Aesar) in a packed-bed tubular reactor at 230°C and 50 bars. The installed reactor of the GTL synthesis unit was a Microactivity Effi (PID Eng&Tech) and the used syngas flow into the reactor was 0.3 L/min. The produced methanol is condensed out of the product stream and collected in a glass vial.

The measured single-pass molar conversion of the GTL unit was 27%. External analysis by the company Intertek shows a methanol purity of 65% with the rest being water. Other contaminants were below the detection limit of < 1 ppm for ethanol and butanol or < 10 ppm for propanol.

The remaining unconverted syngas was recycled for multiple passes through the GTL unit (see Fig. 2.1). This implemented recycling loop again stresses out the importance to control the composition of syngas suitable for the GTL process. The goal is to match the composition of the unreacted syngas to the one entering the GTL unit from the reactors. This takes careful adjustments in the reactor operation and was implemented in this thesis. Another option, not followed up on in this thesis, but possible to implement

with the described system, would be to compensate for the imbalances in the recycled syngas by continuously adjusting the syngas composition from the reactors. Since Ar concentration increased in the recycled syngas with each pass, the recycled syngas was discarded after 6 consecutive passes, resulting in a total molar conversion of 85%.

2.2 Cycles for CO₂-splitting ¹

2.2.1 Representative CO₂-splitting Cycle

Figure 2.6 shows a representative redox cycle for CO₂-splitting, operated under a temperature/pressure-swing mode. Plotted as a function of time are the temperature at the outer perimeter of the RPC (green), reactor pressure (red) and gas evolution of O₂ released during solar reduction (black) and CO produced during oxidation (blue). The cycle consists of three phases: 1) An on-sun reduction phase of duration $\Delta t_{\text{reduction}}$, during which the solar reactor is exposed to concentrated sunlight at a mean solar radiative power $P_{\text{solar,mean}}$ through its aperture, and heated from the reduction-start temperature $T_{\text{reduction-start}}$ up to the desired reduction-end temperature $T_{\text{reduction-end}}$ (in the case of Fig. 2.6 up to 1400°C), where the solar input is diverted by rotating the secondary reflector. During this phase, the reduction (Eq. 1.1) proceeds to release O₂ from CeO₂ assisted through a decreased total pressure p_{reactor} (down to 4 mbar for Fig. 2.6) by means of a vacuum pump and an Ar sweep gas with flow rate \dot{m}_{Ar} . 2) An off-sun cool-down phase of duration $\Delta t_{\text{cool-down}}$ at ambient pressure without flow, during which the solar reactor is off-sun and re-pressurized by injecting CO₂, and cools down to the oxidation-start temperature $T_{\text{oxidation-start}}$. During this phase, part of the CO₂ in the reactor already reacts with the ceria to form CO (Eq. 1.2). 3) An off-sun oxidation phase of duration $\Delta t_{\text{oxidation}}$ at below $T_{\text{oxidation-start}}$

¹Parts of this chapter have been published as: Schäppi, R. *et. al.*, Solar Thermochemical Splitting of CO₂ in a Modular Solar Dish-Reactor System. *Proceedings of the ISES Solar World Congress 2019, Santiago, Chile, 1405-1408* (2020). <https://doi.org/10.18086/swc.2019.24.08>

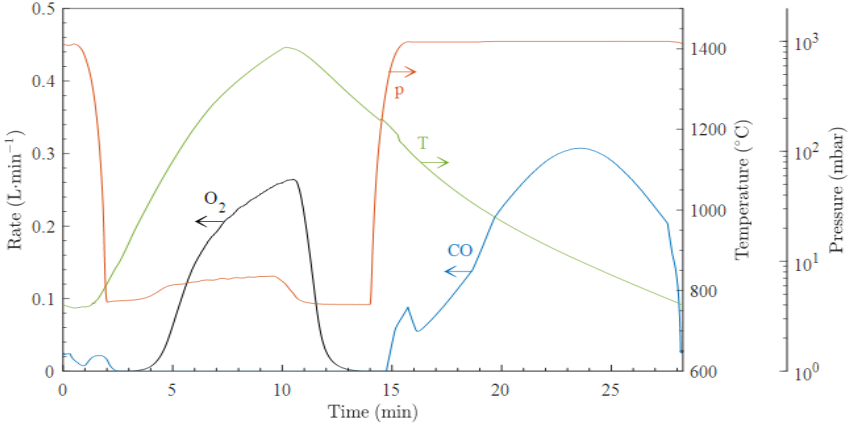


Figure 2.6: Representative CO₂-splitting Cycle. Measured RPC temperature (green), reactor pressure (red) and gas evolution rates (O₂ black and CO blue) over time for a CO₂-splitting cycle. Reduction up to $T_{\text{reduction-end}} = 1400^{\circ}\text{C}$ with $\dot{m}_{\text{Ar}} = 1 \text{ L/min}$ and $p_{\text{reactor}} = 4\text{mbar}$. Oxidation started at $T_{\text{oxidation-start}} = 1000^{\circ}\text{C}$ with $\dot{m}_{\text{CO}_2} = 7 \text{ L/min}$ and ambient pressure.

and ambient pressure, during which CO₂ is injected into the reactor's cavity with flow rate \dot{m}_{CO_2} . During this phase, CO₂ reacts with the reduced ceria (Eq. 1.2) to form CO. The cycle ends when the reactor is fully oxidised, or when the oxidation-end temperature $T_{\text{oxidation-end}}$ is reached. Then, the cycle is repeated ($T_{\text{oxidation-start}} = T_{\text{oxidation-end}}$). The total cycle time is $\Delta t_{\text{cycle}} = \Delta t_{\text{reduction}} + \Delta t_{\text{cool-down}} + \Delta t_{\text{oxidation}}$.

2.2.2 Full-day Stable CO₂-splitting Cycles

Figure 2.7 shows a representative full day on-sun run with fully-automated 32 consecutive CO₂-splitting cycles as described in section 2.2.1. Plotted as function of time are the measured DNI (yellow line) over the day, mean RPC temperatures of both solar reactors (blue and red solid lines), and integrated

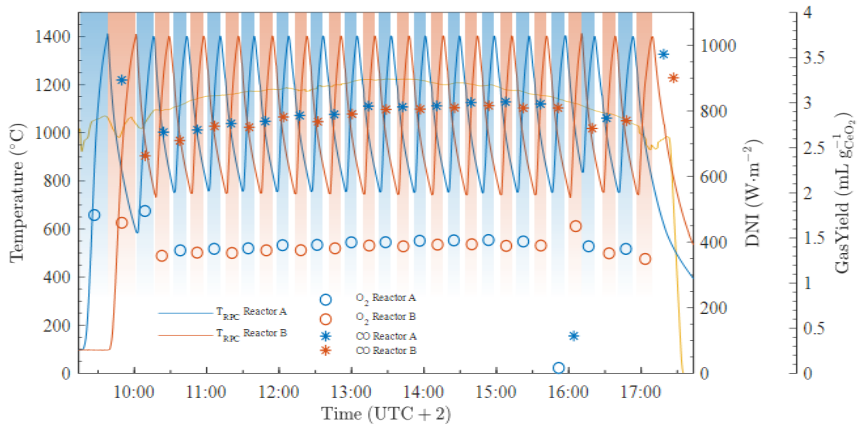


Figure 2.7: Full-day CO_2 -splitting Cycles. Measured RPC temperatures (red and blue), DNI (yellow), and specific gas yield per cycle of CO (circle) and O_2 (asterisks) over 32 consecutive CO_2 -splitting cycles of both solar reactors operated in alternate mode: while reactor A is performing the solar reduction step (eq. 1.1), reactor B is performing the oxidation step (eq. 1.2) and vice versa. Blue and red shaded areas indicate which reactor is on-sun performing the reduction step. Non-shaded areas indicate times where no reactor is performing the on-sun reduction, i.e. one reactor already finished the reduction step, while the other reactor is still performing the oxidation step. Reduction up to $T_{\text{reduction-end}} = 1400^\circ\text{C}$ with $\dot{m}_{\text{Ar}} = 1 \text{ L/min}$ and $p_{\text{reactor}} = 4\text{mbar}$. Oxidation started at $T_{\text{oxidation-start}} = 1000^\circ\text{C}$ with $\dot{m}_{\text{CO}_2} = 7 \text{ L/min}$ and at ambient pressure.

specific gas production per cycle (O₂: circles, CO: asterisks) for both solar reactors operated in alternate mode — one reactor is performing the solar reduction step (Eq. 1.1) while the other reactor is performing the oxidation step (Eq. 1.2). The ceria mass loading of each solar reactor was 3752 g and 3760 g, respectively. The solar power input and mean solar flux concentration through the aperture, measured by calorimetry between the cycles (white areas in Fig. 2.7), were up to 5.9 kW and 2360 suns, respectively. The DNI was increasing in the morning, was highest around solar noon, and decreased again in the afternoon. This had an effect on the reduction times (i.e. the reactor takes longer to reach $T_{\text{reduction-end}}$) which increased with lower DNI (i.e. slightly longer cycles in the morning and in the afternoon). For comparison, cycle 14 of the reactor represented with the blue curve was performed without pressure swing (i.e. ambient pressure during reduction) with the other settings unchanged. The much lower yield of that cycle clearly demonstrates the benefit of including the pressure swing.

The first two cycles of each reactor were longer, as all reactor components started heating up from ambient temperature. The O₂ release in the first cycle was higher as the reactors started fully oxidised. The slower heating of the reactors in the first cycles also leads to a more uniform temperature distribution within the RPCs. Which in turn leads to more ceria at higher temperatures when the reference temperature at the back of the RPC reaches $T_{\text{reduction-end}}$ and hence higher O₂ (and CO) yield of that cycle. The last two cycles show higher CO production as the reactors were cooled down further than before and the reactors were fully oxidised.

Averaged over the entire 32 cycles, the peak and total O₂ evolution was 0.29 ml g_{CeO₂}⁻¹ min⁻¹ and 1.44 ml g_{CeO₂}⁻¹, respectively, and the peak and total CO production was 0.31 ml g_{CeO₂}⁻¹ min⁻¹ and 2.89 ml g_{CeO₂}⁻¹, respectively. Accumulated over the 32 cycles the total production on that day was 168 L of O₂ and 338 L of CO. The CO/O₂ ratio was 2.01 showing that the mass balance for both reactors can be closed and confirming total selectivity for the conversion of CO₂ to CO, with net reaction $\text{CO}_2 = \text{CO} + 1/2\text{O}_2$. The solar-to-syngas energy efficiency $\eta_{\text{solar-to-syngas}}$ is defined as the ratio of the

heating value of the syngas produced to the sum of Q_{solar} and any other parasitic energy inputs such as those associated with vacuum pumping and inert gas consumption during the reduction step (detailed formulation see chapter 2.5). For this run, the average $\eta_{\text{solar-to-syngas}} = 3.8\%$ without any attempt undertaken to maximise efficiency or CO yield in this run. Apart from the first and last cycles of each reactor (as discussed), the results of gas yields per cycle show very constant, repeatable and regular cycling over the entire day, demonstrating the stability and robustness of the solar redox unit.

2.3 Cycles Targeting Syngas for Methanol and Fischer-Tropsch Synthesis

When producing syngas for downstream GTL synthesis, the composition of the syngas and there mainly the $\text{H}_2:\text{CO}$ ratio is key. The optimal composition depends on the type of synthesis performed, the catalyst, reaction conditions and production targets. Depending on the catalyst used in the GTL unit and the $\text{CO}:\text{CO}_2$ ratio in the syngas, the desired $\text{H}_2:\text{CO}_x = \text{H}_2:(\text{CO}+\text{CO}_2)$ molar ratio of syngas for methanol synthesis lies between 2 and 3, while the desired $\text{H}_2:\text{CO}$ molar ratio of syngas for FT synthesis is about 2. The syngas composition, especially the molar ratios $\text{H}_2:\text{CO}$ and $\text{CO}:\text{CO}_2$, can be controlled by adjusting the $\text{H}_2\text{O}:\text{CO}_2$ feed ratio to the solar reactor (e.g. Ref. [39] or chapter 3.2 of this thesis) and/or by performing separately the splitting of CO_2 and H_2O (e.g. Ref. [37, 40] or chapter 3.3 of this thesis) and/or by simply choosing appropriate start and end times of the syngas collection. In either case, the syngas purity and quality is suitable for GTL processing and can be tailored for methanol or FT synthesis, without the need of additional steps for correcting composition and/or separating undesired by-products.

Another key metric to consider for downstream GTL processing is the molar CO_2 conversion, as it determines how much unreacted CO_2 is leaving the reactor with the syngas. The general goal is to reduce the amount of CO_2 as it can negatively affect the GTL process. In case for downstream

methanol synthesis, CO_2 participates in the synthesis via inverse water gas shift reaction. It is therefore possible to run stable methanol synthesis with shares of CO_2 as long as the share of H_2 in the syngas is also adjusted to match the stoichiometric ratio for methanol synthesis. This concept was applied in the production of syngas for methanol synthesis in this thesis. The additional H_2 needed, could be minimised by lowering the CO_2 content of the syngas. So while it is possible to use the CO_2 in the methanol synthesis, this comes with an energy penalty for the additional H_2 production. The inverse water gas shift reaction also leads to water in the condensed methanol, which in an industrial plant would have to be separated afterwards. In the case of downstream FT synthesis, the CO_2 in the syngas does not participate in the main reaction. It has to be mentioned, that in industrial scale FT processes there is usually a small amount of CO_2 added to the syngas to control the resulting products and tailor them towards most desirable hydrocarbon chains. However, especially for FT synthesis, there needs to be more research done on how this larger share of CO_2 will affect the quality of products and how the GTL process could be adjusted to best deal with this share of CO_2 in the syngas.

2.3.1 Representative Co-splitting Cycle

A representative redox cycle for co-splitting of CO_2 and H_2O operated under a temperature/pressure-swing mode, consists of three phases: 1) An on-sun reduction phase of duration $\Delta t_{\text{reduction}}$, during which the solar reactor is exposed to concentrated sunlight at a mean solar radiative power $P_{\text{solar,mean}}$ through its aperture, and heated from the reduction-start temperature $T_{\text{reduction-start}}$ up to the desired reduction-end temperature $T_{\text{reduction-end}}$ of up to 1500°C , where the solar input is diverted by rotating the secondary reflector. During this phase, the reduction (Eq. 1.1) proceeds to release O_2 from CeO_2 assisted through an Ar sweep gas with flow rate \dot{m}_{Ar} and a decreased total pressure p_{reactor} by means of a vacuum pump. After the reduction phase the reactor is re-pressurized by injecting either Ar (when targeting syngas for methanol synthesis) or CO_2 (when targeting syngas

for FT synthesis) before the next phase: 2) An off-sun cool-down phase of duration $\Delta t_{\text{cool-down}}$ at ambient pressure without flow, during which the solar reactor is off-sun, and cools down to the oxidation-start temperature $T_{\text{oxidation-start}}$. In case the reactor was repressurised with CO_2 , part of the CO_2 in the reactor already reacts with the ceria to form CO (Eq. 1.2). 3) An off-sun oxidation phase of duration $\Delta t_{\text{oxidation}}$ at below $T_{\text{oxidation-start}}$ and ambient pressure, during which CO_2 and H_2O are co-injected into the reactor's cavity with flow rates \dot{m}_{CO_2} and $\dot{m}_{\text{H}_2\text{O}}$. During this phase, both CO_2 and H_2O react with the reduced ceria (Eq. 1.2 and 1.3) to form syngas. The cycle ends when the desired syngas composition (e.g. given by the cumulative $\text{H}_2:\text{CO}$ molar ratio) is reached, e.g. through a larger share of H_2 produced during oxidation, compensating for the CO already formed during the cool-down phase, or the oxidation-end temperature $T_{\text{oxidation-end}}$ is reached. Then, the cycle is repeated with $T_{\text{oxidation-start}} = T_{\text{oxidation-end}}$. The total cycle time is $\Delta t_{\text{cycle}} = \Delta t_{\text{reduction}} + \Delta t_{\text{cool-down}} + \Delta t_{\text{oxidation}}$.

2.3.2 Cycle Targeting Syngas for Methanol Synthesis

Figure 2.8 shows an exemplary redox cycle for co-splitting H_2O and CO_2 and producing solar syngas with compositions suitable for methanol synthesis. Figure 2.8a shows the temporal variation of the nominal cavity temperature, total pressure, and outlet gas flow rates during a single redox cycle. The solar radiative power input is maintained relatively constant at $P_{\text{solar}} = 5.1 \text{ kW}_{\text{thermal}}$. Note the high flowrates of H_2 compared to the flow rates of CO as also unreacted CO_2 is taken into account to determine if the syngas is suitable for methanol synthesis. Figure 2.8b shows the variation of the cumulative species concentrations and yields of solar syngas collected during the oxidation step. Time 0 denotes the start of the oxidation when the nominal reactor temperature reaches $T_{\text{oxidation-start}}$.

When generating syngas for methanol synthesis in Fig. 2.8b, the full oxidation cycle over 20 min yields 18.5 L of syngas with composition 40.7% H_2 , 4.3% CO, 22.4% CO_2 and 32.6% Ar. The resulting molar ratio $\text{H}_2:\text{CO}_x$

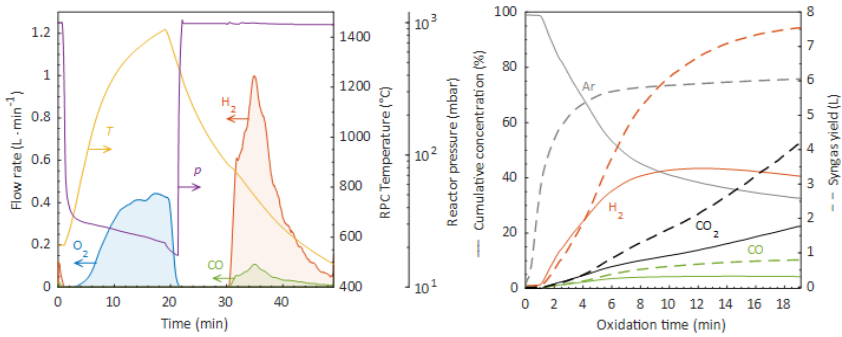


Figure 2.8: Representative solar redox cycle producing syngas with composition suitable for methanol synthesis. a) Temporal variation of the nominal cavity temperature, total pressure, and outlet gas flow rates during a single redox cycle. b) Temporal variation of the cumulative species concentration and yield of solar syngas collected during the oxidation step. Operation conditions — During the reduction step: $Q_{\text{solar}} = 5.1 \text{ kW}$, $\dot{m}_{\text{Ar}} = 0.5 \text{ L/min}$, $T_{\text{reduction-end}} = 1450^{\circ}\text{C}$, $p_{\text{reactor}} \leq 25 \text{ mbar}$. During the oxidation step: $Q_{\text{solar}} = 0 \text{ kW}$, $\dot{m}_{\text{CO}_2} = 0.4 \text{ L/min}$, $\dot{m}_{\text{H}_2\text{O}} = 9.8 \text{ g/min}$, $T_{\text{oxidation-start}} = 900^{\circ}\text{C}$, $p_{\text{reactor}} = 1 \text{ bar}$.

is 1.52, which is not optimal for methanol synthesis. Besides, the CO_2 conversion — integrated over the full oxidation period — is only 16.1%. Apart from selecting $T_{\text{oxidation-start}}$, \dot{m}_{CO_2} and $\dot{m}_{\text{H}_2\text{O}}$, the composition of the syngas can be adjusted by choosing adequate start and end times of the syngas collection. For example, immediately after the start of the oxidation step, the syngas contains undesired high content of Ar. As example, the first two minutes of oxidation already yield 4.9 L of syngas, but with the composition of 10.2% H_2 , 0.9% CO, 1.6% CO_2 and 87.3% Ar (i.e. containing predominatly Ar). This part of the syngas containing predominatly Ar should be discarded and the syngas quality can be improved by simply delaying the start of the syngas collection. On the other hand, the end of the syngas collection can be determined once the desired molar ratio $\text{H}_2:\text{CO}_x$ of the collected syngas is achieved. As example, the end of oxidation from minute 10 onwards contains another 4.2 L of syngas but with the composition of 33.6% H_2 , 64.5% CO, 57.7% CO_2 and 4.2% Ar (i.e. containing predominatly unreacted CO_2) would tip the $\text{H}_2:\text{CO}_x$ ratio too much towards the CO_x side and hence this part of the syngas should be discarded.

Collecting only the syngas between minutes 2 and 10 instead (Fig. 2.8b) would yield only 9.4 L of syngas, i.e. only about half the amount compared to total oxidation, but with a more favorable composition of 59.9% H_2 , 6.0% CO, 17.2% CO_2 and 16.9% Ar. The resulting molar ratio $\text{H}_2:\text{CO}_x$ would be 2.58, and thus suitable for methanol synthesis. Evidently, there is a trade-off between syngas quality and syngas quantity. The CO_2 conversion — integrated over minutes 2 to 10 — would now be 25.7%. Furthermore, the Ar content would be cut in half, reducing the energy penalty of carrying an inert gas downstream. Nevertheless, a scale-up of the process would require either Ar separation and recycling or ways to avoid the use of inert gas for re-pressurizing during the switch from the reduction step to the oxidation step. Replacing Ar with CO_2 is not an option for cycles targeting syngas suitable for methanol synthesis, as the additional amount of CO_2 (and CO produced from it) would lower the $\text{H}_2:\text{CO}_x$ molar ratio too much, so the syngas would not be suitable for methanol synthesis anymore. In terms

of energy efficiency, $\eta_{\text{solar-to-syngas}}$ is affected in both directions because, although the amount of syngas is reduced, the duration of both redox steps can be shortened and Q_{solar} , Q_{pump} and Q_{inert} are therefore smaller (see Eqs. 2.4 - 2.9).

2.3.3 Cycle Targeting Syngas for Fischer-Tropsch Synthesis

Figure 2.9 shows an exemplary redox cycle for co-splitting H_2O and CO_2 and producing solar syngas with compositions suitable for FT synthesis. Figure 2.9a shows the temporal variation of the nominal cavity temperature, total pressure, and outlet gas flow rates during a single redox cycle. The solar radiative power input is maintained relatively constant at $P_{\text{solar}} = 4.1 \text{ kW}_{\text{thermal}}$. Note the much larger CO flow rate compared to Fig. 2.8 despite the lower \dot{m}_{CO_2} during oxidation. This is because the reactor could now be repressurised with CO_2 instead of Ar. Also note the difference in power levels compared to Fig. 2.8, leading to the much longer reduction time of over 30 minutes compared to just under 20 minutes in Fig. 2.8. Figure 2.9b shows the variation of the cumulative species concentrations and yields of solar syngas collected during the oxidation step. Time 0 denotes the start of the oxidation when the nominal reactor temperature reaches $T_{\text{oxidation-start}}$.

When generating syngas for FT synthesis in Fig. 2.9b, the full oxidation after 25 min yields 15.6 L of syngas with composition 31.0% H_2 , 11.4% CO and 57.6% CO_2 . Note the absence of Ar in the syngas for FT synthesis because CO_2 was used instead to re-pressurize the solar reactor after the reduction step. The molar ratio $\text{H}_2:\text{CO} = 2.72$, which is not optimal for FT synthesis, and the CO_2 conversion — integrated over the full oxidation period — is only 16.5%. However, the end of the syngas collection can be determined once the desired molar ratio $\text{H}_2:\text{CO}$ of the collected syngas is achieved.

Collecting the syngas between minutes 0 and 4.25 of the oxidation cycle (Fig. 2.9b) would yield only 7.52 L of syngas, i.e. only about half the amount compared to the full oxidation, but with a more favorable composition of

43.1% H₂, 21.5% CO and 35.4% CO₂. The resulting molar ratio would be exactly H₂:CO = 2, and thus suitable for FT synthesis. The CO₂ conversion — integrated over minutes 0 to 4.25 — would now be 37.9%. For comparison, the end of oxidation from minute 4.25 onwards contains another 8.05 L of syngas but with the composition of 19.6% H₂, 1.9% CO and 78.5% CO₂ (i.e. containing predominately unreacted CO₂). This syngas would dilute the total syngas with more undesired CO₂ and also tip the H₂:CO ratio too much towards the H₂ side and hence this part of the syngas should be discarded.

Evidently, there is a trade-off between syngas quality and syngas quantity. Note that the operational conditions during the oxidation step (\dot{m}_{CO_2} , $\dot{m}_{\text{H}_2\text{O}}$ and $T_{\text{oxidation-start}}$) are different for the run targeting syngas for methanol synthesis and the one targeting syngas for FT synthesis. A more detailed study how operational parameters affect the syngas yield and other performance values can be found in chapter 3.2. Chapter 3.2 also shows results of cycles where a higher amount of the total oxidation potential is used to produce syngas of the desired composition. Note that for production, the cycle would not be performed to the end of oxidation but ended prematurely by the end of syngas collection to avoid additional passive cooling of the cavity and enable shorter cycle durations.

In both redox cycles for 2.8 and 2.9, the oxygen mass balance can be closed within the error bars of the measurement devices (electronic mass flow controllers and the electrochemical and IR gas analysis), confirming total selectivity for the conversion of H₂O to H₂ and of CO₂ to CO, with net reactions $\text{H}_2\text{O} = \text{H}_2 + 1/2 \text{O}_2$ and $\text{CO}_2 = \text{CO} + 1/2 \text{O}_2$. Total selectivity was obtained in all cycles performed with the solar reactor, i.e. only the reduction (Eq. 1.1) and oxidation (Eq. 1.2 and 1.3) reactions occur.

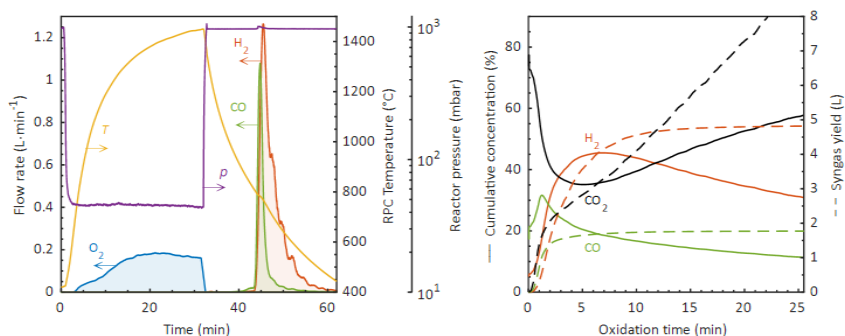


Figure 2.9: Representative solar redox cycle producing syngas with composition suitable for FT synthesis. a) Temporal variation of the nominal cavity temperature, total pressure, and outlet gas flow rates during a single redox cycle. b) Temporal variation of the cumulative species concentration and yield of solar syngas collected during the oxidation step. Operation conditions — During the reduction step: $Q_{\text{solar}} = 4.1 \text{ kW}$, $\dot{m}_{\text{Ar}} = 0.5 \text{ L/min}$, $T_{\text{reduction-end}} = 1450^{\circ}\text{C}$, $p_{\text{reactor}} \leq 50 \text{ mbar}$. During the oxidation step: $Q_{\text{solar}} = 0 \text{ kW}$, $\dot{m}_{\text{CO}_2} = 0.2 \text{ L/min}$, $\dot{m}_{\text{H}_2\text{O}} = 9.8 \text{ g/min}$, $T_{\text{oxidation-start}} = 800^{\circ}\text{C}$, $p_{\text{reactor}} = 1 \text{ bar}$.

2.4 Producing Syngas for Methanol Synthesis

2.4.1 Full-day Syngas Production for Methanol Synthesis

Figure 2.10 shows a representative 7-hour day run with 17 consecutive redox cycles for co-splitting H_2O and CO_2 , targeting syngas suitable for methanol synthesis. Depicted are the reactor temperatures (blue and red solid lines) and pressures (dashed lines), DNI (yellow line) and accumulated syngas over the time (black line) of day, as well as the syngas composition per cycle (diamond shapes for H_2 , circles for CO_2 and asterisks for CO). Analogous to Fig. 2.7 the cycles are shortest around noon and are getting longer towards the evening with decreasing DNI (Δt_{cycle} increasing because of increasing $\Delta t_{\text{reduction}}$). The pressure curves show that the achieved vacuum pressure in the reactor is decreasing with longer $\Delta t_{\text{reduction}}$, due to the continuous evaporation of H_2O left in the tubing downstream of the reactor. Note the increase of reactor pressure during reduction over the day due to water accumulation in the system. The results for accumulated syngas and composition show very constant cycling over the entire day, again demonstrating the stability of the solar redox system.

Over the entire day the yield was 96.2 L (standard liters, including all species H_2 , CO , CO_2 , and Ar) of syngas with composition 59.5% H_2 , 4.6% CO , 17.5% CO_2 , and 18.4% Ar . The daily mass specific yield of syngas was 12.81 L/kg of ceria (3.752 kg ceria per reactor) and its cumulative molar ratio $\text{H}_2:\text{CO}_x$ was 2.7. The cumulative CO_2 -to- CO molar conversion was 15.1%. This conversion can be further increased by reducing the CO_2 mass flow rate but at the expense of producing less syngas. The presence of unreacted CO_2 in the syngas obviously affects its molar ratio $\text{H}_2:\text{CO}_x$, which is critical for methanol synthesis but less relevant for FT synthesis. It is worth pointing out that the cumulative molar ratio $\text{H}_2:\text{CO}_x$ of 2.7 over the entire day of Fig. 2.10 is close to the optimal stoichiometric ratio for producing methanol with the respective CO_2 -to- CO molar conversion 2.8. This took careful adjustments of \dot{m}_{CO_2} , $\dot{m}_{\text{H}_2\text{O}}$ and $T_{\text{oxidation-start}}$ over

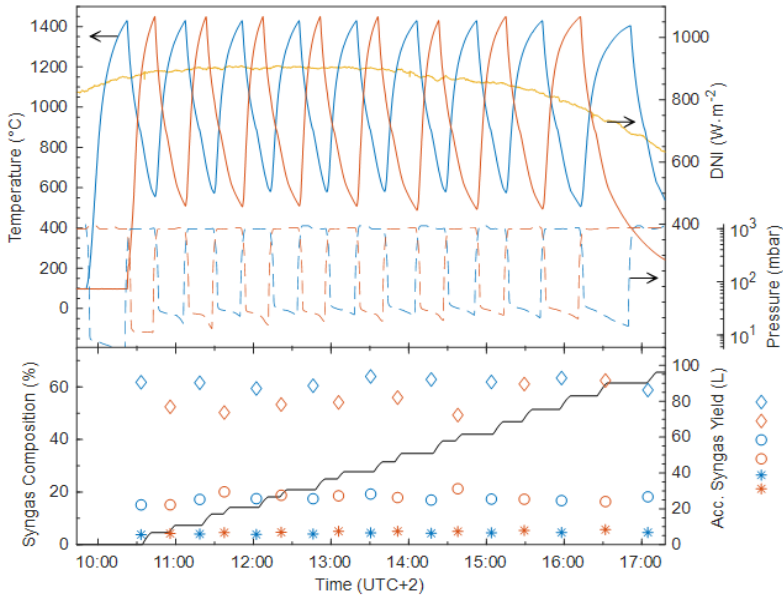


Figure 2.10: Representative day run of the solar redox unit for co-splitting H_2O and CO_2 . Temporal variations of the DNI (yellow), temperature (blue and red solid lines), pressure (blue and red dashed lines), syngas composition (diamond shapes for H_2 , circles for CO_2 and asterisks for CO), and cumulative syngas yield (black) of the two adjacent solar reactors A and B (blue and red) performing the thermochemical redox cycle simultaneously. The concentrated solar radiative input is alternated between the solar reactors A and B: while one reactor is solar irradiated to effect the reduction step (Eq. 1.1), H_2O and CO_2 are injected in the second reactor to effect the oxidation step (Eqs.1.2 and 1.3). Reduction: $\dot{m}_{\text{Ar}} = 0.5 \text{ L/min}$. Oxidation: $\dot{m}_{\text{CO}_2} = 0.3 \text{ L/min}$, $\dot{m}_{\text{H}_2\text{O}} = 9.8 \text{ g/min}$.

multiple days of experiments leading to the presented production campaign in this chapter. Note that, in contrast to the runs of Figs. 2.8 and 2.9, the oxidation steps in the consecutive cycles of Fig. 2.10 were not executed until completion but they were terminated prematurely at the end of syngas collection to avoid additional passive cooling of the cavity and enable shorter cycle durations. Average $\eta_{\text{solar-to-syngas}}$ of Fig. 2.10 was 1.9. This is much lower compared to the previously presented CO₂-splitting cycles of Fig 2.7, mainly as in this case the reactors were not fully oxidised and co-splitting generally leads to lower $\eta_{\text{solar-to-syngas}}$ compared to CO₂-splitting only.

The molar ratios H₂O:CO₂ of reactants fed to the solar redox unit for the run in Fig. 2.10 (but also for the runs of Fig. 2.8, Fig. 2.9 and any other co-splitting cycles) were significantly higher than the stoichiometric ones, indicating large amounts of excess H₂O fed into the solar reactor. Because CO₂ dissociation proceeds more readily than that of H₂O at equal conditions [39], a large excess of H₂O over CO₂ had to be introduced into the solar reactor to obtain the desired syngas compositions. Additionally, some H₂O condenses out in the system even before getting in contact with the ceria cavity, again increasing the needed excess H₂O. This condensation in the water cooled inlet cone between window and aperture (see Fig. 2.3) could be avoided by switching from water to oil cooling at temperatures above 100°C. The excess water introduces significant energy penalties associated with steam generation and heating unreacted species.

The experimental run of Fig. 2.10 was part of a bigger methanol production campaign shown below. For the representative 7-hour day run of Fig. 2.10, the relative amount of pure methanol produced was 3.2 cl.

2.4.2 Long-term Production Campaign for Methanol Synthesis

This section presents a long-term production campaign performing 152 consecutive redox cycles over 18 measurement days targeting syngas suitable

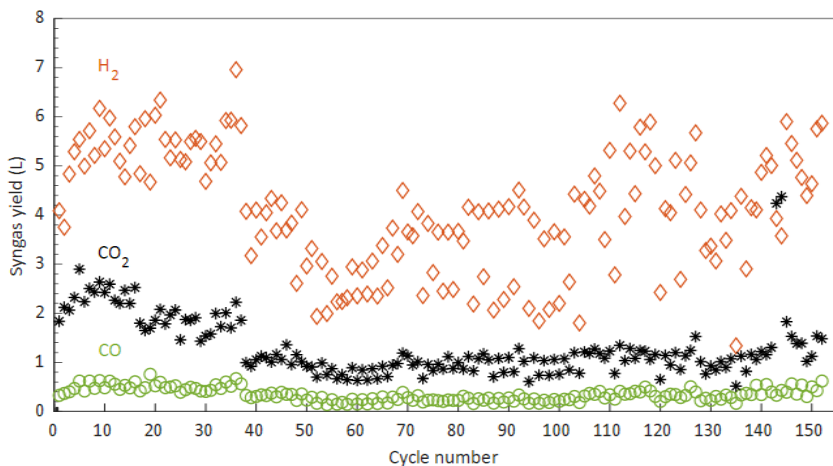


Figure 2.11: Syngas yield (H_2 in orange, CO in green, CO_2 in black) for each of the 152 consecutive solar redox cycles for producing syngas suitable for methanol synthesis.

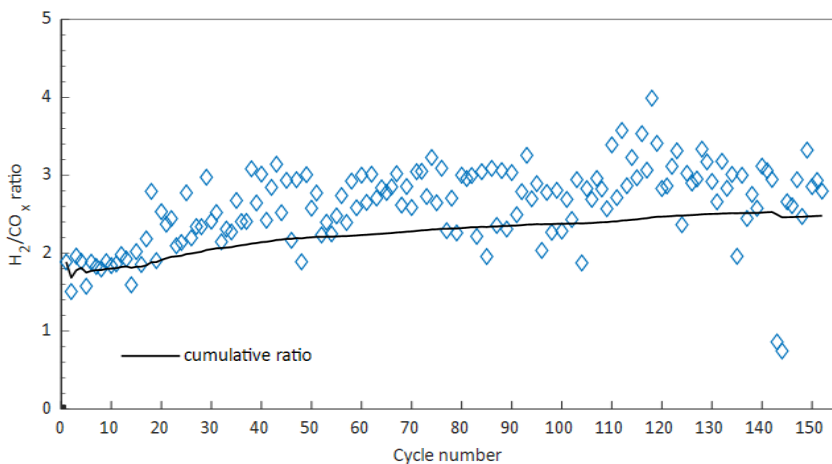


Figure 2.12: Cyclic variation (blue data points) and cumulative $H_2:CO_x$ molar ratio (black curve) for the 152 consecutive redox cycles of Fig. 2.11

for methanol synthesis.

Figure 2.11 shows the syngas composition and yield for each of the 152 consecutive solar redox cycles. In contrast to the day run of Fig. 2.10, which was performed on a clear day with constant DNI and yielded steady syngas composition from cycle to cycle, this long-term run was performed over 18 days and yielded significant variations in the syngas composition from cycle to cycle, primarily due to the unstable DNI, which in turn affected the solar radiative power input, the heating rates and temperature distributions, and the reduction and oxidation rates and extents. As the run progressed, the H_2O and CO_2 mass flow rates were adjusted to ensure syngas collection with a cumulative molar ratio $\text{H}_2:\text{CO}_x$ in the range 2-3, suitable for methanol synthesis. The reactants' flow rates during the oxidation step were 0.4 L/min CO_2 and 10 g/min H_2O for cycles 1 to 37, and 0.3 L/min CO_2 and 10 g/min H_2O for cycles 38 to 152. During the first 17 cycles, a molar ratio $\text{H}_2:\text{CO}_x = 2$ was targeted. From cycle 18 onwards, a cumulative molar ratio $\text{H}_2:\text{CO}_2 = 2.5$ over the entire 152 cycles was targeted.

Figure 2.12 shows the cyclic variation and cumulative molar ratio $\text{H}_2:\text{CO}_x$ for the 152 redox cycles of Extended Data Fig. 4. The total yield was 1069.7 L of syngas with composition 58.4% H_2 , 5% CO , 18.6% CO_2 and 18% Ar (after condensation of unreacted water). Thus, the cumulative molar ratio obtained was $\text{H}_2:\text{CO}_2 = 2.48$, hence almost exactly reaching the targeted ratio of 2.5.

The collected syngas from this measurement campaign was further processed to methanol in the GTL unit, hence completing the demonstration of the entire thermochemical process chain from ambient air and sunlight to liquid fuels.

2.5 Energy Efficiency Analysis

The overall energy conversion efficiency of the solar fuel system, i.e. the system efficiency η_{system} , is defined as the ratio of the heating value of the

liquid fuel produced to the total energy input to the system, which in turn results from multiplying the energy efficiencies of each of the three units of the process chain:

$$\eta_{\text{system}} = \eta_{\text{DAC}} \cdot \eta_{\text{solar redox unit}} \cdot \eta_{\text{GTL}} \quad (2.2)$$

where $\eta_{\text{solar redox unit}}$ results from multiplying the optical efficiency with that of the solar reactor:

$$\eta_{\text{solar redox unit}} = \eta_{\text{optical}} \cdot \eta_{\text{solar-to-syngas}} \quad (2.3)$$

The optical efficiency η_{optical} is defined as the ratio of the solar radiative energy input to the solar reactor, Q_{solar} , to the DNI incident on the solar primary concentrator. Q_{solar} can be measured through calorimetry or solar flux measurements, see section 2.1.2 and Ref. [79]. The area of the primary concentrator also includes the areas shaded by the secondary reflector and its support structure. The solar-to-syngas energy efficiency $\eta_{\text{solar-to-syngas}}$ is defined as the ratio of the heating value of the syngas produced to the sum of Q_{solar} and any other parasitic energy inputs such as those associated with vacuum pumping and inert gas consumption during the reduction step:

$$\eta_{\text{solar-to-syngas}} = \frac{Q_{\text{fuel}}}{Q_{\text{input}}} = \frac{Q_{\text{fuel}}}{Q_{\text{solar}} + Q_{\text{pump}} + Q_{\text{inert}}} \quad (2.4)$$

Q_{fuel} is the heating value of the collected fuel (CO and H₂) produced over a cycle, given by:

$$Q_{\text{fuel}} = \sum_{\text{fuel:H}_2, \text{CO}} (\Delta H_{\text{fuel}} \int r_{\text{fuel}} dt) \quad (2.5)$$

where ΔH_{fuel} is the molar enthalpy change of fuel oxidation (e.g. $\Delta H_{\text{CO}} = 283$ kJ/mol, $\Delta H_{\text{H}_2} = 286$ kJ/mol) and $\int r_{\text{fuel}} dt$ is the measured molar rate of the fuel produced integrated over the duration of the oxidation step. Q_{solar} is the total solar energy input integrated over the duration of the reduction step:

$$Q_{\text{solar}} = \int P_{\text{solar}} dt \quad (2.6)$$

where P_{solar} is the measured solar radiative power input through the solar reactor's aperture (measured by the water calorimeter with same aperture size), accounting for the total transmittance of the quartz window (measured value 0.932) [83]. Q_{pump} and Q_{inert} are the thermal energy penalties associated with vacuum pumping and inert gas consumption during the reduction step. All work terms are converted to an equivalent heat by dividing by a heat-to-work efficiency $\eta_{\text{heat-to-work}}$ (assumed 0.4). In this way, the entire thermochemical process chain is driven using solar heat alone. Q_{pump} is calculated as the thermodynamic minimum pumping work divided by the product of two efficiencies, namely the heat-to-work efficiency $\eta_{\text{heat-to-work}}$ and the vacuum pump efficiency η_{pump} , according to:

$$Q_{\text{pump}} = \frac{1}{\eta_{\text{heat-to-work}} \cdot \eta_{\text{pump}}} \int \dot{n}(t) \cdot R \cdot T \cdot \ln\left(\frac{p_{\text{atmospheric}}}{p_{\text{cavity}}(t)}\right) dt \quad (2.7)$$

where $\dot{n}(t)$ is the sum of the measured molar flow rates of Ar injected and O_2 released by ceria during the reduction step, p_{cavity} is the measured total pressure inside the cavity and $p_{\text{atmospheric}}$ is the atmospheric pressure. The pump efficiency for a multi-stage industrial arrangement[72] is given by:

$$\eta_{\text{pump}} = 0.07 \cdot \log\left(\frac{p_{\text{cavity}}}{p_{\text{atmospheric}}}\right) + 0.4 \quad (2.8)$$

Note that $\eta_{\text{solar-to-syngas}}$ is weakly dependent on η_{pump} because $Q_{\text{solar}} \gg Q_{\text{pump}}$ at the moderate vacuum pressure levels applied during reduction in the range 10-1000 mbar. The thermal energy required for inert gas separation is given by:

$$Q_{\text{inert}} = \frac{1}{\eta_{\text{heat-to-work}}} E_{\text{inert}} \int r_{\text{inert}} dt \quad (2.9)$$

where r_{inert} is the measured Ar flow rate and E_{inert} is the work required for inert gas separation, assumed 20 kJ per mole [84]. Because of the relatively low mass flow rate of Ar, Q_{inert} is typically less than 5% of Q_{solar} , but even this penalty could be eliminated by replacing Ar with ambient air during the reduction step as proven experimentally [40]. Furthermore, when targeting syngas for FT synthesis, CO_2 is injected after the reduction step

for re-pressurizing the reactor, hence avoiding the use of inert gas for that step.

Based on the measured performance of the solar redox unit and the experimental results presented in this chapter, $\eta_{\text{solar-to-syngas}} = 1.9 - 3.8\%$ with no attempt to optimise the units for maximum η_{system} . To date, the highest experimentally obtained $\eta_{\text{solar-to-syngas}}$ was 5.25% with a labscale 4-kW_{thermal} solar reactor tested in a solar simulator [40] and 5.6% with a 50-kW_{thermal} solar reactor mounted on a solar tower [20], both solar reactors were of the same type as the one presented in this thesis and were performing a CO₂-splitting redox cycle without any heat recovery.

The following attempt at calculating η_{system} of the presented fuel system is based on assumptions regarding the DAC and GTL unit. As the DAC unit is driven by heat, the heat source has a major influence on η_{DAC} . With thermal management, the DAC unit could predominantly be driven by waste heat at below 100°C, available for example from the solar redox unit (e.g. from the reactors or optical spillage). Note that this heat integration is not implemented in the current system, mainly due to scaling issues with transporting heat from the reactors to the DAC unit (significant heat losses in piping at that scale) and the capacity mismatch between the solar redox unit and the DAC unit. The GTL unit could be operated auto-thermally, since the synthesis reaction is exothermic. Of course electricity would still be needed to operate the pumps in the DAC unit (desorption step at below 0.1 bar), the solar redox unit (reduction step at below 0.05 bar), and GTL unit (synthesis step at above 20 bar), as well as to run the controls, valves and smaller auxiliary systems. However, the energy penalties of the DAC unit and the GTL unit remain comparably small compared to the one of the solar redox unit, and thus $\eta_{\text{solar redox unit}}$ is the dominating term in the calculation of η_{system} (see Eq. 2.2).

Based on the measured performance of the solar redox unit described in this chapter and accounting for the energy penalties associated with vacuum pumping and inert gas separation, $\eta_{\text{optical}} = 59.6\%$ [79] and $\eta_{\text{solar-to-syngas}}$

= 1.9 - 3.8% as discussed above. This results in $\eta_{\text{solar redox unit}} = 1.1 - 2.3\%$. Assuming $\eta_{\text{DAC}} = 0.90$ (accounting for the energy penalty of vacuum pumping, assumed isothermal with 0.7 efficiency, but assuming waste heat thermal management) and $\eta_{\text{GTL}} = 0.75$ (using the measured syngas-to-methanol conversion of 85% and accounting for the energy penalty of gas compression, but assuming auto-thermal synthesis), the efficiency of the present non-optimized solar fuel system described in this chapter can be estimated as $\eta_{\text{system}} \approx 0.8 - 1.5\%$.

To increase η_{system} there are multiple options. For example, optimising the optical system by minimising surface and tracking errors can increase η_{optical} to 82% [85]. This change alone would already increase η_{system} to 1.1 - 2.1%. Additionally taking the highest so far demonstrated $\eta_{\text{solar-to-syngas}} = 5.6\%$ [20] would yield $\eta_{\text{system}} = 3.1\%$.

The low value obtained for $\eta_{\text{solar-to-syngas}}$ is mainly due to the sensible heat rejected during the temperature-swing cycling (no heat recovery), which accounted for more than 60% of Q_{solar} . Could this fraction be partially or mostly recovered, and combined with other improvements for example on the RPC structure [86, 87] this could raise $\eta_{\text{solar-to-syngas}}$ to over 20% [63, 56, 88]. Using the same numbers for the increased optical efficiency as before, this would boost η_{system} to over 11.1%. Assuming the entire solar redox unit performing at 20%, η_{system} has the potential of exceeding 13%.

However, it has to be mentioned that heat recuperation at that reactor scale is extremely challenging due to the high losses in tubing etc. at that scale (due to large surface to volume ratio) and should best be investigated on scaled up versions of the fuel system. The analysis above also shows that heat recuperation in the solar redox unit and thermal management to enable thermo-neutral operation of the DAC and GTL units is absolutely essential for a potential up scaled industrial implementation.

Putting this efficiency in perspective to other pathways to produce solar hydrocarbon fuels, shows that the technology has the potential to possibly surpass for example the PV-electrolysis pathway (solar electricity production using PV combined with water electrolysis) with efficiency from solar energy

to liquid fuels estimated in different studies between 8.2-12.9% [18, 89, 90]. This is mainly because the PV-electrolysis pathway requires the production of substantial excess H_2 by water electrolysis using solar electricity, which is subsequently consumed via the highly endothermic RWGS reaction to obtain syngas suitable for the GTL step. In contrast, the presented thermochemical pathway bypasses the solar electricity generation, the electrolysis, and the RWGS steps, and directly produces solar syngas of desired composition in a single step. Comparing technologies like that however, has to be done very critically and is subject to a lot of uncertainties and assumptions, especially given the very different maturity levels of the technologies. With these uncertainties in mind, it might make best sense to further develop both technologies before finally ruling out one over the other.

2.6 Summary and Conclusions

The chapter described the developed and installed process chain to solar fuels from ambient air and sunlight. The system serially integrates three thermochemical process units: 1) The DAC unit, capturing CO_2 and H_2O from ambient air via adsorption/desorption cycles based on temperature and pressure swing. 2) The solar redox unit, concentrating sunlight with a modular parabolic dish system to heat up two solar reactors for performing in parallel the ceria redox cycles to produce syngas. And 3) the GTL unit to finally transform the syngas to methanol or hydrocarbon fuels. The redox cycles for splitting CO_2 or for co-splitting CO_2 and H_2O have been introduced and full day cyclic runs presented. The continuous on-sun cycling under real field conditions over the entire day demonstrates the robustness and stability of the solar redox unit.

Perhaps the most critical aspect of integration is the suitability of the gas streams exchanged between the units, namely the quality and purity of CO_2 and H_2O exiting the DAC unit and fed to the solar redox unit, and the quality and purity of the syngas exiting the solar redox unit and fed to

the GTL unit. The solar fuel system fulfills the suitability criterion without the need for additional refinement steps, such as the energy-intensive RWGS step, and thereby reaffirmed the potential for high η_{system} (Eq. 2.2).

Integrating the three units and producing methanol, demonstrates the technical viability of the thermochemical process chain for converting sunlight and ambient air to drop-in fuels and advance the technological readiness and its industrial implementation.

PARAMETRIC STUDY OF THE SOLAR REACTOR OPERATION ¹

The experimental parametric study in this chapter shows how key performance indicators such as the specific fuel yield, molar conversion, and solar-to-fuel energy efficiency vary as a function of the operational parameters. In particular, the CO₂ molar conversion and the H₂:CO molar ratio of the syngas are crucial and set the quality criterion for collecting the gas products. The syngas composition can be tailored for FT-synthesis by selecting adequate operational conditions, eliminating the need for additional downstream refining of the syngas, e.g. via the energy-intensive reverse water-gas shift reaction.

Note that the study in this chapter considers only the operational parameters of the solar reactor. Performance can be further improved by physical

¹Parts of this chapter are in press as: Schäppi, R. *et. al.*, Solar Thermochemical Production of Syngas from H₂O and CO₂ — Experimental Parametric Study, Control, and Automation. *Industrial & Engineering Chemistry Research*, (2024).

modifications in the reactor design or the system setup, e.g. improved porous structures for volumetric absorption [86, 87] and integration of heat recovery of the heat rejected during the temperature swings between the redox cycles [91], but these are beyond the scope of this thesis (see chapter 6.2.1).

The operational parameters studied in this chapter are: p_{reactor} , $T_{\text{reduction-end}}$, $T_{\text{oxidation-start}}$, \dot{m}_{CO_2} , $\dot{m}_{\text{H}_2\text{O}}$, \dot{m}_{Ar} , and the syngas quality criterion. $P_{\text{solar,mean}}$ can in principle be controlled with a diaphragm-shutter but it was not applied as an operational parameter; the diaphragm-shutter was left open and $P_{\text{solar,mean}}$ resulted from the actual measured DNI.

The performance indicators studied in this chapter are:

i) The cumulative CO_2 molar conversion X_{CO_2} , defined as the extent of CO_2 converted to CO during oxidation:

$$X_{\text{CO}_2} = \frac{V_{\text{CO}}}{V_{\text{CO}} + V_{\text{CO}_2}} \quad (3.1)$$

where V_{CO} and V_{CO_2} denote the cumulative volumes of CO and CO_2 exiting the reactor, respectively. The cumulative H_2O molar conversion $X_{\text{H}_2\text{O}}$ is defined analogously. Note that the instantaneous conversions \dot{X}_{CO_2} and $\dot{X}_{\text{H}_2\text{O}}$ can be calculated using the ratio of the reactor outlet flow rates, but such values can be misleading as they do not represent the mean performance.

ii) The syngas yield V_{syngas} per cycle in standard liters L (0°C and 1 atm):

$$V_{\text{syngas}} = V_{\text{CO}} + V_{\text{H}_2} \quad (3.2)$$

iii) The $\text{H}_2:\text{CO}$ molar ratio $R_{\text{H}_2:\text{CO}}$ in syngas:

$$R_{\text{H}_2:\text{CO}} = \frac{V_{\text{H}_2}}{V_{\text{CO}}} \quad (3.3)$$

which serves as a quality measure as well as a target value and criterion for collecting the product gases. For FT synthesis, the optimal value for $R_{\text{H}_2:\text{CO}}$ is around 2.

iv) The solar-to-syngas energy efficiency $\eta_{\text{solar-to-syngas}}$, defined as the ratio of the heating value of the syngas produced to the sum of the solar

radiative power through the aperture (after the window) input and any other parasitic energy inputs such as those associated with vacuum pumping and inert gas consumption. The detailed formulations for the calculation of $\eta_{\text{solar-to-syngas}}$ can be found in chapter 2.5.

3.1 Reduction Parameters

Figure 3.1 shows the reduction step of the cycle with varying parameters p_{reactor} , \dot{m}_{Ar} and $T_{\text{reduction-end}}$ for various P_{solar} while keeping all other settings constant. $\eta_{\text{solar-to-syngas}}$ can either be calculated using the measured CO produced during oxidation or, alternatively, could be calculated based on the O₂ released during reduction (assuming full oxidation) because of the closed mass balance: $\text{CO}_2 = \text{CO} = \frac{1}{2}\text{O}_2$, i.e. 1 mol O₂ released leads to 2 moles CO produced. The CO₂ flow rates were chosen to assure full oxidation at every cycle. The trends shown in Fig. 3.1 hold true for all oxidation conditions leading to full oxidation. Note that \dot{m}_{Ar} and p_{reactor} are coupled, i.e. an increase in \dot{m}_{Ar} leads to higher p_{reactor} because of the fixed operation of the vacuum pump which is connected to the reactor through 8 m length, 45 mm diameter tube (see Fig. 2.1). The cumulative O₂ released V_{O_2} increases with \dot{m}_{Ar} because of the lower oxygen partial pressure due to the combined effect of vacuum pumping and inert gas flow [43]. \dot{m}_{Ar} also has a cooling effect leading to a longer heat up time $\Delta t_{\text{reduction}}$, which in turn results in a more uniform temperature distribution within the RPC and thus more ceria mass reacting when $T_{\text{reduction-end}}$ is reached, hence additionally contributing to higher V_{O_2} . As expected from thermodynamics [43], higher $T_{\text{reduction-end}}$ leads to higher V_{O_2} . $\eta_{\text{solar-to-syngas}}$ also increases for $T_{\text{reduction-end}} > 1400^\circ\text{C}$. Note, that while the results indicate trends of how to increase $\eta_{\text{solar-to-syngas}}$, the maximum potential $\eta_{\text{solar-to-syngas}}$ is likely much higher and could be found with further optimization. For lower $T_{\text{reduction-end}}$ the temperature dependence of $\eta_{\text{solar-to-syngas}}$ is influenced primarily by the lower Q_{solar} based on the shorter $\Delta t_{\text{reduction}}$. Lower P_{solar}

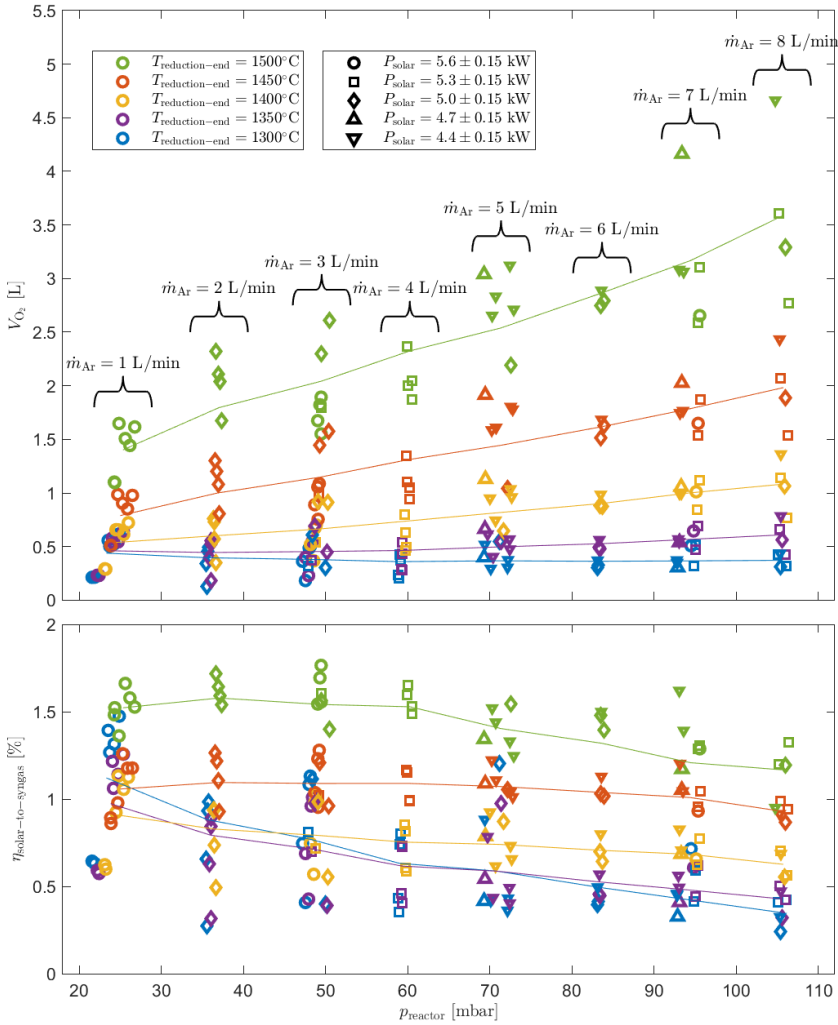


Figure 3.1: Parametric study of reduction parameters: Colours indicate the values obtained by integrating until $T_{\text{reduction-end}} = 1300, 1350, 1400, 1450,$ and 1500°C , while trend lines for each $T_{\text{reduction-end}}$ obtained by data averaged over all solar radiative power levels; shapes indicate the average $P_{\text{solar}} = 4.4, 4.7, 5.0, 5.3,$ and 5.6 ± 0.15 kW; black brackets indicate different $\dot{m}_{\text{Ar}} = 1, 2, 3, 4, 5, 6, 7,$ and 8 L/min. Oxidation: $\dot{m}_{\text{CO}_2} = 7$ L/min, $T_{\text{oxidation-start}} = 900^\circ\text{C}$.

leads to higher V_{O_2} release, explained through the aforementioned effect of more ceria mass at higher temperatures due to the elongated $\Delta t_{\text{reduction}}$. Note that the results for different P_{solar} for higher \dot{m}_{Ar} are highly scattered, and comparing the results becomes challenging due to other variables changing with P_{solar} , such as $\Delta t_{\text{reduction}}$ or the temperature distribution within the RPC. Higher V_{O_2} during reduction implies higher V_{CO} during oxidation. However, Q_{solar} also increases due to the longer $\Delta t_{\text{reduction}}$, which outweighs the increase in fuel yield and leads to lower $\eta_{\text{solar-to-syngas}}$. On the other hand, $\eta_{\text{solar-to-syngas}}$ is staying constant or is slightly decreasing with higher \dot{m}_{Ar} . Highest V_{O_2} is reached for the highest $T_{\text{reduction-end}}$ of 1500°C , low P_{solar} and highest \dot{m}_{Ar} of 8 L/min. Highest $\eta_{\text{solar-to-syngas}}$ is reached for the highest $T_{\text{reduction-end}}$ of 1500°C , high P_{solar} and \dot{m}_{Ar} around 3 L/min. There is a clear trade-off between optimising for fuel yield or for efficiency.

3.2 Oxidation Parameters Co-splitting

Figure 3.2 shows the oxidation step of the cycle with varying parameters $T_{\text{oxidation-start}}$, \dot{m}_{CO_2} and \dot{m}_{H_2O} while keeping the others constant. Each data point corresponds to one experimental cycle. Each subfigure shows the results for the three different targeted cumulative $R_{H_2:CO} = 1.8$ (blue), 2 (red) and 2.2 (yellow). For each $R_{H_2:CO}$, plotted are the cumulative syngas ($CO + H_2$) output V_{syngas} , X_{CO_2} , $\Delta t_{\text{oxidation}}$ until $R_{H_2:CO}$ is reached, and $\eta_{\text{solar-to-syngas}}$. Lower $T_{\text{oxidation-end}}$ increases both $\Delta t_{\text{oxidation}}$ and $\Delta t_{\text{reduction}}$ and hence Q_{solar} as well as Q_{pump} and Q_{inert} of that cycle. Note that the numerical value of $\eta_{\text{solar-to-syngas}}$ is strongly dependent on P_{solar} during the reduction phase. For all cycles, the reduction was performed with $\dot{m}_{\text{Ar}} = 3$ L/min, $p_{\text{reactor}} = 50\text{-}200$ mbar, and $T_{\text{reduction-end}} = 1500^\circ\text{C}$. To minimize the influence of varying P_{solar} , $\eta_{\text{solar-to-syngas}}$ has been determined by integrating over time the heating value of the fuel (CO, H_2) produced over the sum of the solar radiative energy input Q_{solar} and the energy inputs associated with vacuum pumping Q_{pump} and inert gas consumption Q_{inert} (see definition of $\eta_{\text{solar-to-syngas}}$ in section 2.5, Eq. 2.4) for a reference

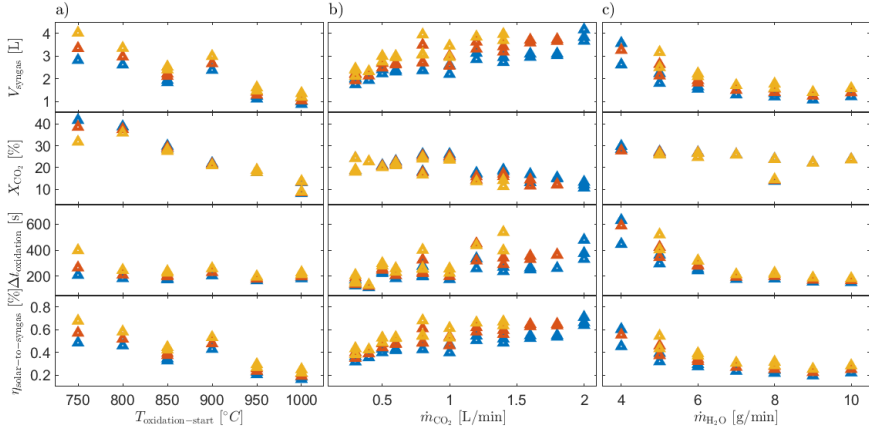


Figure 3.2: Parametric study of oxidation parameters. V_{syngas} , X_{CO_2} , $\Delta t_{\text{oxidation}}$ and $\eta_{\text{solar-to-syngas}}$ over varying $T_{\text{oxidation-start}}$ a), oxidation flows \dot{m}_{CO_2} b) and $\dot{m}_{\text{H}_2\text{O}}$ c). a) Varying $T_{\text{oxidation-start}}$, $\dot{m}_{\text{CO}_2} = 0.6$ L/min, $\dot{m}_{\text{H}_2\text{O}} = 10$ g/min. b) $T_{\text{oxidation-start}} = 900^\circ\text{C}$, varying \dot{m}_{CO_2} , $\dot{m}_{\text{H}_2\text{O}} = 10$ g/min. c) $T_{\text{oxidation-start}} = 900^\circ\text{C}$, $\dot{m}_{\text{CO}_2} = 0.4$ L/min, varying $\dot{m}_{\text{H}_2\text{O}}$. The colours mark different $R_{\text{H}_2:\text{CO}}$: $R_{\text{H}_2:\text{CO}} = 2.2$ (yellow), $R_{\text{H}_2:\text{CO}} = 2$ (red), $R_{\text{H}_2:\text{CO}} = 1.8$ (blue). Reduction: $T_{\text{reduction-end}} = 1500^\circ\text{C}$, $p_{\text{reactor}} = 50\text{-}200$ mbar, $\dot{m}_{\text{Ar}} = 3$ L/min.

reduction run from $T_{\text{reduction-start}} = T_{\text{oxidation-end}}$ to $T_{\text{reduction-end}}$ with $P_{\text{solar}} = 5.3 \text{ kW}$. Note that the varying p_{reactor} is the result of condensed water accumulating in the system over consecutive cycles. $X_{\text{H}_2\text{O}} = 2\text{-}6\%$, but its value is less critical since the removal of unreacted H_2O through condensation is technically feasible (implemented experimentally, see Fig. 2.1) at low cost and the removed H_2O can be readily recycled. $X_{\text{H}_2\text{O}}$ is significantly lower than X_{H_2} due to the longer residence time of CO_2 in the reactor during the cool-down phase until the start of the oxidation flows. Furthermore, at the same T and p , oxidation with CO_2 (Eq. 1.2) is thermodynamically more favorable compared to oxidation with H_2O (Eq. 1.3). The gas stream leaving the redox unit is free of H_2O but contains unreacted CO_2 , which is undesired for the FT synthesis but could be used in the methanol synthesis (see chapter 2.3).

Figure 3.2a shows the performance values for different $T_{\text{oxidation-start}}$ between 750°C and 1000°C , with \dot{m}_{CO_2} and $\dot{m}_{\text{H}_2\text{O}}$ during oxidation kept constant at 0.6 L/min and 10 g/min , respectively. Note that for cycles with $T_{\text{oxidation-start}} < 750^\circ\text{C}$ the targeted $R_{\text{H}_2:\text{CO}}$ could not be reached with the given \dot{m}_{CO_2} and $\dot{m}_{\text{H}_2\text{O}}$. V_{syngas} , X_{CO_2} and $\eta_{\text{solar-to-syngas}}$ decrease with $T_{\text{oxidation-start}}$. Although $\Delta t_{\text{oxidation}}$ stays constant, lowering $T_{\text{oxidation-start}}$ directly leads to an increase of $\Delta t_{\text{cool-down}}$ and hence affects Δt_{cycle} as well as $T_{\text{oxidation-end}}$ (or $T_{\text{reduction-start}}$), which in turn has an effect on the energy input terms Q_{solar} , Q_{pump} and Q_{inert} of the $\eta_{\text{solar-to-syngas}}$. Furthermore, a longer $\Delta t_{\text{cool-down}}$ during which the ceria in the reactor is oxidising and generating CO, results in a CO peak at the beginning of oxidation as soon as the oxidation flows start. This CO peak is higher with lower $T_{\text{oxidation-start}}$ given the longer residence time at more favourable oxidation conditions in the reactor. It then takes more H_2 to compensate and reach the desired $R_{\text{H}_2:\text{CO}}$, leading to the higher V_{syngas} and $\eta_{\text{solar-to-syngas}}$. If $T_{\text{oxidation-start}} < 750^\circ\text{C}$, the H_2 produced is not enough to compensate the higher CO peak and reaching $R_{\text{H}_2:\text{CO}}$. This cut out is dependent on the oxidation flow conditions. Same situation for increasing \dot{m}_{CO_2} , which leads to higher CO production that cannot be compensated with the unchanged $\dot{m}_{\text{H}_2\text{O}}$. The

higher CO peak for the same \dot{m}_{CO_2} also explains the higher X_{CO_2} for the lower $T_{\text{oxidation-start}}$.

Figure 3.2b shows the performance values for varying \dot{m}_{CO_2} during oxidation with $T_{\text{oxidation-start}}$ kept constant at 900°C and $\dot{m}_{\text{H}_2\text{O}}$ kept constant at 10 g/min. Note that the maximum \dot{m}_{CO_2} for which the target $R_{\text{H}_2:\text{CO}}$ could be reached was 1.4 L/min for $R_{\text{H}_2:\text{CO}} = 2.2$, 1.8 L/min for $R_{\text{H}_2:\text{CO}} = 2$ and 2 L/min for $R_{\text{H}_2:\text{CO}} = 1.8$. V_{syngas} , $\Delta t_{\text{oxidation}}$ and $\eta_{\text{solar-to-syngas}}$ increase with \dot{m}_{CO_2} while the opposite is true for X_{CO_2} . As $T_{\text{oxidation-start}}$ remains constant, $\Delta t_{\text{cool-down}}$ also stays constant, leading to the same amount of CO formed in the reactor before the start of the oxidation flows. Higher \dot{m}_{CO_2} leads to higher CO production and more H_2 needed to reach the desired $R_{\text{H}_2:\text{CO}}$, hence the rising V_{syngas} . This is also the explanation for the longer $\Delta t_{\text{oxidation}}$ and the higher $\eta_{\text{solar-to-syngas}}$. Higher \dot{m}_{CO_2} also leads to a decrease in X_{CO_2} by more unreacted CO_2 , which can be used for methanol synthesis but is less critical for FT synthesis, besides the detrimental effect of diluting the syngas mixture.

Figure 3.2c shows the performance values for varying $\dot{m}_{\text{H}_2\text{O}}$ during oxidation, with $T_{\text{oxidation-start}}$ kept constant at 900°C and \dot{m}_{CO_2} kept constant at 0.4 L/min. Note that the minimum $\dot{m}_{\text{H}_2\text{O}}$ for which the target $R_{\text{H}_2:\text{CO}}$ could be reached was 5 g/min for $R_{\text{H}_2:\text{CO}} = 2.2$ and 4 g/min for $R_{\text{H}_2:\text{CO}} = 1.8$ and $R_{\text{H}_2:\text{CO}} = 2$. V_{syngas} , X_{CO_2} , $\Delta t_{\text{oxidation}}$ and $\eta_{\text{solar-to-syngas}}$ decrease with $\dot{m}_{\text{H}_2\text{O}}$. This effect is more pronounced at lower $\dot{m}_{\text{H}_2\text{O}}$ while the performance values stay almost constant above $\dot{m}_{\text{H}_2\text{O}} = 7$ g/min. As $T_{\text{oxidation-start}}$ remains constant, $\Delta t_{\text{cool-down}}$ also stays constant. Lower $\dot{m}_{\text{H}_2\text{O}}$ result in lower H_2 production rates which also allows more CO_2 to react in the meantime and hence increasing V_{syngas} . Analogous to the discussion of Fig. 3.2a and b, $\eta_{\text{solar-to-syngas}}$ is dominated by V_{syngas} . X_{CO_2} is higher for lower $\dot{m}_{\text{H}_2\text{O}}$ as this allows for longer residence time and, thus, more of the CO_2 to react. The total outlet flow is much more dependent on the changes in $\dot{m}_{\text{H}_2\text{O}}$ due to the high H_2O to CO_2 oxidation feed ratio.

Figure 3.2a, b, and c indicates that, when targeting higher values of $R_{\text{H}_2:\text{CO}}$, V_{syngas} , $\Delta t_{\text{oxidation}}$ and $\eta_{\text{solar-to-syngas}}$ increase, while X_{CO_2} de-

creases. A higher $R_{\text{H}_2:\text{CO}}$ leads to longer gas collection in that cycle, as the CO peak is ahead of the H₂ peak. This explains the increased V_{syngas} , $\Delta t_{\text{oxidation}}$ and $\eta_{\text{solar-to-syngas}}$ as the higher Q_{fuel} again outweighs the increase in Q_{solar} , Q_{pump} and Q_{inert} . In contrast, X_{CO_2} decreases as there is more unreacted CO₂ leaving the reactor due to much lower \dot{X}_{CO_2} later in the oxidation. The influence of this effect is bigger with higher \dot{m}_{CO_2} as the initial CO₂ in the reactor remains unchanged. Note that, as mentioned above, some cycles with higher target $R_{\text{H}_2:\text{CO}}$ will not reach the target composition, while lower target $R_{\text{H}_2:\text{CO}}$ are possible.

In addition to the experimental results of Fig. 3.2 the same experiments have also been conducted for a complete second set of parameter variations with $\dot{m}_{\text{CO}_2} = 0.8$ L/min instead of 0.6 L/min in Fig. 3.2a, $T_{\text{oxidation-start}} = 800^\circ\text{C}$ instead of 900°C Fig. 3.2b, and $T_{\text{oxidation-start}} = 850^\circ\text{C}$ instead of 900°C oxidation start in Fig. 3.2c. This additional set of results confirms the trends and finding of Fig. 3.2 with only minimal changes due to the changed parameters. Notably the cut-off for cycles that just reach the target $R_{\text{H}_2:\text{CO}}$ shifts depending on the parameters, pointing out the challenges in finding optimal operation conditions and the need for an automated optimisation scheme.

3.3 Separate Splitting of CO₂ and H₂O

Alternative to co-splitting of H₂O and CO₂ in a single cycle, as shown above, H₂O and CO₂ splitting cycles can be performed separately with the same solar reactor. Pure CO₂ splitting has been previously demonstrated for a 4kW reactor in a laboratory setup using a high-flux solar simulator [40] and during the stable cycling demonstration in chapter 2.2. This chapter shows an experimental parametric study with separate H₂O and CO₂ splitting cycles, targeting high syngas quality.

3.3.1 Oxidation of CO₂-splitting

Figure 3.3 shows an experimental parametric study of the oxidation step of the CO₂-splitting cycle aiming at high conversion of CO₂. As expected, peak \dot{X}_{CO_2} , peak \dot{m}_{CO} and final V_{CO} increase with lower $T_{\text{oxidation-start}}$, but the curves become flatter with lower \dot{m}_{CO_2} due to the lower total outlet flow. Furthermore, $\dot{m}_{\text{CO}_2} = 1$ L/min is too low to fully oxidise the reactor, hence resulting in a lower final V_{CO} . The peak \dot{X}_{CO_2} is 80.1% and the peak X_{CO_2} is 65.9% for $\dot{m}_{\text{CO}_2} = 2$ L/min, comparable to the previously reported values obtained with the lab scale 4 kW reactor [40]. As X_{CO_2} decreases after the peak while V_{CO} further increases, there is evidently a trade-off between conversion and yield.

3.3.2 Oxidation of H₂O Dominant Co-splitting

In principle, pure H₂O-splitting is also feasible with the same reactor. However, a minimum carrier gas flow of 0.1 L/min is needed for the steam generator used in this study and for re-pressurising the reactor after reduction due to the high water condensation rates in the downstream gas piping. The use of an inert gas such as Ar for this purpose is technically feasible but undesired because of the inefficiencies associated of carrying an inert gas through the GTL-process and the energy penalty of separating and recycling it. For this reason, CO₂ was chosen instead of Ar as both carrier gas as well as to re-pressurise the reactor, not leading to pure H₂O-splitting cycles but rather resulting in a different form of co-splitting cycles with a high H₂O:CO₂ feed ratio, targeting syngas with high H₂:CO ratio.

Figure 3.4 shows an experimental parametric study of such co-splitting cycles aiming at high conversion of both H₂O and CO₂. In contrast to pure CO₂-splitting, the total gas outlet flow is not constant because unreacted water is condensed out before the gas analysis. Note that, towards the end of oxidation, a flush gas flow of CO₂ was introduced for the purpose of collecting the H₂-rich syngas remaining in the reactor. The introduction

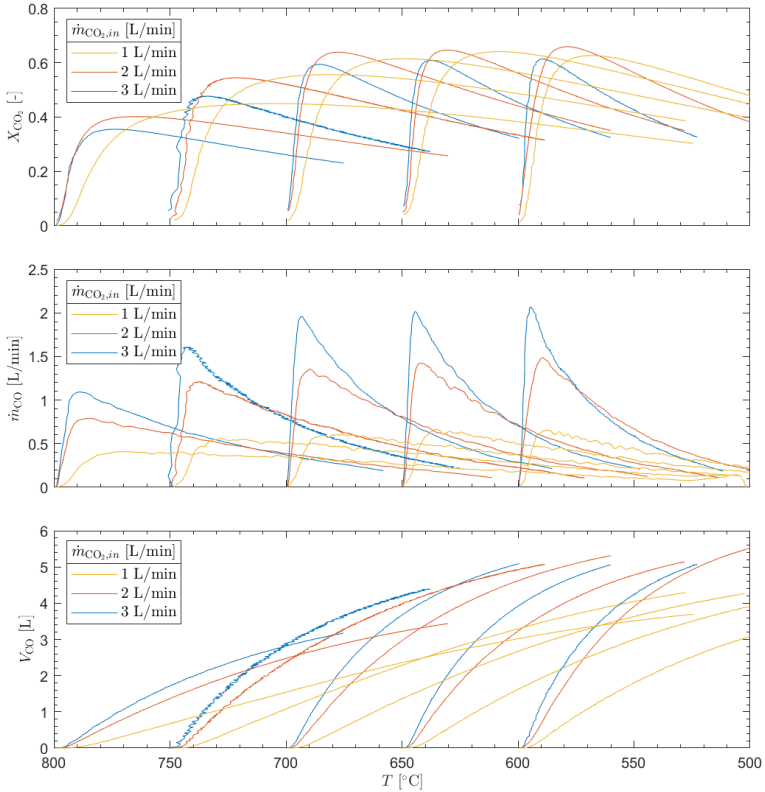


Figure 3.3: CO_2 splitting — X_{CO_2} , \dot{m}_{CO} and V_{CO} as a function of temperature T during oxidation for different $T_{\text{oxidation-start}} = 600, 650, 700, 750, 800$ °C and $\dot{m}_{\text{CO}_2} = 1, 2,$ and 3 L/min (indicated by different colours). Reductio conditions: $T_{\text{reduction-end}} = 1500$ °C , $\dot{m}_{\text{Ar}} = 3$ L/min. Oxidation conditions: gas collection was terminated once CO concentration in the outlet gas dropped below 10%.

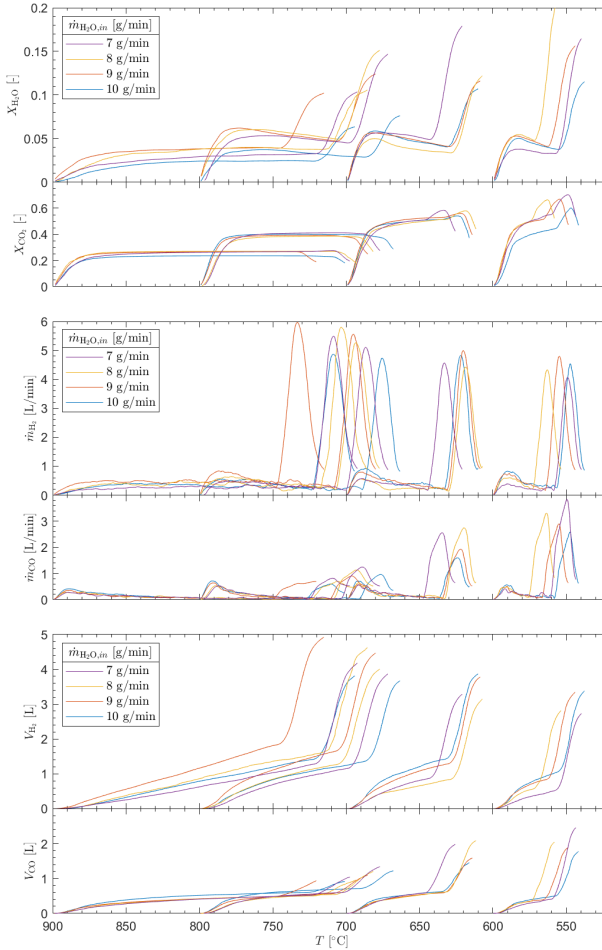


Figure 3.4: Co-splitting with high H₂O:CO₂ feed ratio — Cumulative conversions $X_{\text{H}_2\text{O}}$ and X_{CO_2} , instantaneous mass flows \dot{m}_{H_2} and \dot{m}_{CO} and cumulative yields V_{H_2} and V_{CO} as a function of temperature T during oxidation for $T_{\text{oxidation-start}} = 600, 700, 800,$ and 900 °C and $\dot{m}_{\text{H}_2} = 7, 8, 9,$ and 10 g/min (indicated by different colours). Reduction: $T_{\text{reduction-end}} = 1500$ °C, $\dot{m}_{\text{Ar}} = 3$ L/min. Oxidation: $\dot{m}_{\text{CO}_2} = 0.1$ L/min. Flush gas flow of 10 L/min CO₂ introduced once the measured total gas flow exiting the system dropped below 0.2 L/min averaged over a 5 s time period. Syngas collection was terminated once H₂ concentration dropped below 10%.

of this CO_2 flush gas flow is visible as sudden and steep increase in $X_{\text{H}_2\text{O}}$, \dot{m}_{H_2} , V_{H_2} , \dot{m}_{CO} and V_{CO} towards the end of each signal curve.

$T_{\text{oxidation-start}} = 600^\circ\text{C}$ leads to $R_{\text{H}_2:\text{CO}} < 2$, hence the syngas of this cycle would not be optimal for FT synthesis. $T_{\text{oxidation-start}} = 700^\circ\text{C}$ leads to $R_{\text{H}_2:\text{CO}} \approx 2$ and the syngas is suitable for FT synthesis. X_{CO_2} for those cycles reaches 58.5% peak. $T_{\text{oxidation-start}} = 800^\circ\text{C}$ leads to $R_{\text{H}_2:\text{CO}} > 2$. X_{CO_2} for those cycles reaches 40.8% peak and the syngas could be combined with pure CO_2 -splitting cycles to obtain $R_{\text{H}_2:\text{CO}} = 2$. $T_{\text{oxidation-start}} = 900^\circ\text{C}$ leads to comparable results as those obtained for $T_{\text{oxidation-start}} = 800^\circ\text{C}$ but with lower X_{CO_2} and $X_{\text{H}_2\text{O}}$. Cycles with $T_{\text{oxidation-start}} = 1000$ and 1100°C (not shown in Fig. 3.4) have also been performed and exhibit similar behaviour as the cycles with $T_{\text{oxidation-start}} = 900^\circ\text{C}$ but with lower conversions, consistent with the equilibrium thermodynamics of Eq. 1.2 and 1.3.

3.4 Summary and Conclusions

The results of this chapter show how the syngas product quality can be tailored for Fischer-Tropsch synthesis by selecting adequate oxidation conditions, eliminating the need for additional downstream refining of the syngas.

The parametric study of the reduction parameters p_{reactor} , \dot{m}_{Ar} , $T_{\text{reduction-end}}$ and P_{solar} shows that the highest V_{O_2} is reached for the highest $T_{\text{reduction-end}}$ of 1500°C , low P_{solar} and highest \dot{m}_{Ar} of 8 L/min. Highest $\eta_{\text{solar-to-syngas}}$ is reached for the highest $T_{\text{reduction-end}}$ of 1500°C , high P_{solar} and \dot{m}_{Ar} around 3 L/min. There is a clear trade-off between optimising for fuel yield or for efficiency.

The parametric study with varying oxidation parameters $T_{\text{oxidation-start}}$, \dot{m}_{CO_2} , $\dot{m}_{\text{H}_2\text{O}}$ and $R_{\text{H}_2:\text{CO}}$ shows that V_{syngas} and $\eta_{\text{solar-to-syngas}}$ increase with lower $T_{\text{oxidation-start}}$ and $\dot{m}_{\text{H}_2\text{O}}$ and higher \dot{m}_{CO_2} and $R_{\text{H}_2:\text{CO}}$. The highest values lie on the border of the parameter space leading to cycles reaching the target $R_{\text{H}_2:\text{CO}}$ and parameters for cycles that can not reach it anymore. X_{CO_2} increases with lower $T_{\text{oxidation-start}}$, \dot{m}_{CO_2} , $\dot{m}_{\text{H}_2\text{O}}$ and

$R_{\text{H}_2:\text{CO}}$.

The parametric study for CO_2 -splitting shows peak \dot{X}_{CO_2} of 80.1% and peak X_{CO_2} of 65.9% for $\dot{m}_{\text{CO}_2} = 2 \text{ L/min}$, comparable to previously reported values obtained with a lab scale 4 kW reactor [40]. There is a trade-off between conversion and yield as X_{CO_2} decreases after the peak while V_{CO} further increases.

The parametric study for H_2O heavy co-splitting cycles show that $T_{\text{oxidation-start}} = 700^\circ\text{C}$ leads to syngas suitable for FT synthesis with X_{CO_2} of 58.5% peak. $T_{\text{oxidation-start}} = 800^\circ\text{C}$ leads to cycles with X_{CO_2} of 40.8% peak which could be combined with pure CO_2 -splitting cycles to produce syngas suitable for FT synthesis.

CONTROL AND AUTOMATION OF THE SOLAR FUEL SYSTEM ¹

This chapter focusses on the control and automation of the fuel system for effecting the redox cycles to deliver syngas of desired composition. It details the underlying control logic of the automation, the implementation into a LabView control program and finally shows an auto-optimisation scheme based on feedback control loops to conduct fully-automated consecutive redox cycles for the optimisation of the solar fuel system. Note that all redox cycling experiments shown in this thesis have been conducted using the supervisory control and data acquisition (SCADA) program developed and described in this chapter, or simplified versions thereof.

¹Parts of this chapter are in press as: Schäppi, R. *et. al.*, Solar Thermochemical Production of Syngas from H₂O and CO₂ — Experimental Parametric Study, Control, and Automation. *Industrial & Engineering Chemistry Research*, (2024).

4.1 Automation Control Logic

The operation of the solar fuels system, including the sun-tracking of the solar concentrator, the rotation of the secondary reflector, and the execution of consecutive redox cycles, is fully automated using a LabView program that incorporates instantaneous online analysis and feedback control. The SCADA program runs independent tasks in parallel while exchanging measurement data and setting operational parameters. Figure 4.1 shows the automation flow diagram, encompassing 4 blocks. 1) The process flow chart, indicating set operational parameters (dark red) and measured data (light red). 2) The control program logic (purple box), comprising 8 logical blocks. The data acquisition reads the measurement data from the solar redox unit (dashed lines). The online analysis uses the acquired live data and calculates the performance indicators (X_{CO_2} , $X_{\text{H}_2\text{O}}$, V_{syngas} , $R_{\text{H}_2:\text{CO}}$, $\eta_{\text{solar-to-syngas}}$) and cycle times ($\Delta t_{\text{reduction}}$, $\Delta t_{\text{cool-down}}$, $\Delta t_{\text{oxidation}}$, Δt_{cycle}). The data and performance logging creates and writes log files containing settings, measurement data and additional performance parameters. The instrument control sends set points to the different instruments of the fuel system (solid arrows). The display and user interface shows the live measurements and performance indicators and offers controls to manually set and/or overwrite instrument settings and signals. The safety control checks online measurements for unexpected anomalies (e.g. low cooling water flows, valve malfunctions, oxygen in oxidation flow) and starts safety procedures if needed. Note that additional measurements for process safety such as cooling water flows and various surface and air temperatures are not depicted in Fig. 4.1 for simplicity, but are an integral part of the safety control. 3) The cycling control logic (blue box) is the core element of the automation and controls the continuous cycling of both reactors in parallel based on feedback loops. The control waits for the start signal and sets all process settings for the chosen first reactor to go on sun and start its redox cycling. This step includes the setting of the reduction flows, starting the controlled evacuation and directing the solar input to the chosen reactor by rotating the secondary reflector

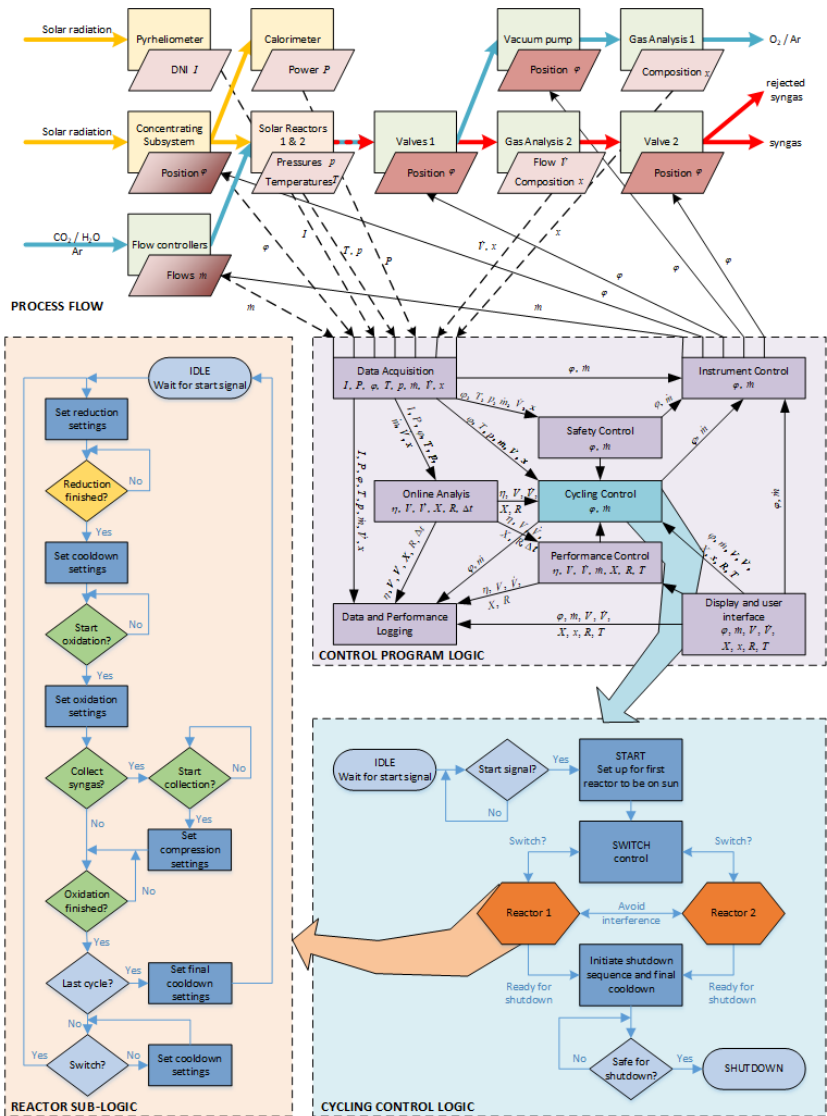


Figure 4.1: Automation flow diagram: 1) process flow chart (top) indicating set operational parameters (dark red) and measured data (light red); 2) control program logic (purple box) with arrows representing forwarded parameter values; 3) cycling control logic (blue box) and; 4) reactor sub-logic (orange box).

of the optical system. 4) The reactor sub-logic, which controls the two reactors and their own feedback based cycling subroutines (orange hexagons and orange box) while being connected via the switch control. The switch control determines which reactor is connected to which downstream device (e.g., vacuum pump during reduction; syngas analysis during oxidation) through valves 1 and also ensures both reactors do not interfere with each other, i.e. only one reactor can be on-sun and perform the reduction step while the other reactor can perform the oxidation step using the $\text{H}_2\text{O}/\text{CO}_2$ mixture coming from the steam generator. The continuous cycling of each reactor is controlled by the logic outlined in the orange box flowchart. The reactor is first set up for on-sun reduction by turning the secondary reflector to focus high-flux solar irradiation into the reactor's aperture, setting the reduction gas flows (i.e. \dot{m}_{Ar}), and starting the controlled evacuation of the reactor based on a feedback loop and a combination of three 2-way valves to gradually decrease the reactor pressure. Once $T_{\text{reduction-end}}$ is reached, the settings are changed to off-sun by turning the secondary reflector away and re-pressurising the reactor. Once $T_{\text{oxidation-start}}$ is reached, the oxidation flows are set. The system waits for the syngas collection start criterion (e.g. collection start temperature or a target initial gas composition) and checks whether the oxidation end criterion is met. Once the oxidation step is terminated, the performance control evaluates the results of the online analysis, determines the performance indicators, and changes accordingly the operational parameters of the next cycle. In case the second reactor is still performing the reduction step, an additional cooldown phase is performed before the start of the next reduction (i.e. until the second reactor is off-sun). Once the command is given to finish the experimental run through the user interface, the reactors will each complete the current cycles ending with a final cool-down phase until the system is safe for shutdown.

4.2 LabVIEW Implementation

The control logic as described in chapter 4.1 has been implemented in a LabVIEW SCADA program. LabVIEW is a graphical programming environment and system engineering software targeting applications where tests, measurements and controls with rapid access to hardware and data insights are important. In case of the solar fuel system this allows for direct integration of the NI data acquisition modules, installed to connect the various sensors, valves and measurement devices, into the control software, and hence allowing the implementation of feedback controls directly, dependent on measurements and online data analysis.

The developed program itself consists of over 120 interlinked subprograms and auxiliary files out of which the most important functions are listed in this chapter. Making use of LabVIEW's parallel programming environment, the core file contains the graphical user interface (GUI) and runs the following background tasks in parallel while passing parameters and commands between them:

- A GUI update loop, that updates the GUI with measurement data, results of the data analysis and automated control setting changes. Also containing a function for instantaneous calculations of selected performance values.
- An event handling loop, that relays the manual system inputs.
- A message handling loop, that forwards the needed commands based on the manual inputs.
- A secondary display, showing the real-time results of the online analysis of reactor cycles and full day experimental summaries.
- The motor control, used to turn the secondary reflector in order to move the focal point (and hence the solar input) to the defined positions.

- The data acquisition subprogram, reading the measurement sensor signals, transform them into measurement values and assigning them to the respective variables.
- The data logging subprogram, writing the measured data and instant analysis into two separate logfiles.
- The flux camera subprogram, controlling the flux measurement camera and saving images upon user input.
- The valves subprogram, controlling the valve positions and gas flow directions throughout the system.
- The vacuum pump subprogram, controlling the vacuum pump and adjacent valves to control the reactor pressure. Also used to evacuate the reactors in a controlled manner by using a combination of proportional and 2-way valves following a predefined pressure evacuation curve based on a direct pressure feedback loop.
- The calorimeter subprogram, performing the calorimeter measurements and calculations. Every calorimeter measurement at steady state also updates the factor relating P_{solar} to the DNI measured by the pyrheliometer.
- The automated reactor cycling subprogram, allowing for fully automated full day experimental runs based on the cycling control logic as described in chapter 4.1.

The GUI displays all the measurements of the various thermocouples, pressure sensors, gas analysis, flow controllers and meters, pyrheliometer and secondary reflector position, and on a second screen the current performance values as well as temporal evolutions of selected parameters and a cycle by cycle summary of the daily measurement runs. The GUI also contains all the controls for manual inputs. For safety reasons, the program is set up in a way that even while the automated cycling is running, the user always has

the option to directly interfere with the setup, change settings or manually take over control.

The automated reactor cycling subprogram is the core program of the automation part. It follows the program logic detailed in the blue and orange boxes of Fig. 4.1 to cycle with both reactors through the different cycling stages while continuously analysing the performance values and avoiding interference between the two cycling reactors.

4.3 Auto-optimisation of Full Day Run

As mentioned in 4.1 the automation for regular and controlled reactor cycling can be further extended with an auto-optimisation scheme that allows the system to change parameter setting from cycle to cycle in order to improve the reactor performance. Based on the fully automated cycling and the parametric study presented in 3.2, a feedback/feed-forward control was implemented to optimise the reactor performance for given targets.

Although affecting each other, the reduction step (Eq. 1.1) and the oxidation step (Eq. 1.2 and 1.3) can in principle be optimised independently, but the reduction affects the oxidation capacity given by δ , and hence the fuel yield during the oxidation, which, in turn, affects $\eta_{\text{solar-to-syngas}}$. From the discussion in chapter 3.1, it is clear that $T_{\text{reduction-end}}$ should be chosen as high as possible for maximising yield, the limit being the mechanical and chemical stability of the ceria RPC structure. On the other hand, as shown in Figs. 3.1 and 3.2 of chapter 3.1 and 3.2 and the discussion thereof, there is a trade-off between maximising yield and efficiency. Thus, an automated optimisation approach based on feedback and prediction control is used to optimise the oxidation parameters once the reduction parameters are set.

4.3.1 Auto-optimisation Description

A combined performance indicator CPI is introduced as a measure of cycle performance, allowing to compare different cycles according to pre-

defined prioritisation. The *CPI* is defined based on the weighted sum of the investigated performance indicators PI_i , normalised by their reference values $PI_{i,\text{ref}}$ (see eq. 4.1). Four *PIs* were investigated, namely: the syngas output per cycle V_{syngas} , the syngas output per time \dot{V}_{syngas} (taking into account the changes in cycle time), X_{CO_2} and $\eta_{\text{solar-to-syngas}}$. V_{syngas} is an important parameter when comparing single reactor cycles, while \dot{V}_{syngas} is important especially when looking at continuous fuel production. Optimising for high \dot{V}_{syngas} optimises for maximum syngas yield e.g. over a day or week, and is hence probably the most important optimisation parameter to consider for upscaling and continuous production. X_{CO_2} has an influence on the quality of the syngas and low conversion can affect the downstream GTL process. The importance of X_{CO_2} depends on the GTL process used, e.g. methanol synthesis or FT-synthesis. $\eta_{\text{solar-to-syngas}}$ is a characteristic number important for both comparing single cycles as well as continuous production. \dot{V}_{syngas} and $\eta_{\text{solar-to-syngas}}$ are closely related and are generally optimised through similar settings. Both parameters are also directly related to economics and production costs. Setting $PI_{i,\text{ref}}$ and weight factors w_i enables to prioritise certain *PIs* above others, making the optimisation scheme adjustable to different needs.

$$\begin{aligned}
 CPI &= \sum \frac{PI_i}{PI_{i,\text{ref}}} w_{PI_i} \\
 &= \frac{V_{\text{syngas}}}{V_{\text{syngas,ref}}} w_{V_{\text{syngas}}} + \frac{\dot{V}_{\text{syngas}}}{\dot{V}_{\text{syngas,ref}}} w_{\dot{V}_{\text{syngas}}} + \frac{X_{\text{CO}_2}}{X_{\text{CO}_2,\text{ref}}} w_{X_{\text{CO}_2}} \quad (4.1) \\
 &+ \frac{\eta_{\text{solar-to-syngas}}}{\eta_{\text{solar-to-syngas,ref}}} w_{\eta_{\text{solar-to-syngas}}}
 \end{aligned}$$

The *CPI* is calculated after every cycle (i.e. termination criterion reached). Additionally, predictions of the value of *CPI* for changes in oxidation parameters are calculated based on the results of the parametric study and set step size. Given that the 3 oxidation parameters $T_{\text{oxidation-start}}$, \dot{m}_{CO_2} , $\dot{m}_{\text{H}_2\text{O}}$ and can be increased, held constant, or decreased, this leads to 26 predictions of *CPIs* in addition to the current value. In an automated

run the system will choose the parameters representing the highest CPI to be used in the next cycle. Although predicted CPI s generally show good agreement with measured CPI s, perfect agreement is unlikely because of the changing external inputs, especially P_{solar} . Note that not all parameter settings are feasible to achieve a required $R_{\text{H}_2:\text{CO}}$ in the syngas. This is critical, especially given that the maximum values for most of the PI s lie on the border between parameter combinations that lead to cycles reaching the target $R_{\text{H}_2:\text{CO}}$ and combinations that do not (see chapter 3.2). Known parameter combinations that do not lead to cycles reaching $R_{\text{H}_2:\text{CO}}$ can be stored, and used as preknowledge to rule out areas of parameter combinations not to be tested again. Should the cycle not reach the desired $R_{\text{H}_2:\text{CO}}$, the next parameter set is chosen based on the last cycle that achieved the desired $R_{\text{H}_2:\text{CO}}$. The feasible parameter space could be further tightened by adding limits, e.g. a minimum X_{CO_2} . The maximum CPI determines the optimum parameter set. However, it is possible that this is only a local rather than a global optimum and other starting conditions might have to be investigated.

4.3.2 Experimental Results and Discussion

Figure 4.2 shows an example of such an optimisation run for one reactor. Shown are the varying oxidation parameters $T_{\text{oxidation-start}}$, \dot{m}_{CO_2} and $\dot{m}_{\text{H}_2\text{O}}$, the measured $P_{\text{solar,mean}}$ and the measured/calculated PI s V_{syngas} , \dot{V}_{syngas} , X_{CO_2} and $\eta_{\text{solar-to-syngas}}$ over 8 consecutive cycles. Oxidation was terminated when either the target $R_{\text{H}_2:\text{CO}} = 2$ was reached (bold markers, cycle 1,2,3,6) or the composition of the outlet gas fell below a certain threshold, for example $\text{CO}+\text{H}_2$ content below 5% or CO/H_2 content below 1% volume fraction (light markers, cycle 4,5,7,8). The first two cycles of that day (not shown in Fig. 4.2) are omitted as their performance is affected by starting up from ambient temperature, i.e. the solar energy is partially used for heating up inert components. For fair comparison and to minimise the influence of the previous cycles, $\eta_{\text{solar-to-syngas}}$ was determined by intergrating the terms of Eq. 2.4 (section 2.5) over time for the reduction step running

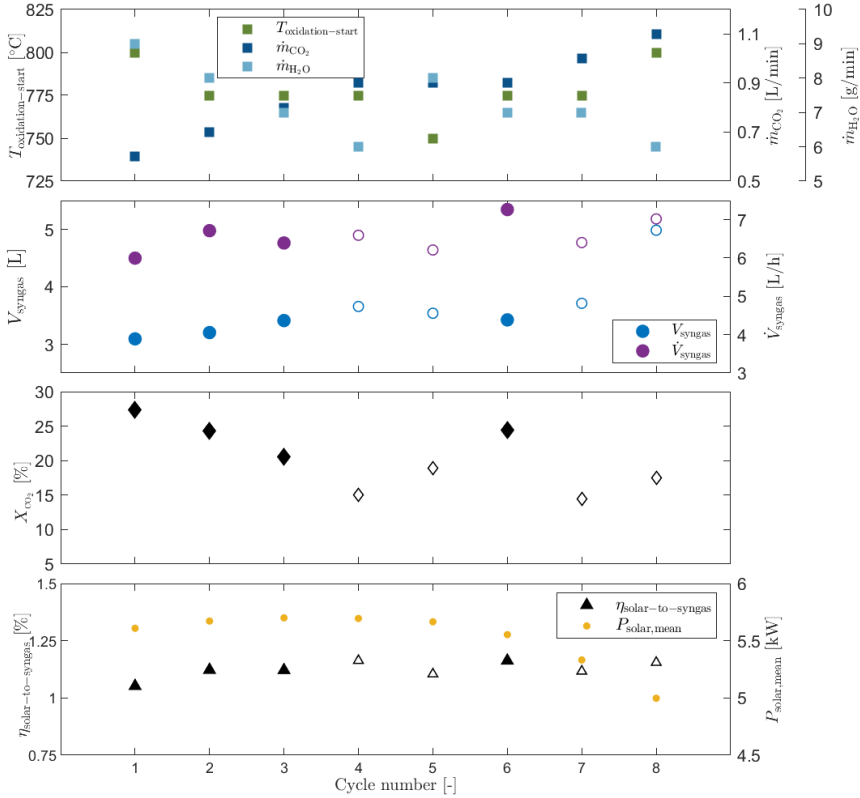


Figure 4.2: Optimisation run with 8 consecutive cycles showing oxidation parameters $T_{\text{oxidation-start}}$, \dot{m}_{CO_2} and $\dot{m}_{\text{H}_2\text{O}}$, measured $P_{\text{solar,mean}}$ and measured/calculated performance parameters V_{syngas} , \dot{V}_{syngas} , X_{CO_2} and $\eta_{\text{solar-to-syngas}}$ as a function of the cycle number. Filled: $R_{\text{H}_2:\text{CO}} = 2$ reached (cycle 1,2,3,6). Empty: $R_{\text{H}_2:\text{CO}} = 2$ not reached (cycle 4,5,7,8). Reduction: $T_{\text{reduction-end}} = 1500^{\circ}\text{C}$, $\dot{m}_{\text{Ar}} = 3 \text{ L}/\text{min}$. Previous knowledge: Cycle with $T_{\text{oxidation-start}} = 750^{\circ}\text{C}$, $\dot{m}_{\text{CO}_2} = 0.7 \text{ L}/\text{min}$ and $\dot{m}_{\text{H}_2\text{O}} = 8 \text{ g}/\text{min}$ does not reach $R_{\text{H}_2:\text{CO}} = 2$. Set $PI_{i,\text{ref}}$ and w_i for CPI calculations: $w_{V_{\text{syngas}}} = 10$, $w_{\dot{V}_{\text{syngas}}} = 30$, $w_{X_{\text{CO}_2}} = 30$, $w_{\eta_{\text{solar-to-syngas}}} = 30$, $V_{\text{syngas,ref}} = 5 \text{ L}$, $\dot{V}_{\text{syngas,ref}} = 7.5 \text{ L}/\text{h}$, $X_{\text{CO}_2,\text{ref}} = 0.5$, $\eta_{\text{solar-to-syngas,ref}} = 0.02$. Parameter step sizes: 25°C for $T_{\text{oxidation-start}}$, $0.1 \text{ L}/\text{min}$ for \dot{m}_{CO_2} , $1 \text{ g}/\text{min}$ for $\dot{m}_{\text{H}_2\text{O}}$.

from $T_{\text{reduction-start}} = T_{\text{oxidation-end}}$ to $T_{\text{reduction-end}}$ of that cycle. The results show the expected increase in V_{syngas} and \dot{V}_{syngas} over the cycles, a decrease in X_{CO_2} as it was weighted less than other PI s, and an increase in $\eta_{\text{solar-to-syngas}}$ despite decreasing $P_{\text{solar,mean}}$. Note that cycles 4, 5, 7 and 8 could not reach the target $R_{\text{H}_2:\text{CO}} = 2$ and their parameter settings were skipped. For the chosen $PI_{i,\text{ref}}$ and w_i , the algorithm found a local optimum for the given conditions at $T_{\text{oxidation-start}} = 775^\circ\text{C}$, $\dot{m}_{\text{CO}_2} = 0.9$ L/min and $\dot{m}_{\text{H}_2\text{O}} = 7$ g/min.

Note that these results correspond to running a single reactor. To optimise a multiple reactor system, the solar input will have to be re-directed to the apertures of the solar reactors to drive the endothermic reduction steps without interruption. For a 2-reactor system, as implemented in this setup, that would mean to match $\Delta t_{\text{reduction}}$ of one reactor with $\Delta t_{\text{cool-down}} + \Delta t_{\text{oxidation}}$ of the second reactor.

4.4 Summary and Conclusions

The chapter summarised the implemented control logic and its implementation for controlling the solar red unit and facilitate the fully automated cyclic runs presented in this thesis. In order to optimise for a specific prioritisation of performance indicators, an auto optimisation scheme is introduced. The shown example of a solar run of fully-automated consecutive redox cycles demonstrates that the implementation of the proposed control scheme for the optimisation of the solar fuel system works and indeed leads to higher performance values. In the present study, no attempt was performed to optimize the system for maximum efficiency as the heat losses were significant at this scale. While the control scheme for the performance optimisation shows only modest increase in both syngas yield and efficiency, future work targeting higher performance improvements will need to include physical modifications of the reactor design and its peripheral components, e.g. implementation of hierarchically-ordered ceria structures[86, 87] and/or integration of heat recovery[91].

DYNAMIC GREY BOX MODEL

This chapter describes the development of a dynamic grey box model for the solar redox reactor, shows some first results of a simplified model and presents an application of the model by comparing simulated two reactor and three reactor systems.

As discussed in the previous chapters the outlet composition of the syngas leaving the redox reactor is key to the integration into the process chain to solar fuels. Previous chapters already discussed different ways of controlling the reactor outputs based on changes to the reactor inputs. However, this was all done purely experimental, either by simply trying out different input combinations or by means of an automated software based on direct feedback loops. Another option to further examine the dependence of reactor outputs to reactor inputs and investigate different operation procedures to run the reactors, is by means of a reactor model. Using a reactor model for such studies would potentially reduce the time intensive measurement

campaigns or allow to simulate measurement procedures also when the external conditions do not allow experimental runs. Integrating the reactor model into a larger model of the entire fuel system would allow it to look into optimising the integration of the different process steps and the way the entire system is operated. A reactor model might also allow to test options that are physically not possible to implement in the current system.

As the key interest is the dynamic modelling of the reactor output dependent on varying inputs a grey box model approach was chosen. In difference to white box models — purely theoretical models of fundamental aspects, based on deterministic equations, physiological knowledge and detailed sub-models, with fully known internal states — and purely data and statistic based black box models with a purely input-output representation, no assumed model form and unknown internal states, a grey box model is typically based on physiological knowledge, some known internal dynamics and data, with the internal states partially known. A recent example for a white box model of a similar type redox reactor can be found in Ref. [81] where the model is used to investigate the temperature distribution within the ceria RPC.

Another option compared to a gray box model of the redox reactor to simulate reactor outputs based on reactor inputs, would for example be a computational fluid dynamics (CFD) model. A CFD reactor model is usually a white box model with maybe some fitted parameters, that can provide a deep understanding of the internal states of the reactor. This type of model provides the benefits of detailed reactor insights and is typically used in the design stage of a reactor or to analyse different design options. When only interested in the output of a reactor based on the inputs to the reactor, knowing all internal states is less essential, as long as the model response shows good agreement with measured data sets. The key benefit of a dynamic grey box reactor model compared to a CFD reactor model, if mainly interested in the model outputs dependent on inputs, is the speed of the finalised model (after parameter estimation). The lower computational

cost allows it to be easily integrated into a larger systems model. For example, multiple reactor blocks could be integrated into a system model of the entire solar fuel system containing also models of the DAC unit, the GTL unit, the optical concentrating system, buffer storage tanks and auxiliary systems.

The simulation of the entire solar fuel production system is outside the scope of this thesis. However, the dynamic reactor model presented in this chapter can provide the reactor component — a key stone of the process chain — for future system models.

5.1 Model Description

The methodology of setting up the model in part follows the methodology described by Ref. [92] and [93]. The model is based on energy and mass conservation equations within predefined model domains and considers mass and energy transfer between the domains and over the system boundaries. The model domains are divided in three groups containing solid, gaseous and porous volumes with the redox reactions (Eq. 1.1, Eq. 1.2 and Eq. 1.3) taking place in the porous volumes representing the RPC structure inside the cavity. The model follows a lumped parameter approach to describe the mass and energy reservoirs and is implemented using MATLAB. Unknown system parameters are determined empirically through comparing numerically simulated results to experimental data collected over multiple characteristic cycles with varying process parameters.

The modelled domain is the solar redox reactor described in chapter 2.1.2. System inputs are the solar power input Q_{solar} , cooling water inlet temperature and flow, mass flows and temperatures of the inlet gasses, and the reactor pressure and its derivative. The reactor pressure is modelled as an input, as it can be controlled through the vacuum pump system. System outputs are the outermost RPC temperature, cooling water outlet temperature and the mass flows and temperature of the outlet gasses.

The insert of Fig. 5.1 shows the division of the reactor in different lumped-parameter reservoirs for mass and energy with level variables temperature

T , number of moles per species n_i and ceria nonstoichiometry δ . Figure 5.1 shows the causality diagram of the implemented model, indicating the energy and mass exchanges between the different reservoirs. The solid model domains are divided in domains for the alumina insulation I, Inconel reactor shell S, water cooled aluminium reactor front F and quartz reactor window W. The gas domains are labelled G and cover the volume inside the cavity G1 as well as the gas volume inside the insulation before the reactor outlet G2, G3. The RPC cavity is divided in 4 domains P with the innermost domain P1 displaying the apparent reactor properties important for the radiative heat exchange with the surroundings and P4 being the outermost RPC layer representing the measured reactor temperature. P2 and P3 are two additional RPC domains between P1 and P4 and their volume fraction of the entire RPC is used during parameter fitting to adjust the temperature profile in the reactor.

5.1.1 Model Equations

The general unsteady conservation equation for a generic reservoir is

$$\frac{d(\text{reservoir content})}{dt} = \sum(\text{inflows}) - \sum(\text{outflows}) \quad (5.1)$$

Applying the general conservation equation for the energy balance of a solid (s) non-reacting domain, such as an insulation element, yields:

$$\frac{dT_s}{dt} m_s c_{v,s}(T_s) = Q_{\text{rad},s} + \sum_{\text{reservoir:i}} (Q_{\text{cond},i \rightarrow s} + Q_{\text{conv},i \rightarrow s}) - Q_{\text{conv},s \rightarrow \infty} \quad (5.2)$$

Where the radiation term $Q_{\text{rad},s}$ is only present for the case of the window but is 0 for all other solid non-reacting domains. The quartz window is modelled with a total transmittance of 0.934[83]. Assuming gas outlet temperature equal to the solid temperature, negligible ceria mass loss/gain and neglecting kinetic and potential effects, the energy conservation equation

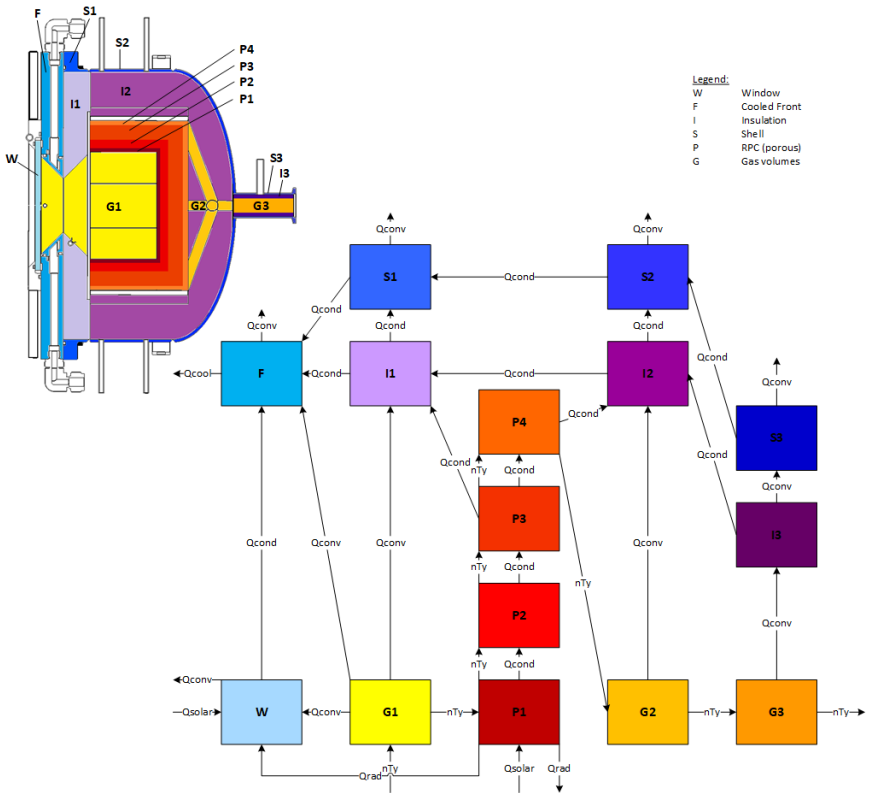


Figure 5.1: Causality diagram of the implemented grey box model containing the gaseous domains G, porous domains P and solid domains I (insulation), S (steel shell), F (water cooled front) and W (window). The arrows between the domains indicate exchanged energy and mass flows. Top left insert: Cross section of modelled reactor with coloured areas corresponding to the domains of the causality diagram.

for a porous (p) domain is:

$$\begin{aligned} \frac{dT_p}{dt} m_p c_{v,p}(T_p) = & Q_{\text{rad},p} + \sum_{\text{reservoir:i}} Q_{\text{cond},i \rightarrow p} + \sum_{\text{species:j}} \dot{n}_{g,j,\text{in}} h_j(T_{\text{in}}) \\ & - \sum_{\text{species:j}} \dot{n}_{g,j,\text{out}} h_j(T_{\text{out}}) + \sum_{\text{species:j}} r_j \Delta H_j \end{aligned} \quad (5.3)$$

The net radiative power Q_{rad} is given by the difference of the solar radiation Q_{solar} absorbed and the re-radiation through the reactor's aperture A_{aperture} :

$$Q_{\text{rad},p} = A_{\text{aperture}} (\alpha_{\text{app}} Q_{\text{solar}} - \epsilon_{\text{app}} \sigma T_p^4) \quad (5.4)$$

where α_{app} is the apparent absorptivity and ϵ_{app} the apparent emissivity of the innermost ceria layer. For cavity geometries approaching blackbody absorbers, α_{app} and ϵ_{app} approach unity. For the conduction and convection terms a combined heat transfer coefficient UA is determined through parameter identification.

$$Q_{\text{conv},s} + Q_{\text{cond},s} = \sum_k UA_{s-k} (T_k - T_s) \quad (5.5)$$

Gas volumes are modelled as continuously stirred without chemical reaction. Ideal gas law is assumed for all involved gas species and the pressure is assumed to be equal in all gas volumes, i.e. no pressure difference between different reservoirs. The total number of moles in a gas reservoir is a function of temperature and pressure. The total outlet flow of a gas reservoir can be calculated with a simple mass balance and the composition of the outlet flow is equal to the composition of the gas reservoir.

Assuming the enthalpy of each species j is a function of temperature only, i.e. independent of pressure, the energy conservation equation for a gaseous (g) domain is:

$$\begin{aligned} \frac{dT_g}{dt} \sum_{\text{species:j}} n_{g,j} c_{p,j}(T_g) = & \sum_{\text{reservoir:i}} Q_{\text{conv},i \rightarrow g} + \sum_{\text{species:j}} \dot{n}_{g,j,\text{in}} h_j(T_{\text{in}}) \\ & - \sum_{\text{species:j}} \dot{n}_{g,j,\text{out}} h_j(T_{\text{out}}) + \frac{dp_g}{dt} V_g \end{aligned} \quad (5.6)$$

Interactions between the reservoirs is given by mass and energy transfer. Note that during the passive cool-down of the reactor (i.e. no inlet flows), the flow direction of the gasses passing from one reservoir to another is inverse, i.e. the reactor will suck in small amounts of gas from the outlet. Reaction rates during reduction are based on equilibrium conditions for the temperature and pressure dependent reduction extent of ceria provided by Ref. [94]:

$$\left(\frac{\delta}{\delta_m - \delta}\right)^n = \left(\frac{p_{O_2}}{p^o}\right)^{-\frac{1}{2}} \exp\left(\frac{\Delta s_{th}^o}{R}\right) \exp\left(\frac{\Delta h_{\delta}^o}{RT}\right) \quad (5.7)$$

where $\delta_m = 0.35$ the maximum possible nonstoichiometry, $n = 2.31$, $\Delta s_{th}^o = 165 \text{ J/(K mol)}$ the partial molar entropy and $\Delta h_{\delta}^o = 430 \text{ kJ/mol}$ the partial molar enthalpy [94].

The required reaction rates during oxidation are fitted with an empirical equation in the form of an anti-Arrhenius equation, a methodology also used in Ref. [51]:

$$\frac{d\delta}{dt} = -K_0 \frac{n_{CO_2} + n_{H_2O}}{F} \exp\left(\frac{\Delta E_{\delta}}{RT}\right) \delta^{n_{\delta}} \quad (5.8)$$

where K_0 is a rate constant [s^{-1}] (a lumped fitting parameter), $F = 1 \text{ mol}$, ΔE_{δ} the apparent activation energy (a fitting parameter), R is the universal gas constant and n_{δ} is a fitting parameter.

The model also requires the produced $CO:H_2$ ratio $R_{CO:H_2}$. For this another empirical Arrhenius type equation is fitted:

$$R_{CO:H_2} = A_R \exp\left(\frac{-\Delta E_R}{RT}\right) \frac{n_{CO_2}}{n_{H_2O}} \quad (5.9)$$

where A_R is a lumped fitting parameter and ΔE_R the apparent activation energy (a fitting parameter). The combination of the two fitted empirical equations lead to a model response comparable to the measured CO and H_2 gas flows.

Initial estimates of a simplified model version to test the oxidation rate equations based on just G1, P1, P2 and P4 with $UA_{P1-P2} = 8W/K$, $UA_{P2-P3} = 9W/K$, $UA_{P3-I2} = 3W/K$, $K_0 = 5 \cdot 10^{-7} \text{ s}^{-1}$, $\Delta E_{\delta} = 120000$

J/mol, $n_\delta = 1$, $A_R = 500$ and $\Delta E_R = 40000$ J/mol already give promising results with the normalized root mean square error (NRMSE) fitness value of the temperature signal exceeding 80% and the fit for the H_2 signal exceeding 65% between the simulated response and measurement data over one cycle. Note that the stated values were not the results of fitted parameter estimation, but initial estimates showing the viability of the implemented empirical rate equations. Further note that the value for ΔE_δ is of the same order of magnitude as the reported activation energies for CO_2 reduction over ceria in Refs. [51, 95] and the value of ΔE_R is of the same order of magnitude as the activation energy of the water gas shift reaction.

A full parameter estimation for the complete reactor model still needs to be conducted. Ideally this is performed using whole day measurements of continuous redox cycling with changing parameter settings. Validation could then be done by comparing the modelled response to a second set of randomised cycling parameters. Unfortunately, the part of parameter estimation and model validation could not be accomplished in the framework of this thesis due to time constraints and various challenges. Some selected challenges are listed in the following paragraph.

The model is very stiff, due to the different dynamics of the various signals. E.g. the model contains signals with fast dynamics such as chemical reactions, switching valves, changing mass flows, turning the solar power input on and off but also signals with slow dynamics such as temperature changes. The model also contains highly non-linear dependencies. It is also the case that most parameters are to some extent dependent on various other parameters making the parameter estimation increasingly difficult. Another issue is that the model contains variables with different orders of magnitude, e.g. Temperature swing up to $1500^\circ C$ vs. changes in nonstoichiometry in the order of 0.001 for some domains. Solving this system of nonlinear differential equations would lead to matrices that are close to singular and the signals have to be scaled before solving.

A critical point is also the gas flows. The model is assuming continuously stirred gas volumes, an assumption that does not hold true for some small volumes experiencing high flow rates during evacuation of the reactor. Also as already mentioned above, during the cool-down phase the flow regime of the reactor is inverse, which needs to be addressed in the model.

More of a systematic measurement issue is that while the model determines gas compositions right after the reactor, the measurement of the gas composition used for parameter fitting and to validate the results in the gas analysis units is performed inside the control room. This results in a significant flow dependent measurements delay (which to some extent can be compensated in post measurement analysis) but also to a flattening of the gas composition signal due to dilution and mixing inside the over 20-meter gas lines between the reactors and the gas analysis units. This does not affect the cumulative gas yields but the temporal variations of the composition signal, which is a very important signal for the parameter estimation. Estimating the accuracy of the model is also an issue, since some gas evolution signals are basically 0 for the entire cycle apart from the oxidation step. As the model matches the 0 signal correctly for most of the cycle, the deviation in measurement signal during oxidation is not affecting the accuracy that much (i.e. there is still a near perfect fit for the rest of the cycle), and hence the automated parameter fitting algorithm will focus more on good agreement with for example the temperature signal, as there the discrepancies between model response and measured values occur over the entire cycle and thus have a higher numerical impact.

Nevertheless, to move forward with the modelling, reach reasonable validation and develop a model that is useful in the framework of this thesis, a simplified version of the model presented above has been developed and the details are explained in the following section.

5.2 Simplified Model

Figure 5.2 shows the causality diagram of a simplified version of the model consisting of only 5 domains, 4 porous RPC domains and one solid insulation domain. The five domains are identical to the respective domains of the presented model with the extended causality diagram in Fig. 5.1. The aperture for calculating the radiative losses was also kept identical at 60mm diameter. Gas flows into the reactor are modelled as flowing directly into the porous domain P1. Gas flows leaving the reactor are modelled directly leaving from P4. The insulation domain I2 is modelled as directly exposed to ambient air. As the water cooled front of the reactor (a significant energy loss) is not modelled, the power input has been adjusted based on the energy balance of chapter 2.1.2 during reduction. Note that in the real reactor the front is also a heat sink during oxidation.

Tables 5.1 to 5.6 present the summary of parameter estimated cycles using 6 selected parameter sets with different RPC mass fractions for P1 - P4 while all other parameters remain unchanged. Each set run a parameter estimation process to minimise the estimation error between the simulated model response and the measured experimental results to the same inputs. Fitted are the UA products (a lumped parameter, see Eq. 5.5) of the heat exchange between the domains. Parameter estimation was conducted in MATLAB using trust-region reflective newton algorithm with nonlinear least-squares fitting and ode45 solver. System input and measured output for parameter estimation is based on cycle 1 of Fig. 2.7. The first cycle was chosen since the algorithm estimated unfeasible initial conditions (internal temperatures) for representative cycles during regular cycling. Specifying/-fixing the initial conditions is only possible for the first cycle of a day, since it is the only time one can estimate the temperatures of the domains without a respective temperature measurement (reactor heating up from ambient temperature). Starting temperature for the model evaluation was 100°C , since the B-type thermocouples inside the reactor can only measure temper-

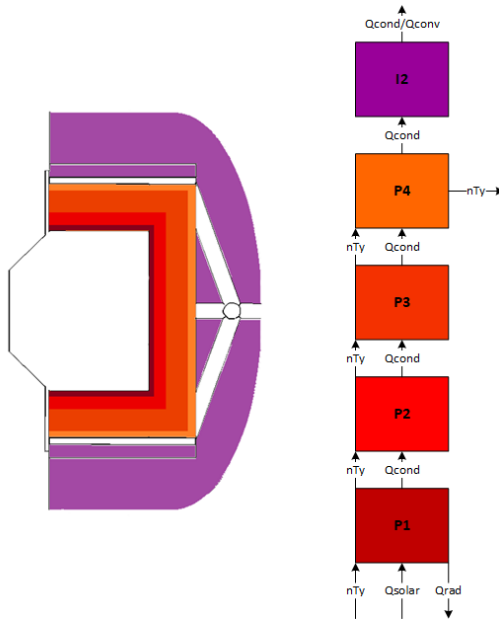


Figure 5.2: Left: Cross section of modelled reactor domains for the simplified model with coloured areas corresponding to the domains of the causality diagram. Right: Causality diagram of the simplified grey box model containing the four porous domains P (shades of red) and one insulation solid domain I (purple). The arrows between the domains indicate exchanged energy and mass flows.

atures $> 100^\circ\text{C}$. Additionally, for the first cycle the ceria nonstoichiometry $\delta_{\text{reduction-end}}$ at the end of reduction directly relates to the O_2 yield of the cycle, since the reactor was fully oxidised (all $\delta = 0$) before the start of the cycle. In continuous cycling the reactor is never fully oxidised and the initial conditions of δ in each domain are unknown. Using the first cycle for parameter estimation comes at the cost of lower agreement with the measurement curves and potentially lower fit for representative continuous cycles.

Each table 5.1 to 5.6 lists the RPC mass fractions of the RPC domains P1-P4, $T_{\text{reduction-end}}$ of each model domain, the nonstoichiometry at the end of reduction nonstoichiometry $\delta_{\text{reduction-end}}$ and $V_{\text{O}_2,\text{cycle}}$ of each RPC domain. The table also states the NRMSE fitness value of the temperature curve of P4 compared to the measured RPC temperatures as well as the total $V_{\text{O}_2,\text{cycle}}$ if the entire cavity and the relative difference of the total yield compared to the measured O_2 yield of the cycle. For comparison, the measured $T_{\text{reduction-end}} = 1400^\circ\text{C}$ and $V_{\text{O}_2,\text{cycle}} = 1.669$ L. Evidently there is a clear trade-off between optimising for increased NRMSE T evolution of P4 or $V_{\text{O}_2,\text{cycle}}$. The higher the agreement between the modelled temperature of P4 and the measured RPC temperature, the more $V_{\text{O}_2,\text{cycle}}$ is overestimated. Set 2 shows a relative difference to the measured O_2 yield of only -3.46% but with a relatively low temperature NRMSE of 77.07%. Set 3 shows a somewhat balanced result with NRMSE $T = 82.48\%$ and a relative difference to the measured $V_{\text{O}_2,\text{cycle}}$ of 21.3%. Set 3 was chosen to further analyse and use in the application case of chapter 5.3. Sets with higher NRMSE T also show higher relative difference in $V_{\text{O}_2,\text{cycle}}$. For example set 6 shows NRMSE $T = 85.04\%$ while $V_{\text{O}_2,\text{cycle}}$ is overestimated by 127.2%

Figure 5.3 shows the temperature evolution of all domains as well as the measured RPC temperature (mean value of two thermocouple measurements on the back of the top RPC sidebrick, see chapter 2.1.2) for a single cycle with parameter set 3. The slightly unsmooth signals of P1 and P2 are the result from fluctuations in solar power input (real measurement data used

| Domain | Frac. RPC [-] | $T_{\text{reduction-end}}$ [°C] | $\delta_{\text{reduction-end}}$ [-] | $V_{\text{O}_2,\text{cycle}}$ [L] |
|--------|---------------|---------------------------------|-------------------------------------|-----------------------------------|
| P1 | 0.02 | 1708.5 | 0.0402 | 0.196 |
| P2 | 0.1 | 1629.5 | 0.0214 | 0.523 |
| P3 | 0.68 | 1407.4 | 0.0035 | 0.581 |
| P4 | 0.2 | 1273.5 | 0.0009 | 0.046 |
| I2 | | 296.5 | | |
| | | | total: | 1.346 |
| | NRMSE T : | 74.48% | rel. diff.: | -19.4% |

Table 5.1: Parameter set 1. Results after parameter estimation of the UA products for the heat exchange between the domains.

| Domain | Frac. RPC [-] | $T_{\text{reduction-end}}$ [°C] | $\delta_{\text{reduction-end}}$ [-] | $V_{\text{O}_2,\text{cycle}}$ [L] |
|--------|---------------|---------------------------------|-------------------------------------|-----------------------------------|
| P1 | 0.05 | 1702.9 | 0.0360 | 0.440 |
| P2 | 0.1 | 1631.7 | 0.0213 | 0.520 |
| P3 | 0.65 | 1415.3 | 0.0038 | 0.603 |
| P4 | 0.2 | 1279.1 | 0.0010 | 0.049 |
| I2 | | 238.6 | | |
| | | | total: | 1.612 |
| | NRMSE T : | 77.07% | rel. diff.: | -3.5% |

Table 5.2: Parameter set 2. Results after parameter estimation of the UA products for the heat exchange between the domains.

| Domain | Frac. RPC [-] | $T_{\text{reduction-end}}$ [°C] | $\delta_{\text{reduction-end}}$ [-] | $V_{\text{O}_2,\text{cycle}}$ [L] |
|--------|---------------|---------------------------------|-------------------------------------|-----------------------------------|
| P1 | 0.02 | 1667.8 | 0.0314 | 0.153 |
| P2 | 0.15 | 1643.9 | 0.0227 | 0.831 |
| P3 | 0.58 | 1485.8 | 0.0067 | 0.949 |
| P4 | 0.25 | 1318.4 | 0.0015 | 0.092 |
| I2 | | 113.1 | | |
| | | | total: | 2.025 |
| | NRMSE T : | 82.48% | rel. diff.: | 21.3% |

Table 5.3: Parameter set 3. Results after parameter estimation of the UA products for the heat exchange between the domains.

| Domain | Frac. RPC [-] | $T_{\text{reduction-end}}$ [°C] | $\delta_{\text{reduction-end}}$ [-] | $V_{\text{O}_2,\text{cycle}}$ [L] |
|--------|---------------|---------------------------------|-------------------------------------|-----------------------------------|
| P1 | 0.02 | 1671.2 | 0.0320 | 0.156 |
| P2 | 0.12 | 1636.9 | 0.0220 | 0.645 |
| P3 | 0.61 | 1532.2 | 0.0095 | 1.415 |
| P4 | 0.25 | 1313.7 | 0.0014 | 0.085 |
| I2 | | 127.8 | | |
| | | | total: | 2.301 |
| | NRMSE T : | 82.61% | rel. diff.: | 37.9% |

Table 5.4: Parameter set 4. Results after parameter estimation of the UA products for the heat exchange between the domains.

| Domain | Frac. RPC [-] | $T_{\text{reduction-end}}$ [°C] | $\delta_{\text{reduction-end}}$ [-] | $V_{\text{O}_2,\text{cycle}}$ [L] |
|--------|---------------|---------------------------------|-------------------------------------|-----------------------------------|
| P1 | 0.02 | 1667.4 | 0.0307 | 0.150 |
| P2 | 0.2 | 1652.9 | 0.0232 | 1.133 |
| P3 | 0.58 | 1600.8 | 0.0151 | 2.138 |
| P4 | 0.2 | 1323.1 | 0.0015 | 0.073 |
| I2 | | 86.3 | | |
| | | | total: | 3.495 |
| | NRMSE T : | 84.81% | rel. diff.: | 109.3% |

Table 5.5: Parameter set 5. Results after parameter estimation of the UA products for the heat exchange between the domains.

| Domain | Frac. RPC [-] | $T_{\text{reduction-end}}$ [°C] | $\delta_{\text{reduction-end}}$ [-] | $V_{\text{O}_2,\text{cycle}}$ [L] |
|--------|---------------|---------------------------------|-------------------------------------|-----------------------------------|
| P1 | 0.02 | 1666.3 | 0.0304 | 0.148 |
| P2 | 0.15 | 1655.9 | 0.0240 | 0.879 |
| P3 | 0.63 | 1624.1 | 0.0175 | 2.692 |
| P4 | 0.2 | 1324.7 | 0.0015 | 0.073 |
| I2 | | 62.5 | | |
| | | | total: | 3.793 |
| | NRMSE T : | 85.04% | rel. diff.: | 127.2% |

Table 5.6: Parameter set 6. Results after parameter estimation of the UA products for the heat exchange between the domains.

for simulation). This effect is the highest in P1 (directly radiated) but can not be seen any more in P3 and P4. As expected, the highest temperature signal during reduction is P1, followed by P2 close to the centre of the cavity. Interestingly P3 shows the highest temperature in the cool-down and oxidation phases of the cycles. This can be explained by the radiative losses of P1 through the reactor aperture, which cool down P1 more rapidly. P2 follows P1 analogously as P1 is a very thin layer. The temperature profile from the insulation domain remains flatter than the RPC domains. This can be explained as it is in contact with the surroundings at constant temperature, has a different specific heat capacity than the RPC and the partial air gap between RPC and insulation adding to a lower heat exchange. The initial conditions of 100°C are over estimated as they are based on the measurements of one side of the insulation (next to the RPC) and hence overestimate the mean temperature at the start. At the same time the initial RPC temperatures are underestimated. However, given the high heating rates within the RPC domains, this effect is limited. While generally following the profile of the measured temperature, $T_{\text{reduction-end}}$ of P4 is lower than the measured value and hence underestimating the peak temperature (P4 $T_{\text{reduction-end}} = 1318.4^{\circ}\text{C}$ compared to the measured 1400°C). Worth noticing is also the slight shift in time of the peak temperatures (e.g. P4 peaks later than P1) due to the slower dynamics of temperature changes through conductive heat transfer.

Given the simplifications, assumptions and limits of this simplified model, it is clear that exact agreement with the measurements is unlikely. Leaving away the other solid domains compared to Fig. 5.1, also removed the heat losses over those domains from the model, hence changes the temperature profiles of the remaining domains. Especially leaving away the water cooled aluminium front has a big impact. This was partially addressed by adjusting the radiative input power, but can not be compensated completely, especially as cooling also occurs during oxidation. Leaving away the gas volumes (e.g. G1) has an influence on the gas composition entering the porous domains,

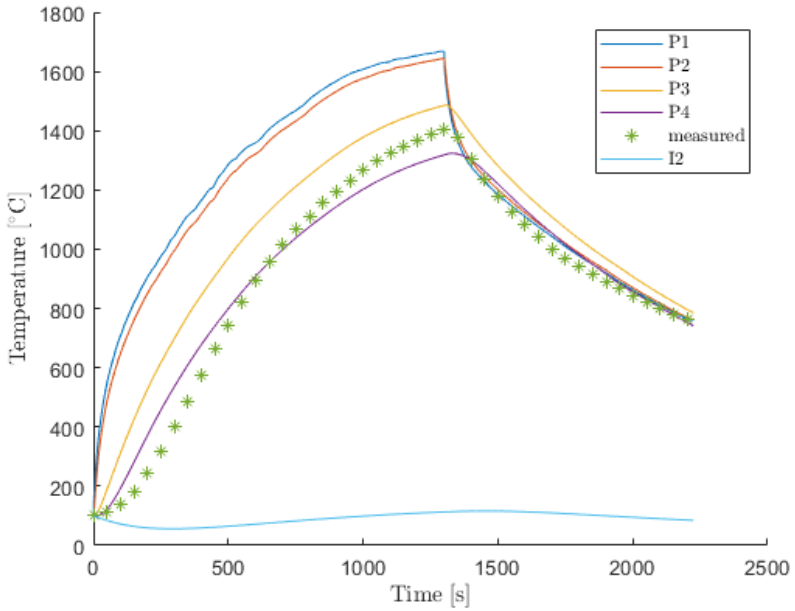


Figure 5.3: Temporal variation of temperatures of model domains P1, P2, P3, P4, I2 and measured RPC temperature for 1 cycle. For increased visibility only every 50th measured data point is plotted. Model based on parameter set 3.

as the mixing in the volume before P1 now does not occur. The gas volumes also play a role in the heat exchange with the removed parts such as the front insulation, the cooled front, or the window.

The real reactor will show a continuous temperature gradient within the RPC. Modelling this with only 4 domains at uniform temperature will naturally differ from the reality. The model also assumes axial symmetry of the temperature profiles. However, due to convective effects within the reactor the top of the reactor is always hotter than the bottom and there might be a temperature gradient between the front and back of the reactor parallel to the main axis as well, which is not addressed in this model. The exact locations of the temperature measurements are essential and explain the discrepancies with the modelled domains at averaged and uniform temperature. Note that the positioning of the temperature measurement is less critical for running physical experiments as the temperature there is mainly taken as a reference for the cycling control.

Since the O_2 yield over the cycle is dependent on the temperature via the temperature dependence of the ceria nonstoichiometry (see Eq. 5.7), the change in temperature profile has a direct influence on the yield.

In the real reactor the apparent reactor temperature used for calculating the radiative heat losses is only reached on the surface of the RPC while in the model this temperature is taken for the entirety of P1. The temperature of P1 is hence overestimated, leaving to a higher nonstoichiometry and hence overestimated O_2 yield in P1. This effect has an especially high influence on the modelled yield, as the changes in δ are exponentially higher with higher temperatures. The effect can be decreased by decreasing the RPC mass fraction of P1, but will in turn also decrease the residence time of the gas within the domain, which then could break the assumption of gas outlet temperature of the domain matching the solid RPC temperature. The assumption of the gas volumes (also within the RPC domain) being perfectly stirred (i.e. uniform composition in the entire volume) is also further from the reality for smaller volumes with high through flow.

Since the temperature of P4 is used to represent the measured tempera-

ture at the back of the RPC and the temperature generally increases towards the center of the cavity, the temperature of P4 is underestimated (uniform temperature within entire P4 and not only on the outside) if they would be in perfect agreement. This effect could be decreased by decreasing the RPC mass fraction of P4, but at the cost of at the same time increasing the fractions of P2 and or P3. Increasing the amount of porous RPC domains could address this issue. It is also worth noting that since P4 is the coldest RPC domain it also has the smallest $\delta_{\text{reduction-end}}$ and hence typically does not cocontribute much to the total $V_{\text{O}_2, \text{cycle}}$.

A remaining uncertainty is the temperature measurement itself. Since the exact position of the used thermocouples is unknown when the reactor is closed up and in operation (RPC parts can slightly shift during operation) and the exact positioning of the measurement tip is essential (e.g. touching the RPC directly or measuring the temperature in the gas gap behind). Unfortunately this uncertainty can not be avoided.

5.3 Model Application — Multi Reactor System

The following section shows a possible application of such a grey box model. Modelled is the cycling of multiple reactors by making continuous use of the incoming solar radiation. Reduction was modelled until the reactor reaches $T_{\text{reduction-end}}$. The reactor is then cooling down and performing the oxidation until all other reactors come off-sun and the cycle can start again. The modelling assumes instantaneous refocussing of the optical system to the next reactor, i.e. no delay due to turning of secondary mirror. Input power, reactor pressures and gas flows are based on measured cycles. The simplified model used for this study is based on parameter set 3. $T_{\text{reduction-end}}$ is chosen as 1319°C according to parameter fitting (fitted for cycles with $T_{\text{red-end}} = 1400^\circ\text{C}$). $P_{\text{solar}} = 4.8$ kW and reactor pressure was lowered to 4.5 mbars during reduction and ambient pressure during cool-down and oxidation. Without modelling the oxidation reaction, complete oxidation

was assumed at the end of every cycle.

Figure 5.4 shows the P4 temperature evolutions of a system with 2 reactors using the solar input at all times. The first heat up takes the longest as the reactor was heated up from ambient temperature (displayed temperature curve starting at 100°C). Cycling time stabilises (no further decrease in $\Delta t_{\text{reduction}}$) after the 3rd cycle of reactor 2 with identical and repeatable cycles after that. For stable cycling $\Delta t_{\text{reduction}} = \Delta t_{\text{cool-down}} + \Delta t_{\text{oxidation}} = 1021.1$ s, resulting in a cycle time of 2042.2 s. As expected, the system balances the two reactors operating side by side by matching reduction time with cool-down plus oxidation times. The temperature swing is 614.7°C for P4 and 988.3°C for P1, respectively. $V_{\text{O}_2, \text{cycle}}$ of one cycle is 2.07 L resulting in $\dot{V}_{\text{O}_2, \text{cycle}} = 3.65$ L/h of one reactor and $\dot{V}_{\text{O}_2, \text{system}} = 7.31$ L/h of the two reactor system. Assuming full oxidation in every cycle this would lead to a syngas production of 14.61 L/h in the two reactor system. Note that in reality the reactors are usually not fully oxidised after every cycle during production. The calculated syngas production rate can serve as an estimated upper boundary. Also note that the numerical result is highly dependent on P_{solar} , e.g. higher P_{solar} would reduce the cycle time and hence increase production rate.

Figure 5.5 shows the P4 temperature evolutions of a system with 3 reactors using the solar input at all times under the same conditions as Fig. 5.4. Analogous to Fig. 5.4 the first heat up takes longer as the reactor was heated up from ambient temperature (displayed temperature curve starting at 100°C). An obvious difference to the two reactor system of Fig. 5.5, is the higher temperature swing caused by the longer cycles. Cycling time stabilises (no further decrease in $\Delta t_{\text{reduction}}$) after the 3rd cycle of reactor 1 with identical and repeatable cycles after that. For stable cycling $\Delta t_{\text{reduction}} = 1198.4$ s and $\Delta t_{\text{cool-down}} + \Delta t_{\text{oxidation}} = 2397.0$ s, resulting in a cycle time of 3594.8 s. The higher $\Delta t_{\text{reduction}}$ compared to the two reactor system is explained with the higher temperature swing of the three reactor system,

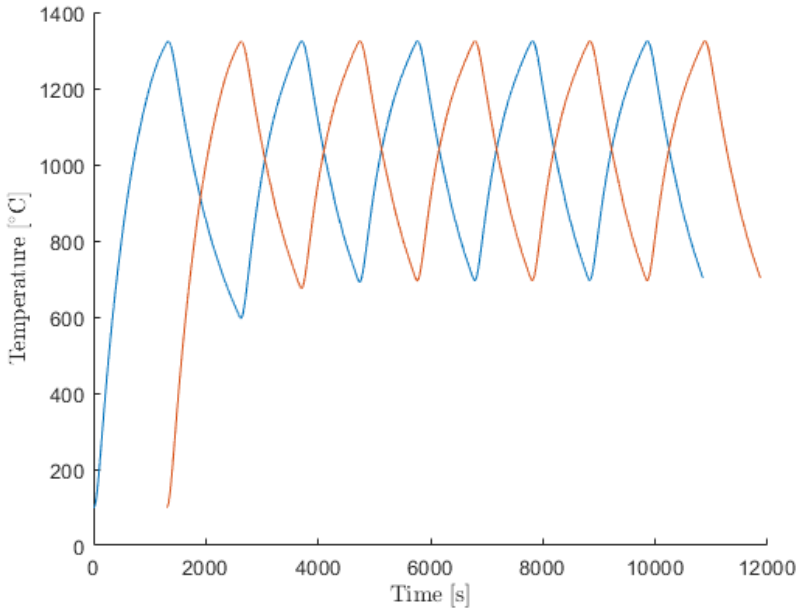


Figure 5.4: Temporal variation of temperatures of the RPC domain P4 for a two reactor system making continuous use of the incoming solar power. Model based on parameter set 3. $P_{\text{solar}} = 4.8$ kW. Blue and red represent the two modelled reactors.

i.e. the reduction step starts at lower temperatures. As expected, the system balances the three reactors operating in parallel by performing the cool-down plus oxidation step twice as long as the reduction step. The temperature swing is 976.4°C for P4 and 1309.1°C for P1, respectively. $V_{\text{O}_2, \text{cycle}}$ is 2.06 L, which is nearly identical to that of the two reactor system. However, the resulting $\dot{V}_{\text{O}_2, \text{cycle}} = 1.54$ L/h of one reactor is expectedly much lower given the longer cycle time. For the entire three reactor system $\dot{V}_{\text{O}_2, \text{system}} = 4.63$ L/h. Assuming full oxidation in every cycle this would lead to a syngas production of 9.27 L/h in the three reactor system. This is 36.6% lower than the hourly production rate of the two reactor system. Given that both systems use P_{solar} continuously, with always one reactor performing the reduction step at any given time, this also implies that the three reactor systems has a 36.6% lower $\eta_{\text{solar-to-syngas}}$ compared to the two reactor system. The absolute value of $\eta_{\text{solar-to-syngas}}$ depends on the syngas composition. These results make the three reactor system unreasonable to be implemented with the investigated reactors for the modelled P_{solar} , as the two reactor system would outperformed it in both efficiency as well as production rate. Based on the above analysis of the two and three reactor system, it can also be concluded that a system with four or even higher number of reactors (same reactor size and P_{solar}) would perform even worse. Additionally, a two reactor system, such as the one implemented in this thesis, is of course less complex to implement and much simpler to control than a three reactor system.

Figure 5.6 shows the P4 temperature evolutions of the system with 2 reactors as in Fig. 5.4 but for a higher power input $P_{\text{solar}} = 6.2$ kW instead of 4.8 kW. As expected, the system again balances the two reactors operating side by side by matching reduction time with cool-down plus oxidation times. Cycling time stabilises (no further decrease in $\Delta t_{\text{reduction}}$) after the 5th cycle of reactor 1 with identical and repeatable cycles after that. Compared to Fig. 5.4 the cycle times are now much shorter at $\Delta t_{\text{cycle}} = 950$ s for the full cycle ($\Delta t_{\text{reduction}} = 475.2$ s). The temperature swing is only 305.8°C

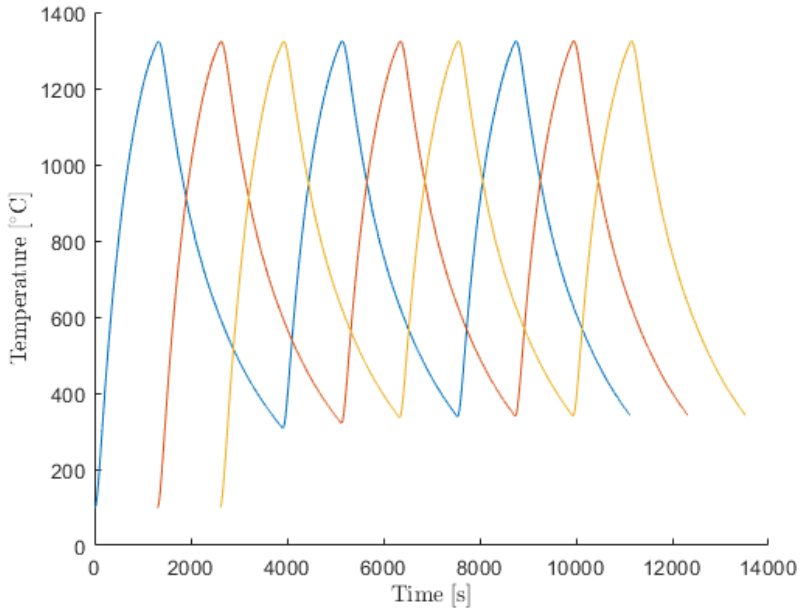


Figure 5.5: Temporal variation of temperatures of the RPC domain P4 for a three reactor system making continuous use of the incoming solar power. Model based on parameter set 3. $P_{\text{solar}} = 4.8$ kW. Blue, red and yellow represent the three modelled reactors.

for P4 and 761.7°C for P1, respectively with P4 cycling above 1000°C . For that temperature range oxidation kinetics would not be favourable and the reactor will not be fully oxidising, in fact it might barely produce syngas at all. In order for production to be feasible at the power level of 6.2 kW one would have to move the solar power away from the reactors entirely to allow them to cool down to temperatures more favourable for the oxidation reactions (Eq. 1.2 and Eq. 1.3). Since P_{solar} is then not used continuously anymore, running the system with three reactors might become a resonable option again. So the optimum number of reactors to make continuous use of the incoming solar radiation depends on the particular reactor type but also on the power levels the system is expected to perform. One interesting option to further investigate would be to generally run the system with two reactors but switch to operating three reactors as soon as it becomes viable.

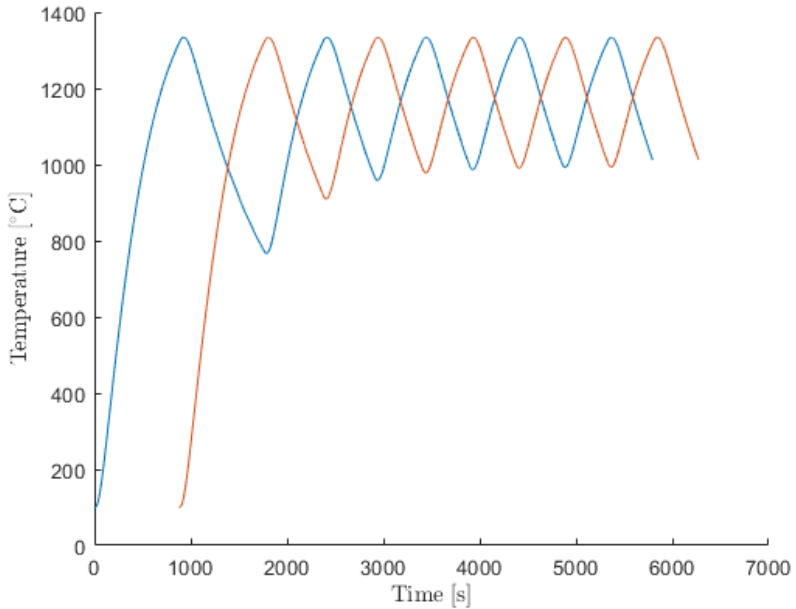


Figure 5.6: Temporal variation of temperatures of the RPC domain P4 for a two reactor system making continuous use of the incoming solar power. Model based on parameter set 3. $P_{\text{solar}} = 6.2$ kW. Blue and red represent the two modelled reactors.

5.4 Summary and Conclusions

This chapter described the key equations for setting up a dynamic grey box model of the solar redox reactor. Conducting parameter estimations on a simplified model for different RPC domain sizes shows a clear trade-off between reaching high temperature NRMSE agreement between model and measured data and agreement of cumulative O₂ yield. The yield being more overestimated the higher the NRMSE temperature agreement. Applying the simplified model to a two reactor and a three reactor system, allows to compare the performance of the two systems and discuss the viability of installing a third reactor depending on P_{solar} . A three reactor system is not a viable option for $P_{\text{solar}} = 4.8$ kW but could become viable for higher P_{solar} .

SUMMARY, OUTLOOK AND RESEARCH RECOMMENDATIONS

6.1 Summary

This thesis described the implementation and demonstration of the thermochemical process chain from sunlight and air to liquid fuels, discussing the details and characteristics of the implemented fuel system and presenting fully automated experimental runs for the production of solar methanol. The system serially integrates three thermochemical process units: 1) The DAC unit, capturing CO_2 and H_2O from ambient air via adsorption/desorption cycles based on temperature and pressure swing. 2) The solar redox unit, using concentrated sunlight to run in parallel two directly radiated solar reactors performing the ceria based redox cycles to form H_2 and CO . And 3) the GTL unit to finally transform the syngas to methanol or hydrocarbon fuels. The characteristic redox cycle of the solar redox unit is operated under a temperature/pressure-swing mode, consisting of three phases: 1) The

reduction phase, during which the solar reactor is heated with concentrated sunlight up to the desired reduction end temperature of up to 1500°C to release O₂ from CeO₂, assisted through decreased total pressure by a vacuum pump and an Ar sweep gas flow. 2) A cool-down phase under atmospheric pressure during which the solar reactor, re-pressurized by injecting CO₂, cools down to the oxidation start temperature. 3) The oxidation phase, during which CO₂ and H₂O are co-injected into the reactor's cavity and react with the reduced ceria to form syngas.

Integrating the three thermochemical units and producing methanol, demonstrates the technical viability of the thermochemical process chain for converting sunlight and ambient air to drop-in fuels and advance the technological readiness and its industrial implementation. Continuous on-sun cycling under real field conditions over the entire day demonstrates the robustness and stability of the solar redox unit and the analysis of characteristic cycles shows the ability to produce syngas with composition for downstream methanol synthesis as well as FT-synthesis. An 18 day 152 consecutive cycles production campaign led to the first demonstration of the production of methanol via the thermochemical pathway from sunlight and air. An in-depth experimental parametric study of the solar reactor operation shows how the syngas product quality can be tailored for Fischer-Tropsch synthesis by selecting adequate oxidation conditions, eliminating the need for additional downstream refining of the syngas. The study shows a clear trade-off between optimising for fuel yield, efficiency or conversion. A challenging aspect when optimising is the fact that the highest values for most parameters such as $\eta_{\text{solar-to-syngas}}$ or V_{syngas} lie on the boarder of possible parameter combinations reaching the target $R_{\text{H}_2:\text{CO}}$ in the syngas or not reaching the target anymore. The results of this parametric study were compared to separate CO₂ and H₂O splitting cycles targeting high molar conversion. To address the issue of finding optimal process parameters a control scheme for optimisation was incorporated in the automation of the solar fuel system. A solar run of fully-automated consecutive redox cycles

demonstrates that the implemented control scheme for the optimisation of the solar fuel system works and indeed leads to higher performance values.

The stable and successful outdoor operation of the solar fuel system under intermittent solar irradiation convincingly demonstrates the technical viability of the thermochemical process chain for converting sunlight and ambient air to drop-in fuels and advances the technological readiness.

6.2 Outlook and Research Recommendations

While parts of the process chain contain technologies that are already further developed and industrially implemented on large scale (e.g. DAC and GTL processes) the key part of the process chain with the highest improvement potential (partially because the technology is in an earlier research stadium and less established) is the solar redox unit. This chapter hence focusses on the research recommendations mainly of the solar redox unit, but also system integration and the pathway to bring solar fuels into the market. The research should continue on all scales from fundamental material research all the way to system integration and economic aspects. The main goal for most improvements is ultimately to increase η_{system} in order to decrease the final fuel price and make the technology viable for large scale deployment.

6.2.1 Improvements on the Setup and Reactor Design

The study in this thesis focussed mostly on the influence of the operational parameters of the solar reactor. However, system performance can be further improved by physical modifications in the reactor design or the system setup.

Improvements on the Ceramic Material and Structure

The RPC could be improved both on the material and the morphology side. Although pure ceria so far is still the benchmark material and typi-

cally outperforming newly developed and investigated redox alternatives on long-term cycling stability and structural integrity, material research should continue on screening for and testing potential alternative candidates such as doped ceria or perovskites. The goal would be to find a material that can reach higher reduction extent for the same temperatures or comparable reduction extent but at lower temperatures, while keeping similar or better oxidation characteristics and also demonstrate long term cyclability and chemical stability.

On the morphology side, the RPC structure can be further improved or replaced by an alternative shape for example with a porosity gradient for better volumetric absorption of radiation and more uniform heating. Recent developments in the design and fabrication of ordered structures and 3D-printed alternative structures show promising results [86, 87] and this research should be continued both on the numerical modelling and applied testing side. Designing and manufacturing not only small samples but whole cavities depending on the distribution and direction of the solar input opens new possibilities. During this research also the mechanical stability of the designed cavity should be considered, as making the directly radiated ceria structure more robust over long-term cycling (i.e. less structural damage to the cavity over time) is important, as in an industrial application the need to replace ceria elements should be avoided or minimised and where possible replaced material should be recycled.

Improvements of the Reactor Design

The reactor design itself could also be improved. The flow regime inside the reactor could most definitely be improved by changing the position and shape of the steam inlet into the reactor. However, this would need careful analysis with a detailed fluid flow model inside the entire reactor in order to optimise it. The size of the aperture in relation to the size of the cavity is another parameter that could be investigated e.g. with a model as presented in [81]. The aperture size relative to P_{solar} is one of the reasons why the reactors

installed and discussed in this thesis show lower $\eta_{\text{solar-to-fuel}}$ compared to e.g. the reactor of Ref. [40]. While increasing the solar power rating from about 4 kW to about 5 kW the aperture increased from 40 mm to 60 mm diameter, increasing also the radiative losses. As there is a trade-off between higher $\eta_{\text{solar-to-fuel}}$ for a smaller aperture (i.e. lower re-radiation losses) and higher η_{optical} for a larger aperture (need for higher concentration ratios in smaller aperture), finding the optimal aperture size would need careful analysis of both effects in parallel.

Heat Recovery in the Solar Reactor

To boost $\eta_{\text{solar redox unit}}$ a key research need is the implementation of heat recovery (see also efficiency discussion in chapter 2.5). Recovery of the heat rejected during the temperature swings between the redox cycles is one of the most significant ways of increasing $\eta_{\text{solar redox unit}}$. Recent work using a large amount of gas to recover some of the heat during the cool-down phase and store it in a thermal energy storage to be used again to heat up the reactor in the coming reduction phase [91] investigates this topic. This comes with the further benefit of shortening $\Delta t_{\text{cool-down}}$ and $\Delta t_{\text{reduction}}$ and hence Δt_{cycle} , which increases fuel yield per time. However, further investigations and technical implementations are needed. Since heat recovery is absolutely key also other alternative options of heat recovery should be investigated (e.g. [69]). For a multi-reactor system, one option is to use the recovered heat directly in one of the other reactors, hence avoiding the losses of adding a separate heat storage. Alternatively, the extracted heat could be used to drive the DAC unit, generate steam, preheat gases or (if used to generate electricity first) run the vacuum pumps, compressors and auxiliary systems.

Improvements of Auxiliary Systems

Looking at potential improvements for future designs of similar fuel systems, one of the challenges is the large distance between the reactors and the auxiliary systems. In the current setup, there is between 8 and 10 m tubing

between the reactors and the vacuum pump at the bottom of the solar dish. Between the reactors and the gas analysis unit this distance is over 20m. This means that when evacuating a reactor also the KF25 tubing between the reactor and the vacuum pump are evacuated and hence have to be repressurised again after the reduction step. The piping between the pump and the reactor also affects the achievable vacuum pressure in the reactors due to friction. So apart from upgrading to a more powerful vacuum pump, bringing the pump closer to the reactor outlet and therefore reducing the evacuated gas volume after the reactor, would decrease the achievable vacuum pressure during reduction and decrease the amount of non-reacting gas (Ar or CO₂ to repressurise the volume after the reactor) in the product line.

Also bringing the gas analysis units closer to the reactor would help decreasing the flow dependent delay of the measured gas analysis signal to what is occurring in the reactor. Through careful post processing of the measurement data, parts of this delay can be adjusted retrospectively. The long distance between the reactors and the gas analysis units also lead to some flattening of the gas composition curve due to diffusion and mixing within the gas travelling from the reactors to the gas analysis units.

Dealing with Condensation in the System

An issue that arose and should be addressed in future reactor designs, is the condensation of water in the system when adding H₂O-splitting cycles. In the current reactor design the inlet cone between the aperture and the window (see Fig. 2.3) is water cooled. During oxidation the H₂O entering the reactor condenses on the cone and fills up the cone to the level of the aperture opening. A possible way to address this issue is to change the cooling in the front from water to oil at above 100°C . Additionally, unconverted H₂O condenses in the tubing after the reactor and stays in the system until the next reduction phase. During the reduction phase the condensed water is partially evaporated again and removed through the vacuum pump. This evaporation leads to higher p_{reactor} during reduction. As H₂O accumulates

in the system over a measurement day, this effect increases with every cycle. Condensation in the gas volume after the reactor is also the reason why the reactor can not be repressurised with H_2O after the reduction step, as due to the condensation in the tubing the reactor can not be brought up to ambient pressure in time for the oxidation start. A possible idea to address this issue would be to close off the reactor at the outlet after reduction until the start of the oxidation. Like this the reactor could be repressurised with H_2O , as the H_2O would remain in the hot zone. However, this would imply the deployment and possibly development of a high temperature valve right at the reactor outlet.

Another issue is, that in order for the vacuum pump to deal with the H_2O in the pumped gas, the pump pulls a large amount of ballast gas (ambient air) into the pump, diluting the gasses from the reactor to the point that the O_2 content can not be measured anymore in the gas stream after the vacuum pump. The liquid water in the system, combined with the suction of the vacuum pump can also transport unwanted particles such as ceria dust or broken of pieces of RPC down the lines, which have to be filtered out before the vacuum pump. Of course any addition of filters further decreases the achievable vacuum pressure in the reactor.

Improvements of the Optical System

Improvements of the solar optics for the installed concentrating dish system has already been analysed in detail, with potential to improve η_{optical} from 59.6% to 82% [79]. Apart from the optical system itself, the alignment of the solar reactors and the calorimeter with the optical system is critical. Optical misalignment of the reactors obviously decrease their efficiency, while misalignment of the calorimeter itself or the position relative to the reactors, can lead to an overestimation of P_{solar} and hence underestimation of $\eta_{\text{solar-to-syngas}}$. The current system of aligning the different instruments is based on installed lasers and assumptions that certain structural parts of the primary and secondary reflector kept their exact position relative to each other since the very first instalment. For a potential next generation optical

system, it would be important to include a concept of alignment from the beginning of construction based on immovable fixed points.

Improvements of the DAC unit

Although the main focus should be set on the improvement of the solar redox unit, also the technology of the DAC unit should be further developed. As the DAC process is highly energy intensive, gains in the DAC efficiency (e.g. through improvements on the sorbent material or by finding ways to decrease the needed energy input of the adsorption/desorption cycle) would increase η_{system} . Decreasing the energy demand for the DAC unit, even without improvement of η_{DAC} , would free recovered heat available for other uses within the system and hence still decrease η_{system} , e.g. through decreasing $\eta_{\text{solar-to-syngas}}$ by increased preheating.

Improvements of the GTL unit

For the GTL unit (by far the most established technology of the process chain) the key challenges are the integration with the rest of the process chain. Industrial GTL processes usually tailor/mix the syngas to the optimal composition for the used catalyst and target fuel. When integrating the GTL with the solar redox unit however, there might be cases where it would overall be beneficial (e.g. as it might improve $\eta_{\text{solar redox unit}}$) to run the GTL unit with less optimal syngas composition. The challenge there would then be to optimise the GTL process based on the provided syngas composition, for example with a higher than usual content of CO_2 left in the syngas.

6.2.2 Operation of the Fuel System

Changing Vacuum Pump Operation

Apart from simply decreasing the vacuum pressure during reduction as mentioned before, the pressure could also only be reduced towards the end

of the reduction step with the potential of decreasing Q_{pump} and therefore increasing $\eta_{\text{solar-to-syngas}}$. However, this option only brings improvement if the issue of condensate accumulation downstream of the reactor is addressed first. For the current setup, the cycle performance when running the pump during the entire reduction step and reaching a lower p_{reactor} is higher, compared to only running the pump towards the end of reduction, but not reaching the same vacuum pressure due to the condensed water in the system, i.e. the effect of the higher fuel yield due to the lower p_{reactor} dominates the effect of the reduced Q_{pump} .

Introducing Varying Oxidation Flows

During this study and previous studies with a similar reactor concept (e.g. Refs. [40, 20]) the gas flows into the reactors have been kept constant during oxidation. While this does give promising results, it also brings potential issues. One issue that was discussed in chapter 3.3.2 is that due to the removal of condensed and unreacted H_2O , the outlet flow of the reactor is not constant but decreases during oxidation. Depending on the CO_2 flow rates, this leads to accumulation of high quality syngas in the reactor that is not leaving the reactor during the oxidation as the total flow is too low. In chapter 3.3.2 this was addressed by introducing a flush flow of CO_2 towards the end of oxidation. Another option would be to gradually change the gas flows into the reactor during the oxidation. One could for example flow more CO_2 at temperatures where CO_2 -splitting is thermodynamically favourable and more H_2O where H_2O -splitting is more favourable, with the potential to increase conversion of both CO_2 and H_2O . One could potentially even decouple $T_{\text{oxidation-start}}$ for CO_2 and H_2O , respectively.

The inlet flows could even be directly coupled to a feedback control system with the outlet gas analysis units. For this however, the gas analysis would have to take place much closer to the reactor outlet to minimise the delay of measurement and allow for feedback within the response time of the system. Implementation of this direct feedback loop during the oxidation might be infeasible on the presented system due to the comparably big gas

volumes between the reactors and gas analysis units, but could be investigated on a model (e.g. the one developed in chapter 5) or upscaled system.

6.2.3 System Integration

Evidently, the coupling of the intermittent solar redox process with the round-the-clock DAC and GTL processes complicates the integration of the three units because of the temporal mismatch of both mass and energy flow rates to/from each unit. Further complication arises from the different operational temperatures and pressures of each unit. In terms of the mass flows, the incorporation of buffer tanks upstream and downstream of the solar redox unit to intermediately store H_2O and CO_2 (upstream) and syngas (downstream), as applied in the described setup, is technically simple and scalable, and therefore the preferred approach as compared to running the entire system only during sunshine hours with oversized (and more expensive) DAC and GTL units. Given the non-continuous cyclic production in the DAC unit and the solar redox unit and the continuous syngas flow needed in the GTL reactor, at least minimal buffer tanks would have to be implemented anyway. The sizing of these buffer tanks for an industrial-scale plant is a function of the mass flow rates of reactants/products to/from the solar redox unit.

In terms of the energy flows, the thermal management mentioned above as a measure to maximize η_{system} would be practicable by heat exchange via heat transfer fluids between the endothermic DAC process (heat sink at below 100°C), the exothermic GTL process (heat source at above 200°C) and the solar redox unit (heat source at between 600 and 1500°C). However, for a 24 h continuous production, heat exchange with the solar-driven process would only be possible if heat is stored temporarily, for example in thermocline heat storage tanks [96]. Thermal management of the combined process chain is a key research need for further upscaling and industrial implementation.

Alternative Solar Redox Unit Configuration

An alternative solar redox unit configuration, which would potentially simplify its integration, consists of replacing the solar reactor at the focus of the solar concentrator with a solar receiver that delivers high-temperature heat via a heat transfer fluid to a thermal storage tank, which in turn continuously delivers heat to a (non-solar) redox reactor. Such a reactor, or array of reactors, would operate round-the-clock similar to the power block of a CSP plant with thermal storage [8], and therefore would be simpler to integrate with the DAC and GTL units, both in terms of the mass and energy flow rates. Thermal management would be applicable by heat exchange with the redox reactor as well. Furthermore, this configuration would facilitate the operation of the oxidation step at higher, thermodynamically more favourable pressures to obtain pressurized syngas, thereby minimising or even eliminating the compression work before the GTL. A key advantage of this configuration is that the redox reactor is not exposed to the harsh conditions of concentrated solar irradiation. This should increase the longevity of the redox material inside the reactor. Note that the reactor geometry and optimal ceria structure would also be different.

When thinking about reconfiguring the solar redox unit it, would also be an option to investigate the possibility to add a third or even more reactors with reactor size adjusted to always have one reactor on sun performing the reduction step and making optimal use of the incoming solar power. The optimal number of reactors depends on the size and design of the reactors as well as on the solar power input. See also discussion in chapter 5.3. It could even be an option to have one or more reactors on standby and only use it above a certain P_{solar} , i.e. constantly adjust the number of reactors running depending on the solar conditions.

6.2.4 Advances in System and Reactor Modelling

As discussed in chapter 5 the developed dynamic grey box reactor model still needs careful parameter fitting and model validation. In order to accomplish this, there are a couple of open challenges that need to be addressed (see chapter 5). If needed, the current reactor model could also be extended by adding additional domains or by simply dividing existing domains into multiple smaller domains. For example, increasing the number of RPC domains modelled inside the reactor, might help getting a better agreement with the measured temperature curves and could be an option to improve the model accuracy. However, increasing the amount of modelled domains of course comes with the drawback of an increase also in computational time.

Once the reactor model is fully functional, it can be used as an essential building block in modelling the entire solar fuel system. For this, also the other subsystems such as the DAC unit, the GTL unit, the optical concentrating system, the buffer storage tanks and various auxiliary systems have to be modelled as well. Also for modelling those systems, grey box models would be an excellent choice given the shorter computational time compared to for example a complete CFD model and the easy integration as building block into a combined model. Since a model of the entire fuel system would predominantly be used to investigate topics on a systems level, details of internal states are of less interest as long as the model response corresponds reasonably well with measured outputs of the modelled subsystem. For some subsystems where there is a vast amount of data available even a black box model approach could be a viable option.

The system model could be used to investigate research needs such as heat recuperation and integration across the different units of the fuel system, dimensioning of appropriate storage buffer tanks, identifying bottlenecks in the production chain and optimising energy and mass flows throughout the system. It can also be used to simulate new control strategies or to test suggested improvements to the system before they are physically implemented.

6.2.5 Scale-up to Industrial Size Plant

One of the next challenges to bring the technology closer to market is upscaling. Ref. [20] discusses an upscaling attempt with a 50 kW reactor mounted on a solar tower. However, for industrial production the reactor concept would have to be up scaled even further. Parts of the challenges have already been discussed in sections above, with most improvement suggestions for the current system also applicable and even more important for an up-scaled process chain. This section summarises how a potential industrial size plant could look like. Material in this section is partially extracted from Ref. [97].

As solar concentrating system a multitude of solar dishes or a heliostat field focusing on a solar tower could be used for scaling up and concentrating the DNI to the solar flux concentration required ($C > 2000$ suns) [8]. Notably, the optical components for concentrating the DNI, e.g. solar dishes and heliostat fields, are already established for CSP plants, though for lower values of solar flux concentration, but there are substantial technological spill overs from solar thermal electricity to solar thermochemical fuels. Although technically possible, as demonstrated in this thesis, a multitude of up-scaled solar dishes as with individual reactor redox systems is economically less feasible and the preferred option would be to put an array of solar reactors onto a solar tower with a heliostat field to provide the concentrated solar energy input.

To appreciate the scaling needed, a commercial-scale solar fuel plant could use for example 10 heliostat fields, each collecting 100 MW_{thermal} of solar radiative power, to produce 95,000 liters kerosene a day (assuming an overall system efficiency η_{system} of 10%), enough to fuel an Airbus A350 carrying 325 passengers for a London-New York roundtrip flight. This requires an additional 20x scale up from the reactor described in [20] for a 1-MW_{thermal} solar reactor module, whose front quartz window is the limiting element. The commercial-size solar tower foresees an array of solar reactor modules, each attached to hexagon-shaped secondary concentrators in a honeycomb

arrangement [40]. Further assembling the array of solar reactor modules in at least two clusters and focusing the heliostat field alternately onto each cluster would enable the continuous operation of both redox steps of the cycle. This re-focusing of the heliostat field should be feasible with current hardware/software control but its dynamics still need to be proven in the field. The complexity of the entire fuel system would be comparable to that of a concentrated solar power (CSP) plant, for which incremental scaling has taken place. The required frontal area of the DAC subsystem, based on a modular design using the technology applied in the present solar fuel system, would be about 4500 m² for capturing approximately 100,000 tons CO₂/year needed for the process, and the land area covered would represent less than 1% of the total land footprint of the plant. Thus, the DAC modules can be arranged in a single row to avoid drawing CO₂-depleted air. Assuming $\eta_{\text{system}} = 10\%$, such a solar fuel plant would produce about 34 million liters kerosene/year. To put this in context, 2019 global aviation kerosene consumption was 414 billion liters; the total land footprint of all solar plants required to fully satisfy global demand would be about 45,000 km², equivalent to 0.5% of the area of the Sahara Desert.

6.2.6 Techno Economic Analysis

Techno economic analyses are an important tool to determine whether industrial implementation is economically feasible. Although there has already been substantial work done in analysing the potential of the presented technology, there is still room for further investigations, especially as the technology continues to become more and more mature. The following section is extracted from Ref. [97] and summarises the techno economic analyses conducted for an industrial implementation of the discussed fuel system.

Techno-economic analyses of the complete process chain analogous to the pathway demonstrated in this thesis estimated a jet fuel cost in the range 1.2 - 2 € / liter [90, 98, 99]. These cost values are predominantly sensitive

to the energy efficiencies (assumed $\eta_{\text{system}} = 4.4 - 11.7\%$), the CO_2 costs (assumed 100 €/ton CO_2 , consistent with the long-term cost target [100]), and the manufacturing costs of the heliostat field, which typically represent half of the total investments costs of the solar fuel system (assumed 100 €/m²; currently in the 100-150 €/m² range; DOE Sunshot's target is 75 USD/m²). This also explains the strong dependency of the fuel cost on the solar reactor performance because the higher $\eta_{\text{solar-to-syngas}}$ the smaller becomes the heliostat field for a given Q_{solar} , and consequently the lower the investments costs of the solar concentrating infrastructure. The auxiliary components at the interface between the three main processing subsystems, such as gas pipelines, compressors, storage tanks, and other balance-of-plant components, are embedded within the given range of cost values of the fuel. The compression and storage of CO_2 and syngas in the buffer tanks represent 9.5% of the investment costs [99], but can have a significant effect on η_{system} and ultimately on the annual O&M costs because of their electricity consumption; optimized integration to minimize storage size and learning-by-doing are warranted as the system undergoes upscaling. In particular, substantial R&D and implementation of heat recovery in the solar reactor [96, 56, 88] are needed to achieve the 20% value of $\eta_{\text{solar-to-syngas}}$ assumed in the economic analyses. As expected, solar thermochemical fuels are most competitively produced in desert regions with high DNI ($> 2500 \text{ kWh/m}^2$ per year) [98, 99]. In contrast to biofuels, which are limited by resource provision, global jet fuel demand can be met by utilizing less than 1% of the worldwide arid land [98], which does not compete with food or fodder production. Furthermore, the solar fuel production chain's life cycle assessment indicates 80% avoidance of greenhouse gas emission with respect to conventional fossil jet fuel, with emissions in the range 0.1-0.6 kg CO_2 -equivalent per liter jet fuel and approaching zero when construction materials (e.g. steel, glass) are manufactured using renewable energy [99], as the amount of CO_2 emitted during jet fuel combustion equals that captured from the air during its production.

The most recent study offering a technical, economic and environmental

analysis of the fuel production, estimate the jet fuel production cost for a plant in Chile at 2.3 €/L in the near-term and 0.6-1.3 €/L in the long-term future, with a 22-30% higher price for a plant located in Spain or Morocco [101].

6.2.7 Bringing Solar Fuels to the Market

A big challenge in bringing solar fuels to market, other than the necessary substantial advances in the technology, process optimization and upscaling, is creating the market for solar fuels and make it economically feasible. This should be supported by policy schemes that enable market introduction at commercial scale. The following section is summarised from Ref. [97] and is based on work performed by Johan Lilliestam and Anthony Patt, both co-authors and collaborators in the paper "Schäppi, R. *et. al.*, Drop-in fuels from sunlight and air. *Nature* 601, 63-68 (2022)" [97].

Industrial scale solar fuel plants need to overcome the issue that they require very high initial investment costs [99]. To bring down those costs through scaling effects and process optimisation as well as mass production of key components and learning by doing, they would first need to be widely deployed, and this is where they require policy support to create a market. Both CORSIA (Carbon Offsetting and Reduction Scheme for International Aviation) and the EU Emission Trading System aim to reduce CO₂ emissions with carbon-pricing. However, the current carbon price is too low to support market demand for solar fuels. A valuable option would be an aviation sector support scheme to create a near-term market for the first generation of industrial scale commercial solar fuel plants. The idea would be to introduce a jet fuel quota scheme where airlines and users or retailer of aviation fuels in general would have to proof, that a given quota of their fuel stems from solar fuel sources. This quota would initially be very small and could then be continuously increased to keep providing the marked demand to deploy new solar fuel plants. If the initial quota is chosen small enough compared to the overall jet fuel demand, the cost of this new policy would

be low enough to be widely politically accepted and the financial impact for example on a plane tickets would be nearly negligible, while it would still create the market for solar fuels — even if the price for this solar fuel would initially be at a multitude of the current fossil fuel price. The deployment of the first generation plants would then start the technologies path down the learning curve. Important to keep in mind for this scenario, is that the solar fuel produced is a drop-in fuel and hence does not require new infrastructure, but can use the existing network for storage, transportation and utilisation. Hence, with appropriate policy support solar fuels on long-term have the potential for decarbonising the aviation sector, underlining the importance of the demonstrated milestone of carbon-neutral solar fuel production from sunlight and air.

List of Figures

- 2.1 Simplified process chain of the solar fuel system integrating three thermochemical conversion units in series: 1) the direct air capture (DAC) unit which co-extracts CO_2 and H_2O directly from ambient air; 2) the solar redox unit which converts CO_2 and H_2O into a desired mixture of CO and H_2 (syngas) using concentrated solar energy; and 3) the gas-to-liquid (GTL) synthesis unit which finally converts syngas to methanol or liquid hydrocarbons. Two identical solar reactors are positioned at the focus of the solar concentrator for performing both redox steps of the thermochemical cycle simultaneously by alternating the concentrated solar input between them. While one solar reactor is performing the endothermic reduction step on sun, the second solar reactor is performing the exothermic oxidation step off sun. Red arrow indicates reduction (Eq. 1.1); blue arrow indicates oxidation (Eq. 1.2 and 1.3). Dimensions are not to scale. Upper-left insert: Cross-section of the solar reactor featuring a cavity-receiver containing a reticulated porous ceramic structure (RPC) made of pure ceria for performing the thermochemical redox cycle. 11

- 2.2 Schematics and photographs of the optical solar dish system:
 a) 3D rendering of the primary two-axis sun-tracking parabolic dish and secondary rotating flat reflector; b) Installed instruments: solar reactors, water-calorimeter, and Lambertian target. The dashed circle indicates the 0.4 m diameter focal point trajectory during rotation of the secondary reflector. Figure reproduced from Ref. [79]. 13
- 2.3 3D rendering of the solar reactor (left) and view of the open reactor cavity with the aluminium front and first insulation layer removed (right). Labeled are the radiation shield, water cooled front, thermocouple positions, thermal insulation, gas outlet, ceria RPC, ceria laminate, steel vessel, gas inlet, aperture + quartz window. 17
- 2.4 SEM images of RPC struts — Strut cross section 250x magnification (a, d) and 1000x magnification (b, e) and strut surface 1000x magnification (c, f) for unused RPC (a, b, c) and used RPC (d, e, f) after 293 on-sun redox cycles. 21
- 2.5 Photo of installed compression station with labeled components. 24
- 2.6 Representative CO₂-splitting Cycle. Measured RPC temperature (green), reactor pressure (red) and gas evolution rates (O₂ black and CO blue) over time for a CO₂-splitting cycle. Reduction up to $T_{\text{reduction-end}} = 1400^{\circ}\text{C}$ with $\dot{m}_{\text{Ar}} = 1 \text{ L/min}$ and $p_{\text{reactor}} = 4\text{mbar}$. Oxidation started at $T_{\text{oxidation-start}} = 1000^{\circ}\text{C}$ with $\dot{m}_{\text{CO}_2} = 7 \text{ L/min}$ and ambient pressure. 26

- 2.7 Full-day CO₂-splitting Cycles. Measured RPC temperatures (red and blue), DNI (yellow), and specific gas yield per cycle of CO (circle) and O₂ (asterisks) over 32 consecutive CO₂-splitting cycles of both solar reactors operated in alternate mode: while reactor A is performing the solar reduction step (eq. 1.1), reactor B is performing the oxidation step (eq. 1.2) and vice versa. Blue and red shaded areas indicate which reactor is on-sun performing the reduction step. Non-shaded areas indicate times where no reactor is performing the on-sun reduction, i.e. one reactor already finished the reduction step, while the other reactor is still performing the oxidation step. Reduction up to $T_{\text{reduction-end}} = 1400^{\circ}\text{C}$ with $\dot{m}_{\text{Ar}} = 1 \text{ L/min}$ and $p_{\text{reactor}} = 4\text{mbar}$. Oxidation started at $T_{\text{oxidation-start}} = 1000^{\circ}\text{C}$ with $\dot{m}_{\text{CO}_2} = 7 \text{ L/min}$ and at ambient pressure. . . . 27
- 2.8 Representative solar redox cycle producing syngas with composition suitable for methanol synthesis. a) Temporal variation of the nominal cavity temperature, total pressure, and outlet gas flow rates during a single redox cycle. b) Temporal variation of the cumulative species concentration and yield of solar syngas collected during the oxidation step. Operation conditions — During the reduction step: $Q_{\text{solar}} = 5.1 \text{ kW}$, $\dot{m}_{\text{Ar}} = 0.5 \text{ L/min}$, $T_{\text{reduction-end}} = 1450^{\circ}\text{C}$, $p_{\text{reactor}} \leq 25 \text{ mbar}$. During the oxidation step: $Q_{\text{solar}} = 0 \text{ kW}$, $\dot{m}_{\text{CO}_2} = 0.4 \text{ L/min}$, $\dot{m}_{\text{H}_2\text{O}} = 9.8 \text{ g/min}$, $T_{\text{oxidation-start}} = 900^{\circ}\text{C}$, $p_{\text{reactor}} = 1 \text{ bar}$ 32

- 2.9 Representative solar redox cycle producing syngas with composition suitable for FT synthesis. a) Temporal variation of the nominal cavity temperature, total pressure, and outlet gas flow rates during a single redox cycle. b) Temporal variation of the cumulative species concentration and yield of solar syngas collected during the oxidation step. Operation conditions — During the reduction step: $Q_{\text{solar}} = 4.1 \text{ kW}$, $\dot{m}_{\text{Ar}} = 0.5 \text{ L/min}$, $T_{\text{reduction-end}} = 1450^\circ\text{C}$, $p_{\text{reactor}} \leq 50 \text{ mbar}$. During the oxidation step: $Q_{\text{solar}} = 0 \text{ kW}$, $\dot{m}_{\text{CO}_2} = 0.2 \text{ L/min}$, $\dot{m}_{\text{H}_2\text{O}} = 9.8 \text{ g/min}$, $T_{\text{oxidation-start}} = 800^\circ\text{C}$, $p_{\text{reactor}} = 1 \text{ bar}$ 36
- 2.10 Representative day run of the solar redox unit for co-splitting H_2O and CO_2 . Temporal variations of the DNI (yellow), temperature (blue and red solid lines), pressure (blue and red dashed lines), syngas composition (diamond shapes for H_2 , circles for CO_2 and asterisks for CO), and cumulative syngas yield (black) of the two adjacent solar reactors A and B (blue and red) performing the thermochemical redox cycle simultaneously. The concentrated solar radiative input is alternated between the solar reactors A and B: while one reactor is solar irradiated to effect the reduction step (Eq. 1.1), H_2O and CO_2 are injected in the second reactor to effect the oxidation step (Eqs.1.2 and 1.3). Reduction: $\dot{m}_{\text{Ar}} = 0.5 \text{ L/min}$. Oxidation: $\dot{m}_{\text{CO}_2} = 0.3 \text{ L/min}$, $\dot{m}_{\text{H}_2\text{O}} = 9.8 \text{ g/min}$ 38
- 2.11 Syngas yield (H_2 in orange, CO in green, CO_2 in black) for each of the 152 consecutive solar redox cycles for producing syngas suitable for methanol synthesis. 40
- 2.12 Cyclic variation (blue data points) and cumulative $\text{H}_2:\text{CO}_x$ molar ratio (black curve) for the 152 consecutive redox cycles of Fig. 2.11 40

- 3.1 Parametric study of reduction parameters: Colours indicate the values obtained by integrating until $T_{\text{reduction-end}} = 1300, 1350, 1400, 1450, \text{ and } 1500^\circ\text{C}$, while trend lines for each $T_{\text{reduction-end}}$ obtained by data averaged over all solar radiative power levels; shapes indicate the average $P_{\text{solar}} = 4.4, 4.7, 5.0, 5.3, \text{ and } 5.6 \pm 0.15 \text{ kW}$; black brackets indicate different $\dot{m}_{\text{Ar}} = 1, 2, 3, 4, 5, 6, 7, \text{ and } 8 \text{ L/min}$. Oxidation: $\dot{m}_{\text{CO}_2} = 7 \text{ L/min}$, $T_{\text{oxidation-start}} = 900^\circ\text{C}$ 52
- 3.2 Parametric study of oxidation parameters. V_{syngas} , X_{CO_2} , $\Delta t_{\text{oxidation}}$ and $\eta_{\text{solar-to-syngas}}$ over varying $T_{\text{oxidation-start}}$ a), oxidation flows \dot{m}_{CO_2} b) and $\dot{m}_{\text{H}_2\text{O}}$ c). a) Varying $T_{\text{oxidation-start}}$, $\dot{m}_{\text{CO}_2} = 0.6 \text{ L/min}$, $\dot{m}_{\text{H}_2\text{O}} = 10 \text{ g/min}$. b) $T_{\text{oxidation-start}} = 900^\circ\text{C}$, varying \dot{m}_{CO_2} , $\dot{m}_{\text{H}_2\text{O}} = 10 \text{ g/min}$. c) $T_{\text{oxidation-start}} = 900^\circ\text{C}$, $\dot{m}_{\text{CO}_2} = 0.4 \text{ L/min}$, varying $\dot{m}_{\text{H}_2\text{O}}$. The colours mark different $R_{\text{H}_2:\text{CO}}$: $R_{\text{H}_2:\text{CO}} = 2.2$ (yellow), $R_{\text{H}_2:\text{CO}} = 2$ (red), $R_{\text{H}_2:\text{CO}} = 1.8$ (blue). Reduction: $T_{\text{reduction-end}} = 1500^\circ\text{C}$, $p_{\text{reactor}} = 50\text{-}200 \text{ mbar}$, $\dot{m}_{\text{Ar}} = 3 \text{ L/min}$ 54
- 3.3 CO_2 splitting — X_{CO_2} , \dot{m}_{CO} and V_{CO} as a function of temperature T during oxidation for different $T_{\text{oxidation-start}} = 600, 650, 700, 750, 800^\circ\text{C}$ and $\dot{m}_{\text{CO}_2} = 1, 2, \text{ and } 3 \text{ L/min}$ (indicated by different colours). Reductio conditions: $T_{\text{reduction-end}} = 1500^\circ\text{C}$, $\dot{m}_{\text{Ar}} = 3 \text{ L/min}$. Oxidation conditions: gas collection was terminated once CO concentration in the outlet gas dropped below 10%. 59

- 3.4 Co-splitting with high $\text{H}_2\text{O}:\text{CO}_2$ feed ratio — Cumulative conversions $X_{\text{H}_2\text{O}}$ and X_{CO_2} , instantaneous mass flows \dot{m}_{H_2} and \dot{m}_{CO} and cumulative yields V_{H_2} and V_{CO} as a function of temperature T during oxidation for $T_{\text{oxidation-start}} = 600, 700, 800, \text{ and } 900$ °C and $\dot{m}_{\text{H}_2} = 7, 8, 9, \text{ and } 10$ g/min (indicated by different colours). Reduction: $T_{\text{reduction-end}} = 1500$ °C, $\dot{m}_{\text{Ar}} = 3$ L/min. Oxidation: $\dot{m}_{\text{CO}_2} = 0.1$ L/min. Flush gas flow of 10 L/min CO_2 introduced once the measured total gas flow exiting the system dropped below 0.2 L/min averaged over a 5 s time period. Syngas collection was terminated once H_2 concentration dropped below 10%. 60
- 4.1 Automation flow diagram: 1) process flow chart (top) indicating set operational parameters (dark red) and measured data (light red); 2) control program logic (purple box) with arrows representing forwarded parameter values; 3) cycling control logic (blue box) an; 4) reactor sub-logic (orange box). 65
- 4.2 Optimisation run with 8 consecutive cycles showing oxidation parameters $T_{\text{oxidation-start}}$, \dot{m}_{CO_2} and $\dot{m}_{\text{H}_2\text{O}}$, measured $P_{\text{solar,mean}}$ and measured/calculated performance parameters V_{syngas} , \dot{V}_{syngas} , X_{CO_2} and $\eta_{\text{solar-to-syngas}}$ as a function of the cycle number. Filled: $R_{\text{H}_2:\text{CO}} = 2$ reached (cycle 1,2,3,6). Empty: $R_{\text{H}_2:\text{CO}} = 2$ not reached (cycle 4,5,7,8). Reduction: $T_{\text{reduction-end}} = 1500$ °C, $\dot{m}_{\text{Ar}} = 3$ L/min. Previous knowledge: Cycle with $T_{\text{oxidation-start}} = 750$ °C, $\dot{m}_{\text{CO}_2} = 0.7$ L/min and $\dot{m}_{\text{H}_2\text{O}} = 8$ g/min does not reach $R_{\text{H}_2:\text{CO}} = 2$. Set $PI_{i,\text{ref}}$ and w_i for CPI calculations: $w_{V_{\text{syngas}}} = 10$, $w_{\dot{V}_{\text{syngas}}} = 30$, $w_{X_{\text{CO}_2}} = 30$, $w_{\eta_{\text{solar-to-syngas}}} = 30$, $V_{\text{syngas,ref}} = 5$ L, $\dot{V}_{\text{syngas,ref}} = 7.5$ L/h, $X_{\text{CO}_2,\text{ref}} = 0.5$, $\eta_{\text{solar-to-syngas,ref}} = 0.02$. Parameter step sizes: 25° C for $T_{\text{oxidation-start}}$, 0.1 L/min for \dot{m}_{CO_2} , 1 g/min for $\dot{m}_{\text{H}_2\text{O}}$ 72

-
- 5.1 Causality diagram of the implemented grey box model containing the gaseous domains G, porous domains P and solid domains I (insulation), S (steel shell), F (water cooled front) and W (window). The arrows between the domains indicate exchanged energy and mass flows. Top left insert: Cross section of modelled reactor with coloured areas corresponding to the domains of the causality diagram. 79
- 5.2 Left: Cross section of modelled reactor domains for the simplified model with coloured areas corresponding to the domains of the causality diagram. Right: Causality diagram of the simplified grey box model containing the four porous domains P (shades of red) and one insulation solid domain I (purple). The arrows between the domains indicate exchanged energy and mass flows. 85
- 5.3 Temporal variation of temperatures of model domains P1, P2, P3, P4, I2 and measured RPC temperature for 1 cycle. For increased visibility only every 50th measured data point is plotted. Model based on parameter set 3. 91
- 5.4 Temporal variation of temperatures of the RPC domain P4 for a two reactor system making continuous use of the incoming solar power. Model based on parameter set 3. $P_{\text{solar}} = 4.8$ kW. Blue and red represent the two modelled reactors. . . . 95
- 5.5 Temporal variation of temperatures of the RPC domain P4 for a three reactor system making continuous use of the incoming solar power. Model based on parameter set 3. $P_{\text{solar}} = 4.8$ kW. Blue, red and yellow represent the three modelled reactors. 97
- 5.6 Temporal variation of temperatures of the RPC domain P4 for a two reactor system making continuous use of the incoming solar power. Model based on parameter set 3. $P_{\text{solar}} = 6.2$ kW. Blue and red represent the two modelled reactors. . . . 99

List of Tables

| | | |
|-----|--|----|
| 2.1 | Ingredients for ceria slurry for RPC production with quantities reported for a reference batch containing 1000 g ceria powder. Quantities of deionised H ₂ O reported for high/medium/low viscosity slurry. Ingredients PVA-40 and Contraspum KWE only added after 24 hours of milling. Zirconia milling balls removed after milling. | 21 |
| 5.1 | Parameter set 1. Results after parameter estimation of the UA products for the heat exchange between the domains. . . | 87 |
| 5.2 | Parameter set 2. Results after parameter estimation of the UA products for the heat exchange between the domains. . . | 87 |
| 5.3 | Parameter set 3. Results after parameter estimation of the UA products for the heat exchange between the domains. . . | 88 |
| 5.4 | Parameter set 4. Results after parameter estimation of the UA products for the heat exchange between the domains. . . | 88 |
| 5.5 | Parameter set 5. Results after parameter estimation of the UA products for the heat exchange between the domains. . . | 89 |
| 5.6 | Parameter set 6. Results after parameter estimation of the UA products for the heat exchange between the domains. . . | 89 |

Bibliography

- [1] V. Grewe, A. Gangoli Rao, T. Grönstedt, C. Xisto, F. Linke, J. Melkert, J. Middel, B. Ohlenforst, S. Blakey, S. Christie, S. Matthes, and K. Dahlmann, “Evaluating the climate impact of aviation emission scenarios towards the Paris agreement including COVID-19 effects,” *Nat. Commun.* 2021 121, vol. 12, pp. 1–10, jun 2021.
- [2] J. Chen, Y. Fei, and Z. Wan, “The relationship between the development of global maritime fleets and GHG emission from shipping,” *J. Environ. Manage.*, vol. 242, pp. 31–39, jul 2019.
- [3] A. W. Schäfer, S. R. Barrett, K. Doyme, L. M. Dray, A. R. Gnadt, R. Self, A. O’Sullivan, A. P. Synodinos, and A. J. Torija, “Technological, economic and environmental prospects of all-electric aircraft,” *Nat. Energy* 2018 42, vol. 4, pp. 160–166, dec 2018.
- [4] E. Cabrera and J. M. Melo de Sousa, “Use of Sustainable Fuels in Aviation—A Review,” *Energies*, vol. 15, apr 2022.
- [5] N. S. Lewis and D. G. Nocera, “Powering the planet: chemical challenges in solar energy utilization,” *Proc. Natl. Acad. Sci. U. S. A.*, vol. 103, pp. 15729–15735, oct 2006.
- [6] G. A. Ozin, “Throwing New Light on the Reduction of CO₂,” *Adv. Mater.*, vol. 27, pp. 1957–1963, mar 2015.

- [7] R. J. Detz, J. N. Reek, and B. C. Van Der Zwaan, “The future of solar fuels: when could they become competitive?,” *Energy Environ. Sci.*, vol. 11, pp. 1653–1669, jul 2018.
- [8] M. Romero and A. Steinfeld, “Concentrating solar thermal power and thermochemical fuels,” *Energy Environ. Sci.*, vol. 5, p. 9234, oct 2012.
- [9] S. Haussener, “Solar fuel processing: Comparative mini-review on research, technology development, and scaling,” *Sol. Energy*, vol. 246, pp. 294–300, nov 2022.
- [10] K. J. Warren and A. W. Weimer, “Solar thermochemical fuels: Present status and future prospects,” *Sol. Compass*, vol. 1, p. 100010, may 2022.
- [11] F. S. Zeman and D. W. Keith, “Carbon neutral hydrocarbons,” *Philos. Trans. R. Soc. A Math. Phys. Eng. Sci.*, vol. 366, pp. 3901–3918, nov 2008.
- [12] J. A. Wurzbacher, C. Gebald, N. Piatkowski, and A. Steinfeld, “Concurrent separation of CO₂ and H₂O from air by a temperature-vacuum swing adsorption/desorption cycle,” *Environ. Sci. Technol.*, vol. 46, no. 16, pp. 9191–9198, 2012.
- [13] E. Corporan, M. J. DeWitt, V. Belovich, R. Pawlik, A. C. Lynch, J. R. Gord, and T. R. Meyer, “Emissions characteristics of a turbine engine and research combustor burning a Fischer-Tropsch jet fuel,” *Energy and Fuels*, vol. 21, pp. 2615–2626, sep 2007.
- [14] C. Brady, M. E. Davis, and B. Xu, “Integration of thermochemical water splitting with CO₂ direct air capture,” *Proc. Natl. Acad. Sci. U. S. A.*, vol. 116, pp. 25001–25007, dec 2019.
- [15] J. Jia, L. C. Seitz, J. D. Benck, Y. Huo, Y. Chen, J. W. D. Ng, T. Bilir, J. S. Harris, and T. F. Jaramillo, “Solar water splitting by

- photovoltaic-electrolysis with a solar-to-hydrogen efficiency over 30%,” *Nat. Commun.*, 2016.
- [16] A. Chalmin, “Direct Air Capture: Recent developments and future plans” *Geoengineering Monitor*.
- [17] M. Roeb, J. P. Säck, P. Rietbrock, C. Prahll, H. Schreiber, M. Neises, L. de Oliveira, D. Graf, M. Ebert, W. Reinalter, M. Meyer-Grünefeldt, C. Sattler, A. Lopez, A. Vidal, A. Elsberg, P. Stobbe, D. Jones, A. Steele, S. Lorentzou, C. Pagkoura, A. Zygogianni, C. Agrafiotis, and A. G. Konstandopoulos, “Test operation of a 100 kW pilot plant for solar hydrogen production from water on a solar tower,” *Sol. Energy*, vol. 85, pp. 634–644, apr 2011.
- [18] F. V. Vázquez, J. Koponen, V. Ruuskanen, C. Bajamundi, A. Kosonen, P. Simell, J. Ahola, C. Frilund, J. Elfving, M. Reinikainen, N. Heikkinen, J. Kauppinen, and P. Piermartini, “Power-to-X technology using renewable electricity and carbon dioxide from ambient air: SOLETAIR proof-of-concept and improved process concept,” *J. CO₂ Util.*, 2018.
- [19] D. Marxer, P. Furler, J. Scheffe, H. Geerlings, C. Falter, V. Batteiger, A. Sizmann, and A. Steinfeld, “Demonstration of the entire production chain to renewable kerosene via solar thermochemical splitting of H₂O and CO₂,” *Energy and Fuels*, vol. 29, no. 5, pp. 3241–3250, 2015.
- [20] S. Zoller, E. Koepf, D. Nizamian, M. Stephan, A. Patané, P. Haueter, M. Romero, J. González-Aguilar, D. Lieftink, E. de Wit, S. Brendelberger, A. Sizmann, and A. Steinfeld, “A solar tower fuel plant for the thermochemical production of kerosene from H₂O and CO₂,” *Joule*, vol. 6, pp. 1606–1616, jul 2022.
- [21] J. R. Scheffe and A. Steinfeld, “Oxygen exchange materials for solar thermochemical splitting of H₂O and CO₂: a review,” *Mater. Today*, vol. 17, pp. 341–348, sep 2014.

- [22] S. Abanades, P. Charvin, G. Flamant, and P. Neveu, "Screening of water-splitting thermochemical cycles potentially attractive for hydrogen production by concentrated solar energy," *Energy*, vol. 31, pp. 2805–2822, nov 2006.
- [23] T. Kodama and N. Gokon, "Thermochemical cycles for high-temperature solar hydrogen production," *Chem. Rev.*, vol. 107, pp. 4048–4077, oct 2007.
- [24] A. Steinfeld, "Solar hydrogen production via a two-step water-splitting thermochemical cycle based on Zn/ZnO redox reactions," *Int. J. Hydrogen Energy*, vol. 27, pp. 611–619, jun 2002.
- [25] P. G. Loutzenhiser, A. Meier, and A. Steinfeld, "Review of the Two-Step H₂O/CO₂-Splitting solar thermochemical cycle based on Zn/ZnO redox reactions," *Materials (Basel)*, vol. 3, no. 11, pp. 4922–4938, 2010.
- [26] D. Weibel, Z. R. Jovanovic, E. Gálvez, and A. Steinfeld, "Mechanism of Zn particle oxidation by H₂O and CO₂ in the presence of ZnO," *Chem. Mater.*, vol. 26, pp. 6486–6495, nov 2014.
- [27] E. E. Koepf, S. G. Advani, A. K. Prasad, and A. Steinfeld, "Experimental investigation of the carbothermal reduction of ZnO using a beam-down, gravity-fed solar reactor," *Ind. Eng. Chem. Res.*, vol. 54, pp. 8319–8332, aug 2015.
- [28] M. Brkic, E. Koepf, and A. Meier, "Continuous Solar Carbothermal Reduction of Aerosolized ZnO Particles Under Vacuum in a Directly Irradiated Vertical-Tube Reactor," *J. Sol. Energy Eng. Trans. ASME*, vol. 138, apr 2016.
- [29] T. Nakamura, "Hydrogen production from water utilizing solar heat at high temperatures," *Sol. Energy*, vol. 19, pp. 467–475, jan 1977.

- [30] P. Charvin, S. Abanades, G. Flamant, and F. Lemort, "Two-step water splitting thermochemical cycle based on iron oxide redox pair for solar hydrogen production," *Energy*, vol. 32, pp. 1124–1133, jul 2007.
- [31] T. Kodama, Y. Nakamuro, and T. Mizuno, "A Two-Step Thermochemical Water Splitting by Iron-Oxide on Stabilized Zirconia," *J. Sol. Energy Eng.*, vol. 128, pp. 3–7, feb 2006.
- [32] N. Gokon, H. Murayama, J. Umeda, T. Hatamachi, and T. Kodama, "Monoclinic zirconia-supported Fe₃O₄ for the two-step water-splitting thermochemical cycle at high thermal reduction temperatures of 1400–1600°C," *Int. J. Hydrogen Energy*, vol. 34, pp. 1208–1217, feb 2009.
- [33] J. R. Scheffe, A. H. McDaniel, M. D. Allendorf, and A. W. Weimer, "Kinetics and mechanism of solar-thermochemical H₂ production by oxidation of a cobalt ferrite/zirconia composite," *Energy Environ. Sci.*, vol. 6, pp. 963–973, feb 2013.
- [34] T. Kodama, Y. Kondoh, R. Yamamoto, H. Andou, and N. Satou, "Thermochemical hydrogen production by a redox system of ZrO₂-supported Co(II)-ferrite," *Sol. Energy*, vol. 78, pp. 623–631, may 2005.
- [35] M. D. Allendorf, R. B. Diver, N. P. Siegel, and J. E. Miller, "Two-step water splitting using mixed-metal ferrites: Thermodynamic analysis and characterization of synthesized materials," *Energy and Fuels*, vol. 22, pp. 4115–4124, nov 2008.
- [36] W. C. Chueh and S. M. Haile, "Ceria as a thermochemical reaction medium for selectively generating syngas or methane from H₂O and CO₂," *ChemSusChem*, vol. 2, no. 8, pp. 735–739, 2009.
- [37] W. C. Chueh, C. Falter, M. Abbott, D. Scipio, P. Furler, S. M. Haile, and A. Steinfeld, "High-flux solar-driven thermochemical dissociation of CO₂ and H₂O using nonstoichiometric ceria," *Science (80-.)*, vol. 330, pp. 1797–1801, dec 2010.

- [38] W. C. Chueh and S. M. Haile, "A thermochemical study of ceria: exploiting an old material for new modes of energy conversion and CO₂ mitigation," *Philos. Trans. R. Soc. A Math. Phys. Eng. Sci.*, vol. 368, pp. 3269–3294, jul 2010.
- [39] P. Furler, J. Scheffe, M. Gorbar, L. Moes, U. Vogt, and A. Steinfeld, "Solar Thermochemical CO₂ Splitting Utilizing a Reticulated Porous Ceria Redox System," *Energy & Fuels*, vol. 26, pp. 7051–7059, nov 2012.
- [40] D. Marxer, P. Furler, M. Takacs, and A. Steinfeld, "Solar thermochemical splitting of CO₂ into separate streams of CO and O₂ with high selectivity, stability, conversion, and efficiency," *Energy Environ. Sci.*, vol. 10, pp. 1142–1149, may 2017.
- [41] M. Welte, R. Barhoumi, A. Zbinden, J. R. Scheffe, and A. Steinfeld, "Experimental Demonstration of the Thermochemical Reduction of Ceria in a Solar Aerosol Reactor," *Ind. Eng. Chem. Res.*, vol. 55, pp. 10618–10625, oct 2016.
- [42] J. R. Scheffe, R. Jacot, G. R. Patzke, and A. Steinfeld, "Synthesis, characterization, and thermochemical redox performance of Hf⁴⁺, Zr⁴⁺, and Sc³⁺ doped ceria for splitting CO₂," *J. Phys. Chem. C*, vol. 117, pp. 24104–24110, nov 2013.
- [43] M. Takacs, J. R. Scheffe, and A. Steinfeld, "Oxygen nonstoichiometry and thermodynamic characterization of Zr doped ceria in the 1573–1773 K temperature range," *Phys. Chem. Chem. Phys.*, vol. 17, pp. 7813–7822, mar 2015.
- [44] M. Hoes, C. L. Muhich, R. Jacot, G. R. Patzke, and A. Steinfeld, "Thermodynamics of paired charge-compensating doped ceria with superior redox performance for solar thermochemical splitting of H₂O and CO₂," *J. Mater. Chem. A*, vol. 5, pp. 19476–19484, sep 2017.

- [45] J. R. Scheffe, D. Weibel, and A. Steinfeld, "Lanthanum-strontium-manganese perovskites as redox materials for solar thermochemical splitting of H₂O and CO₂," *Energy and Fuels*, vol. 27, pp. 4250–4257, aug 2013.
- [46] T. Cooper, J. R. Scheffe, M. E. Galvez, R. Jacot, G. Patzke, and A. Steinfeld, "Lanthanum Manganite Perovskites with Ca/Sr A-site and Al B-site Doping as Effective Oxygen Exchange Materials for Solar Thermochemical Fuel Production," *Energy Technol.*, vol. 3, pp. 1130–1142, nov 2015.
- [47] M. Ezbiri, M. Takacs, B. Stolz, J. Lungthok, A. Steinfeld, and R. Michalsky, "Design principles of perovskites for solar-driven thermochemical splitting of CO₂," *J. Mater. Chem. A*, vol. 5, pp. 15105–15115, jul 2017.
- [48] C. K. Yang, Y. Yamazaki, A. Aydin, and S. M. Haile, "Thermodynamic and kinetic assessments of strontium-doped lanthanum manganite perovskites for two-step thermochemical water splitting," *J. Mater. Chem. A*, vol. 2, pp. 13612–13623, jul 2014.
- [49] A. H. McDaniel, E. C. Miller, D. Arifin, A. Ambrosini, E. N. Coker, R. O'Hayre, W. C. Chueh, and J. Tong, "Sr- and Mn-doped LaAlO₃δ for solar thermochemical H₂ and CO production," *Energy Environ. Sci.*, vol. 6, pp. 2424–2428, jul 2013.
- [50] S. Ackermann, J. R. Scheffe, and A. Steinfeld, "Diffusion of Oxygen in Ceria at Elevated Temperatures and Its Application to H₂ O/CO Splitting Thermochemical Redox Cycles," *J. Phys. Chem. C*, vol. 118, pp. 5216–5225, mar 2014.
- [51] S. Ackermann, L. Sauvin, R. Castiglioni, J. L. M. Rupp, J. R. Scheffe, and A. Steinfeld, "Kinetics of CO₂ Reduction over Nonstoichiometric Ceria," *J. Phys. Chem. C*, vol. 119, pp. 16452–16461, jul 2015.

- [52] N. Knoblauch, L. Dörrer, P. Fielitz, M. Schmücker, and G. Borchardt, “Surface controlled reduction kinetics of nominally undoped polycrystalline CeO₂,” *Phys. Chem. Chem. Phys.*, vol. 17, pp. 5849–5860, feb 2015.
- [53] O. T. Sørensen, “Thermodynamic studies of the phase relationships of nonstoichiometric cerium oxides at higher temperatures,” *J. Solid State Chem.*, vol. 18, pp. 217–233, jul 1976.
- [54] S. Abanades and G. Flamant, “Thermochemical hydrogen production from a two-step solar-driven water-splitting cycle based on cerium oxides,” *Sol. Energy*, vol. 80, pp. 1611–1623, dec 2006.
- [55] R. J. Panlener, R. N. Blumenthal, and J. E. Garnier, “A thermodynamic study of nonstoichiometric cerium dioxide,” *J. Phys. Chem. Solids*, vol. 36, pp. 1213–1222, nov 1975.
- [56] J. R. Scheffe and A. Steinfeld, “Thermodynamic analysis of cerium-based oxides for solar thermochemical fuel production,” *Energy and Fuels*, vol. 26, pp. 1928–1936, mar 2012.
- [57] M. Mogensen, N. M. Sammes, and G. A. Tompsett, “Physical, chemical and electrochemical properties of pure and doped ceria,” *Solid State Ionics*, vol. 129, pp. 63–94, apr 2000.
- [58] G. B. Haxel, J. B. Hedrick, and G. J. Orris, *Rare Earth Elements: Critical Resources for High Technology / USGS Fact Sheet 087-02*. fact sheet ed., 2002.
- [59] J. Madhusudhan Naik, C. Ritter, B. Bulfin, A. Steinfeld, R. Erni, G. R. Patzke, J. M. Naik, G. R. Patzke, C. Ritter, B. Bulfin, A. Steinfeld, and R. Erni, “Reversible Phase Transformations in Novel Ce-Substituted Perovskite Oxide Composites for Solar Thermochemical Redox Splitting of CO₂,” *Adv. Energy Mater.*, vol. 11, p. 2003532, apr 2021.

- [60] R. Jacot, J. M. Naik, R. Moré, R. Michalsky, A. Steinfeld, and G. R. Patzke, “Reactive stability of promising scalable doped ceria materials for thermochemical two-step CO₂ dissociation,” *J. Mater. Chem. A*, vol. 6, no. 14, pp. 5807–5816, 2018.
- [61] C. L. Muhich, B. W. Evanko, K. C. Weston, P. Lichty, X. Liang, J. Martinek, C. B. Musgrave, and A. W. Weimer, “Efficient generation of H₂ by splitting water with an isothermal redox cycle,” *Science (80-.)*, vol. 341, pp. 540–542, aug 2013.
- [62] A. Bayon, A. de la Calle, E. B. Stechel, and C. Muhich, “Operational Limits of Redox Metal Oxides Performing Thermochemical Water Splitting,” *Energy Technol.*, vol. 10, p. 2100222, jan 2022.
- [63] I. Ermanoski, J. E. Miller, and M. D. Allendorf, “Efficiency maximization in solar-thermochemical fuel production: challenging the concept of isothermal water splitting,” *Phys. Chem. Chem. Phys.*, vol. 16, pp. 8418–8427, apr 2014.
- [64] S. Abanades, A. Haeussler, and A. Julbe, “Synthesis and thermochemical redox cycling of porous ceria microspheres for renewable fuels production from solar-aided water-splitting and CO₂ utilization,” *Appl. Phys. Lett.*, vol. 119, jul 2021.
- [65] H. Kaneko, T. Miura, A. Fuse, H. Ishihara, S. Taku, H. Fukuzumi, Y. Naganuma, and Y. Tamaura, “Rotary-type solar reactor for solar hydrogen production with two-step water splitting process,” *Energy and Fuels*, vol. 21, pp. 2287–2293, jul 2007.
- [66] R. B. Diver, J. E. Miller, M. D. Allendorf, N. P. Siegel, and R. E. Hogan, “Solar thermochemical water-splitting ferrite-cycle heat engines,” *J. Sol. Energy Eng. Trans. ASME*, vol. 130, pp. 0410011–0410018, nov 2008.
- [67] J. Lapp, J. H. Davidson, and W. Lipiński, “Heat transfer analysis of a

- solid-solid heat recuperation system for solar-driven nonstoichiometric redox cycles,” *J. Sol. Energy Eng. Trans. ASME*, vol. 135, aug 2013.
- [68] S. Siegrist, H. Von Storch, M. Roeb, and C. Sattler, “Moving Brick Receiver-Reactor: A Solar Thermochemical Reactor and Process Design with a Solid-Solid Heat Exchanger and On-Demand Production of Hydrogen and/or Carbon Monoxide,” *J. Sol. Energy Eng. Trans. ASME*, vol. 141, apr 2019.
- [69] A. S. Patankar, X. Y. Wu, W. Choi, H. L. Tuller, and A. F. Ghoniem, “A Reactor Train System for Efficient Solar Thermochemical Fuel Production,” *J. Sol. Energy Eng. Trans. ASME*, vol. 144, dec 2022.
- [70] R. Bader, R. B. Chandran, L. J. Venstrom, S. J. Sedler, P. T. Krenzke, R. M. De Smith, A. Banerjee, T. R. Chase, J. H. Davidson, and W. Lipiński, “Design of a solar reactor to split CO₂ via isothermal redox cycling of ceria,” *J. Sol. Energy Eng. Trans. ASME*, vol. 137, jun 2015.
- [71] L. J. Venstrom, R. M. De Smith, Y. Hao, S. M. Haile, and J. H. Davidson, “Efficient splitting of CO₂ in an isothermal redox cycle based on ceria,” *Energy and Fuels*, vol. 28, pp. 2732–2742, apr 2014.
- [72] S. Brendelberger and C. Sattler, “Concept analysis of an indirect particle-based redox process for solar-driven H₂O/CO₂splitting,” *Sol. Energy*, vol. 113, pp. 158–170, 2015.
- [73] I. Ermanoski, N. P. Siegel, and E. B. Stechel, “A new reactor concept for efficient solar-thermochemical fuel production,” *J. Sol. Energy Eng. Trans. ASME*, vol. 135, aug 2013.
- [74] A. Singh, J. Lapp, J. Grobbel, S. Brendelberger, J. P. Reinhold, L. Olivera, I. Ermanoski, N. P. Siegel, A. McDaniel, M. Roeb, and C. Sattler, “Design of a pilot scale directly irradiated, high temperature, and low pressure moving particle cavity chamber for metal oxide reduction,” *Sol. Energy*, vol. 157, pp. 365–376, nov 2017.

- [75] A. Weber, J. Grobbel, M. Neises-von Puttkamer, and C. Sattler, “Swept open moving particle reactor including heat recovery for solar thermochemical fuel production,” *Sol. Energy*, vol. 266, p. 112178, dec 2023.
- [76] C. P. Falter and R. Pitz-Paal, “Modeling counter-flow particle heat exchangers for two-step solar thermochemical syngas production,” *Appl. Therm. Eng.*, vol. 132, pp. 613–623, mar 2018.
- [77] A. Haeussler, S. Abanades, A. Julbe, J. Jouannaux, and B. Cartoixa, “Solar thermochemical fuel production from H₂O and CO₂ splitting via two-step redox cycling of reticulated porous ceria structures integrated in a monolithic cavity-type reactor,” *Energy*, vol. 201, p. 117649, 2020.
- [78] P. Furler, J. R. Scheffe, and A. Steinfeld, “Syngas production by simultaneous splitting of H₂O and CO₂ via ceria redox reactions in a high-temperature solar reactor,” *Energy Environ. Sci.*, vol. 5, pp. 6098–6103, mar 2012.
- [79] F. Dähler, M. Wild, R. Schäppi, P. Haueter, T. Cooper, P. Good, C. Larrea, M. Schmitz, P. Furler, and A. Steinfeld, “Optical design and experimental characterization of a solar concentrating dish system for fuel production via thermochemical redox cycles,” *Sol. Energy*, vol. 170, no. March, pp. 568–575, 2018.
- [80] I. Reda and A. Andreas, “Solar position algorithm for solar radiation applications,” *Sol. Energy*, vol. 76, no. 5, pp. 577–589, 2004.
- [81] S. Zoller, E. Koepf, P. Roos, and A. Steinfeld, “Heat transfer model of a 50 kW solar receiver-reactor for thermochemical redox cycling using cerium dioxide,” *J. Sol. Energy Eng.*, vol. 141, p. in press, jan 2019.
- [82] U. Ash-Kurlander, O. Martin, L. D. Fontana, V. R. Patil, M. Bernegger, C. Mondelli, J. Pérez-Ramírez, and A. Steinfeld, “Impact of Daily Startup-Shutdown Conditions on the Production of Solar Methanol

- over a Commercial Cu-ZnO-Al₂O₃ Catalyst,” *Energy Technol.*, vol. 4, pp. 565–572, may 2016.
- [83] W. Villasmil, A. Meier, and A. Steinfeld, “Dynamic modeling of a solar reactor for zinc oxide thermal dissociation and experimental validation using IR thermography,” *J. Sol. Energy Eng. Trans. ASME*, vol. 136, feb 2014.
- [84] H. W. Häring and C. Ahner, “Industrial Gases Processing,” *Ind. Gases Process.*, pp. 1–296, jan 2008.
- [85] F. Dähler, M. Wild, R. Schächli, P. Haueter, T. Cooper, P. Furler, and A. Steinfeld, “A high-flux solar parabolic dish system for continuous thermochemical fuel production,” in *Opt. InfoBase Conf. Pap.*, vol. Part F69-O, 2017.
- [86] M. Hoes, S. Ackermann, D. Theiler, P. Furler, and A. Steinfeld, “Additive-Manufactured Ordered Porous Structures Made of Ceria for Concentrating Solar Applications,” *Energy Technol.*, vol. 1900484, pp. 1–8, 2019.
- [87] S. Sas Brunser, F. L. Bargardi, R. Libanori, N. Kaufmann, H. Braun, A. Steinfeld, and A. R. Studart, “Solar-Driven Redox Splitting of CO₂ Using 3D-Printed Hierarchically Channeled Ceria Structures,” *Adv. Mater. Interfaces*, p. 2300452, aug 2023.
- [88] J. Lapp, J. H. Davidson, and W. Lipiński, “Efficiency of two-step solar thermochemical non-stoichiometric redox cycles with heat recovery,” *Energy*, vol. 37, pp. 591–600, jan 2012.
- [89] W. Haije and H. Geerlings, “Efficient production of solar fuel using existing large scale production technologies,” *Environ. Sci. Technol.*, vol. 45, pp. 8609–8610, oct 2011.
- [90] J. Kim, T. A. Johnson, J. E. Miller, E. B. Stechel, and C. T. Maravelias, “Fuel production from CO₂ using solar-thermal energy: system level analysis,” *Energy Environ. Sci.*, vol. 5, pp. 8417–8429, aug 2012.

- [91] A. Lidor, Y. Aschwanden, J. Häseli, P. Reckinger, P. Haueter, and A. Steinfeld, “High-temperature heat recovery from a solar reactor for the thermochemical redox splitting of H₂O and CO₂,” *Appl. Energy*, vol. 329, jan 2023.
- [92] J. Petrasch, P. Osch, and A. Steinfeld, “Dynamics and control of solar thermochemical reactors,” *Chem. Eng. J.*, vol. 145, pp. 362–370, jan 2009.
- [93] J. Petrasch and A. Steinfeld, “Dynamics of a solar thermochemical reactor for steam-reforming of methane,” *Chem. Eng. Sci.*, vol. 62, pp. 4214–4228, aug 2007.
- [94] B. Bulfin, L. Hoffmann, L. De Oliveira, N. Knoblauch, F. Call, M. Roeb, C. Sattler, and M. Schmücker, “Statistical thermodynamics of non-stoichiometric ceria and ceria zirconia solid solutions,” *Phys. Chem. Chem. Phys.*, vol. 18, pp. 23147–23154, aug 2016.
- [95] P. Furler, J. Scheffe, D. Marxer, M. Gorbar, A. Bonk, U. Vogt, and A. Steinfeld, “Thermochemical CO₂ splitting via redox cycling of ceria reticulated foam structures with dual-scale porosities,” *Phys. Chem. Chem. Phys.*, vol. 16, pp. 10503–10511, may 2014.
- [96] L. Geissbühler, “Thermocline Thermal Energy Storage: Advances and Applications to CSP, Compressed Air Energy Storage, and Solar Fuels,” apr 2018.
- [97] R. Schächli, D. Rutz, F. Dähler, A. Muroyama, P. Haueter, J. Lilliestam, A. Patt, P. Furler, and A. Steinfeld, “Drop-in fuels from sunlight and air,” *Nature*, vol. 601, no. 7891, pp. 63–68, 2022.
- [98] C. Falter, N. Scharfenberg, and A. Habersetzer, “Geographical Potential of Solar Thermochemical Jet Fuel Production,” *Energies 2020, Vol. 13, Page 802*, vol. 13, p. 802, feb 2020.

-
- [99] C. Falter, A. Valente, A. Habersetzer, D. Iribarren, and J. Dufour, “An integrated techno-economic, environmental and social assessment of the solar thermochemical fuel pathway,” *Sustain. Energy Fuels*, 2020.
- [100] B. R. Sutherland, “Pricing CO2 Direct Air Capture,” *Joule*, vol. 3, pp. 1571–1573, jul 2019.
- [101] C. Moretti, V. Patil, C. Falter, L. Geissbühler, A. Patt, and A. Steinfeld, “Technical, economic and environmental analysis of solar thermochemical production of drop-in fuels,” *Sci. Total Environ.*, vol. 901, p. 166005, nov 2023.

Curriculum Vitae

| | |
|---------------|--|
| Name | Remo Schäppi |
| Nationality | Swiss |
| Citizen of | Horgen (ZH) |
| Date of birth | September 6, 1989 |
| 2018–2023 | Doctoral studies, Professorship of Renewable Energy Carriers, Department of Mechanical and Process Engineering, ETH Zurich. Supervisor: Prof. Dr. Aldo Steinfeld |
| 2017–2018 | Internship, Dyenamo AB and Swerea IVF, Gothenburg, Sweden |
| 2015–2018 | MSc in Mechanical Engineering, ETH Zurich |
| 2011–2015 | BSc in Mechanical Engineering, ETH Zurich |
| 2008 | Matura at Mathematisch-Naturwissenschaftliches Gymnasium Rämibühl, Zurich, Switzerland |

List of Publications

Journal articles

R. Schäppi, V. Hüsler and A. Steinfeld, “Solar Thermochemical Production of Syngas from H₂O and CO₂ — Experimental Parametric Study, Control, and Automation”, *Industrial & Engineering Chemistry Research*, *in press*, 2024.

R. Schäppi, D. Rutz, F. Dähler, A. Muroyama, P. Haueter, J. Lilliestam, A. Patt, P. Furler and A. Steinfeld, “Drop-in Fuels from Sunlight and Air”, *Nature* 601, 63-68, 2022.

F. Dähler, M. Wild, R. Schäppi, P. Haueter, T. Cooper, P. Good, C. Larrea, M. Schmitz, P. Furler and A. Steinfeld, “Optical Design and Characterization of a Solar Concentrating Dish System for Fuel Production via Thermochemical Redox Cycles”, *Solar Energy* 170, 568-575, 2018.

Conference Proceedings

R. Schäppi, D. Rutz, P. Basler, A. Muroyama, P. Haueter, P. Furler and A. Steinfeld, “Solar Thermochemical Splitting of CO₂ in a Modular Solar Dish-Reactor System”, *Proceedings of ISES Solar World Congress 2019*, 2019. doi:10.18086/swc.2019.24.08

F. Dähler, M. Wild, R. Schäppi, P. Haueter, T. Cooper, P. Furler and

A. Steinfeld, “A High-Flux Solar Parabolic Dish System for Continuous Thermochemical Fuel Production”, Proceedings of the OSA Light, Energy and Environment Congress, 2017.

Conference Presentations

R. Schäppi, A. Steinfeld, “Dynamic Model of a Solar Fuel System for the Thermochemical Production of Syngas from H₂O and CO₂”, AIChE Annual Meeting 2023, Orlando FL, USA, 2023.

R. Schäppi, A. Steinfeld, “Automation and Parametric Study of a Solar Fuel System for the Thermochemical Production of Syngas from H₂O and CO₂”, 17th International Conference on Energy Sustainability (ASME ES 2023), Washington D. C., USA, 2023.

R. Schäppi, V. Hüsler, A. Steinfeld, “Automation and Parametric Study of a Solar Fuel System for the Thermochemical Production of Syngas from H₂O and CO₂”, AIChE Annual Meeting 2022, Phoenix AZ, USA, 2022.

R. Schäppi, A. Steinfeld, “Fully-automated Solar Fuel System for the Thermochemical Production of Syngas from H₂O and CO₂ Applicable for Methanol or Fischer-Tropsch Synthesis”, 3rd SFERA-III / 16th SOLLAB Doctoral Colloquium & Summer School 2022, Zurich, Switzerland, 2022.

R. Schäppi, V. Hüsler, A. Steinfeld, “Fully-Automated and Feedback Loop-Controlled Solar Fuel System for the Thermochemical Production of Syngas From H₂O and CO₂ Applicable for Methanol or Fischer-Tropsch Synthesis”, 16th International Conference on Energy Sustainability (ASME ES 2022), Philadelphia PA, USA, 2022.

R. Schäppi, P. Haueter, P. Furler, A. Steinfeld, “Solar Syngas Production from H₂O and CO₂ Applicable for Methanol or Fischer-Tropsch Synthesis”, 2021 AIChE Annual Meeting, Boston MA, USA, 2021.

R. Schächli, P. Haueter, P. Furler, A. Steinfeld, “Solar Fuel Production from Ambient Air in a Modular Solar Concentrator-Reactor System”, 15th International Conference on Energy Sustainability (ASME ES 2021), Online, 2021.

R. Schächli, D. Rutz, F. Dähler, P. Haueter, P. Furler, A. Steinfeld, “Methanol from Sunlight and Air Using a Modular Solar Dish Reactor System”, 2020 AIChE Annual Meeting, Online, 2020.

R. Schächli, D. Rutz, P. Basler, A. Muroyama, P. Haueter, P. Furler, A. Steinfeld, “Methanol from Sunlight and Air Using a Modular Solar Dish Reactor System”, MaP Graduate Symposium 2020, Online, 2020.

R. Schächli, D. Rutz, P. Basler, A. Muroyama, P. Haueter, P. Furler and A. Steinfeld, “Solar Thermochemical Splitting of CO₂ in a Modular Solar Dish-Reactor System”, ISES Solar World Congress 2019, Santiago, Chile, 2019.

Invited Talks

R. Schächli, A. Steinfeld, “Development of an Automation Software for the Control and Operation of a Solar Refinery with Redox Reactors”, 4th SFERA-III Summer School 2023, Cologne, Germany, 2023.

R. Schächli, A. Steinfeld, “Fuel from Sunlight and Air — Demonstration of the Thermochemical Pathway”, 3rd International Forum on Hydrogen Production Technologies (HyPT-3), Online, 2023.

R. Schächli, A. Steinfeld, “Fuel from Sunlight and Air - Demonstration of the Thermochemical Pathway”, LTP/PSI Thursday Colloquia, Villigen, Switzerland, 2022.

R. Schächli, A. Steinfeld, “Fuel from Sunlight and Air — Demonstration of the Thermochemical Pathway”, COST Action 18234 Conference - Designing

The Future: Electro-, Photo- And Thermo-Chemical Water Splitting, Brussels, Belgium, 2022.

R. Schächli, A. Steinfeld, “Treibstoff aus Luft und Sonnenlicht”, 32. Energie-Lunch / Treibstoffe - quo vadis, Winterthur, Switzerland, 2021.

R. Schächli, A. Steinfeld, “Solar Fuel Production from Ambient Air in a Modular Solar Concentrator-Reactor System”, Transforming the Air, Sea, and Land Freight Transport Sector - SWC50 Webinar, Online, 2022.

R. Schächli, D. Rutz, F. Dähler, P. Haueter, P. Furler, A. Steinfeld, “Thermochemical Fuel Production from Sunlight and Air”, EIT Urban Mobility 2020, Online, 2020.

R. Schächli, F. Dähler, P. Haueter, P. Furler, A. Steinfeld, “CO₂-neutrale Treibstoffe aus Luft und Sonnenlicht”, Richard Vollenweider Lectures 2020/21, Luzern, Switzerland, 2020.

R. Schächli, F. Dähler, P. Haueter, P. Furler, A. Steinfeld, “Treibstoff aus Luft und Sonnenlicht”, Treffpunkt Science City. Herbst 2020: Es wird heiss! Die Klimakrise, Online, 2020.